



Maria Golovleva

NUMERICAL SIMULATIONS OF DEFECT MODELING IN SEMICONDUCTOR RADIATION DETECTORS

HIP-Internal Report Series HIP-2022-02



Maria Golovleva

NUMERICAL SIMULATIONS OF DEFECT MODELING IN SEMICONDUCTOR RADIATION DETECTORS

Dissertation for the degree of Doctor of Science (Technology) to be presented with due permission for public examination and criticism in the Auditorium 1316 at Lappeenranta-Lahti University of Technology LUT, Lappeenranta, Finland on the 18th of November, 2022, at noon.

HIP-Internal Report Series HIP-2022-02

Acta Universitatis
Lappeenrantaensis 1050

Supervisors Professor Panja-Riina Luukka
Department of Physics
Lappeenranta-Lahti University of Technology LUT
Helsinki Institute of Physics
Finland

Adj. Professor Jens Erik Brücken
Helsinki Institute of Physics
University of Helsinki
Finland

Reviewers Professor Flyura Djurabekova
Department of Physics
University of Helsinki
Finland

PhD Giulio Pellegrini
Spanish National Centre of Microelectronics
Autonomous University of Barcelona
Spain

Opponent Professor Flyura Djurabekova
Department of Physics
University of Helsinki
Finland

ISBN 978-952-335-876-8
ISBN 978-952-335-877-5 (PDF)
ISSN 1456-4491 (Print)
ISSN 2814-5518 (Online)

Lappeenranta-Lahti University of Technology LUT
LUT University Press 2022

Abstract

Maria Golovleva

Numerical simulations of defect modeling in semiconductor radiation detectors

Lappeenranta 2022

72 pages

Acta Universitatis Lappeenrantaensis 1050

HIP-Internal Report Series HIP-2022-02

Diss. Lappeenranta-Lahti University of Technology LUT

ISBN 978-952-335-876-8, ISBN 978-952-335-877-5 (PDF), ISSN 1456-4491 (Print),

ISSN 2814-5518 (Online)

Semiconductor radiation detectors are the core of high energy physics experiments. Silicon (Si)-based segmented particle sensors detect and track all the charged particles that are produced during the collisions in different experiments at LHC, for example. Silicon tracking detectors have been designed and developed to cope with the already challenging radiation environments of the present LHC. However, after the foreseen upgrade, the inner tracking systems will have to be operable at extreme radiation levels. Sensors suffer from radiation induced damage that deteriorate the device performance, such as reducing charge collection efficiency.

Another use of such detectors is medical imaging. However, in addition to the radiation-induced defects that deteriorate device efficiency during their working lifetime, there are process-related issues at the manufacturing stage that can drastically affect device efficiency. For instance, in case of Cadmium Telluride (CdTe) sensors, extended crystallographic defects can lead to locally reduced charge collection.

The costs and time of the development phase of a semiconductor device can be largely reduced through the application of Technology Computer-Aided Design (TCAD) software packages. TCAD is an important tool for understanding the link between semiconductor physics and the electrical behavior of devices. It is used to design, analyze and optimize semiconductor technologies and devices based on accurate models of fundamental processes. This thesis features the simulation studies of the defect impact on the device performance. In particular, *CdTe* diodes, chemical vapor deposited (CVD) diamond detectors and Si detectors with aluminium oxide (Al_2O_3) thin film have been simulated and studied. Comparisons between the simulated results have been done to the corresponding laboratory measurements performed under equivalent conditions. Surface damage simulation studies of Al_2O_3 thin films have been performed. The study of the effects of defects in CdTe pad detectors with the red laser transient current technique (TCT) and the effect of the surface passivation on the outcome signal was performed.

Keywords: TCAD, CdTe, CVD diamond, semiconductor, defect

Acknowledgements

I would like to express my gratitude to my supervisors prof. Tuure Tuuva and prof. Panja Luukka for their guidance and support throughout the research process. Erik Brücken is thanked for the help in the reviewing of the manuscript.

The pre-examiners of my thesis Dr. Giulio Pellegrini, and Prof. Flyura Djurabekova, are thanked for the detailed evaluation of the manuscript and for their constructive feedback. Prof. Flyura Djurabekova is much appreciated for acting as my opponent in the public defence.

I am very grateful to all my colleagues, members of the CMS Upgrade project at HIP.

Special thanks go to my parents and brother for their guidance and support. Without them it would not be possible to be where I am now.

And last but not least, I wish to thanks my beloved family for their support during my studies. I'm very grateful to my girls Ekaterina and Anna and I am sincerely and heartily grateful to my husband Ivan for his understanding, care, love and help in finding balance in this life.

Maria Golovleva
October 2022
Lappeenranta, Finland

To my family.

Contents

Abstract	3
Acknowledgments	5
Contents	9
List of publications	11
Nomenclature	13
1 Introduction	15
2 Semiconductor basic structures	19
2.1 The p-n junction	19
2.2 MOS capacitors	23
2.3 Metal semiconductor contact	27
3 Radiation interactions	29
3.1 Interactions of heavy charged particles with matter	29
3.2 Interactions of fast electrons with matter	31
3.3 Interactions of X-rays and gamma rays with matter	32
3.4 Interactions of neutrons with matter	34
4 Particle detectors	35
4.1 Silicon tracking sensors	35
4.2 CVD diamond radiation detectors	36
4.3 CdTe radiation detectors	37
5 Radiation damage in silicon detectors	39
5.1 Bulk damage	40
5.2 Surface damage	41
6 Simulation of defects	43
7 Results and discussions	47
7.1 Simulation study of MOS capacitor and silicon detectors with Al ₂ O ₃ and HfO ₂ thin films	47
7.2 Simulation study of CVD diamond sensors	53
7.3 Simulation study of CdTe detectors	55
8 Conclusion	63
References	65
Publications	

List of publications

This dissertation is based on the following papers. The rights have been granted by publishers to include the papers in dissertation.

- I. T.Naaranaja, M.Golovleva, L.Martikainen, M.Berretti, K.Österberg (2019). Space charge polarization in irradiated single crystal CVD diamond. *Diamond and Related Materials*, Volume 96, pp 167-175.
- II. A.Gädda, J.Ott, A.Karadzhinova-Ferrer, M.Golovleva, M.Kalliokoski, A.Winkler, P.Luukka, J.Härkönen (2019). Cadmium Telluride X-ray pad detectors with different passivation dielectrics. *Nuclear Instruments and Methods in Physics Research Section A: Accelerators, Spectrometers, Detectors and Associated Equipment*, Volume 924, pp 33-37.
- III. M. Golovleva, M. Bezak, S. Bharthuar, E. Brücken, A. Gädda, J. Härkönen, M. Kalliokoski, S. Kirschenmann, P. Luukka, J. Ott, T. Tuuva (2021). Modeling the impact of defects on the charge collection efficiency of a Cadmium Telluride detector. *Journal of Instrumentation*, Volume 16, P08027.
- IV. S. Bharthuar, M. Golovleva, M. Bezak, E. Brücken, A. Gädda, J. Härkönen, A. Karadzhinova-Ferrer, N. Kramarenko, S. Kirschenmann, P. Luukka, K. Mizohata, J. Ott, and E. Tuominen (2022). Characterization of Heavily Irradiated Dielectrics for Pixel Sensors Coupling Insulator Applications. *Frontiers in Materials*, Volume 8, 769947.

Author's contribution

In paper I T. Naaranaja is the main author. Golovleva analyzed the experimental data and planned TCAD simulations. She conducted the simulations and wrote the simulation part of the publication. Golovleva participated in discussion of experimental results and in writing of the article.

In paper II A. Gädda is the primary author. Golovleva planned, executed, analyzed, and wrote the simulation part of the publication. Additionally, the author participated in the discussion of the results and in writing of the article.

In paper III Golovleva is the primary writer of the paper. Author analyzed experimental data and planned as well as conducted TCAD simulations.

In paper IV S. Bharthuar is the main author. Golovleva planned, executed, analyzed, and wrote the simulation part of the publication. Also author participated in the discussion of the results and the revision of the paper.

Nomenclature

Greek alphabet

χ	Semiconductor electron affinity
ϵ_s	permittivity of the semiconductor material
ϵ_{ox}	oxide permittivity
μ_e	electron mobility
μ_h	hole mobility
Φ_m	metal workfunction
ϕ_s	surface potential
Φ_{Si}	Silicon workfunction
ρ	charge density
τ_g	generation lifetime
v	Charge carrier velocity

Symbols

A	Area
C	Capacitance
C_{ox}	Oxide capacitance
d	Sensor bulk thickness
D_{it}	Interface trap density
d_{ox}	Oxide thickness
E	Electric field
E_c	Conduction band energy
E_g	Energy
E_v	Valence band energy
E_w	Weighting electric field
I_{bulk}	Bulk generation current
I_{ds}	Drain-to-source current
I_{leak}	Leakage current
N_a	Acceptor concentration
N_d	Donor concentration
N_{eff}	Effective doping concentration
n_i	Intrinsic concentration
Q	Charge
q	Elementary charge
Q_f	Fixed oxide charge
Q_{acc}	Accumulation charge
Q_{it}	Interface trapped charge
Q_{ox}	Effective oxide charge
T	Temperature

V_{bi}	Build-in potential
V_{fb}	Flat band voltage
V_{fd}	Full depletion voltage
V_g	Gate voltage
V_{th}	Threshold voltage
W	Total width of a space charge

Abbreviations

Al_2O_3	Aluminium oxide
HfO_2	Hafnia oxide
2D	two dimensional
3D	three dimensional
AC	Alternating current
ALD	Atomic layer deposition
AlN	Aluminium nitride
ATLAS	A Toroidal LHC Apparatus
CCE	Charge Collection Efficiency
CdTe	Cadmium Telluride
CERN	European Council for Nuclear Research
CMS	Compact Muon Solenoid
CV	Capacitance voltage
CVD	Chemical vapor deposition
DC	Direct current
FWHM	Full width half maximum
HL-LHC	High Luminosity Large Hadron Collider
IV	Current voltage
LHC	Large Hadron Collider
MOS	Metal oxide semiconductor
MOSFET	Metal Oxide Semiconductor field effect transistor
SCR	Space charge region
Si	Silicon
SRH	Shockley-Read-Hall statistics
TCAD	Technology Computer Aided Design
TCT	Transient current technique
TOTEM	Total Elastic and diffractive cross-section Measurement

1 Introduction

The Large Hadron Collider (LHC) is the largest particle accelerator currently existing. The collider itself is contained in a circular tunnel on the border between France and Switzerland, near the city of Geneva, with a circumference of 27 km. It has been built by the effort of thousands of scientists, engineers, and technicians, to find the missing parts of the 'puzzle' of the Standard model and many other questions about our Universe, such as supersymmetry, dark matter, extra dimensions [1]. After the first run, between 2010 and 2013, the last missing particle of the Standard Model, the Higgs boson, has been found [2, 3]. Proton beam energies of 4 TeV and thus center-of mass energies of 8 TeV were reached at that time. After an upgrade, the LHC was restarted in 2015. In this data taking period, called Run 2, the machine was reaching centre-of-mass energies of 13 TeV. In the following Long Shutdown 2 (LS2) that started during 2019, the emphasis was on upgrading the detectors. However, due to the COVID-19 pandemic many activities on the CERN site were slowed down, leading to delays in the scheduling. Preparations for Run 3 of the LHC finally begun in March 2022, during which the centre-of-mass proton beam energies will reach 13.6 TeV. The next large shutdown, Long Shutdown 3 (LS3), is dedicated to a major upgrade of the LHC itself. The plan is to increase the luminosity of the present LHC by a factor of 10, leading to the so-called High Luminosity LHC (HL-LHC). Currently it is expected that the HL-LHC will come into operation at the end of 2027. The machine upgrade will make it necessary to also upgrade all detector systems to cope with the strong increase of collisions and therefore higher radiation levels.

In order to detect and track all the particles that are produced during the collisions and to measure their properties, various types of detectors are used. Modern particle detectors consist of the layers of subdetectors, each designed to be in charge of the particular task, such as: tracking devices to trace the path of the particle, calorimeters to stop, absorb and measure a particle's energy, and particle-identification detectors to identify the particle. Semiconductor tracking detectors, designed to precisely track the paths of electrically charged particles as they pass through and interact with suitable substances, are the core of all large collider physics experiments [4–7]. The inner layers of the tracking detectors consists of strip and pixel detectors and are closest to the beam pipe and are therefore exposed to the highest levels of radiation. Silicon (Si) tracking detectors have been designed and developed to cope with the already challenging radiation environments of the present Large Hadron Collider. But after the foreseen upgrade, the inner tracking systems have to be able to withstand fluences of up to 2×10^{16} neq/cm² [8]. Sensors suffer from the radiation-induced damage in the silicon bulk that, on the device performance level, can be identified as increased leakage current (I_{leak}) and full depletion voltage (V_{fd}), as well as reduced charge collection efficiency (CCE) [9]. Besides the bulk damage, there is radiation-induced surface damage that is crucial for the isolation of the sensor segments and for the AC-coupled devices. In addition to the radiation-induced defects that deteriorate device efficiency during its working lifetime, there are process-related issues at the manufacturing stage that can drastically affect device efficiency [10].

Sensors, fabricated on a p-type substrate with segmented heavily doped n-type implants, have improved CCE due to a higher mobility of electrons in comparison with holes. In order to electrically isolate the segments, additional implants, known as p-stops and p-sprays, are utilized [11]. The traditional SiO_2 dielectric possesses positive oxide charge, that would lead to the formation of short circuiting channels between the n+ implants. The application of a dielectric with a negative oxide charge can eliminate the usage of p-stop and p-spray structures and therefore simplify the wafer processing. Atomic Layer Deposition (ALD) grown aluminium oxide Al_2O_3 thin films are a good candidate as they possess a high negative oxide charge [12, 13]. Thus, the surface damage studies of such negative charged thin films are necessary in order to evaluate their radiation tolerance.

There are other materials, cadmium telluride (CdTe) and chemical vapor deposited (CVD) diamond, that are of interest for the semiconductor industry. These materials have outstanding characteristics, such as large bandgap, high charge mobility, high resistivity, high breakdown voltage, and low dielectric constant, which result in low-noise fast-signal responses. And from the technological point of view, sensors based on these materials can have simple designs that do not need fabrication of p-n junctions. Despite the material advantages, there are some issues that need to be studied. For instance, in case of CdTe sensors, point and extended crystallographic defects can lead to locally reduced CCE [14, 15] and for the diamond detectors, signal degradation was observed in heavily irradiated material.

Future LHC upgrade will further increase luminosity, creating an even more destructive environment for silicon detectors. Therefore, the development of detectors comprising of alternative materials withstanding high energies is of great importance. The costs and duration of the development phase of a semiconductor device can be significantly reduced by the application of Technology Computer-Aided Design (TCAD) software packages. "TCAD represents our physical understanding of processes and devices in terms of computer models of semiconductor physics" [16]. TCAD is an important tool for understanding the link between semiconductor physics and the electrical behavior of devices. It is used to design, analyze and optimize semiconductor technologies and devices based on accurate models of fundamental processes. The capability of implementation of the experimentally observed effects in the simulation models will lead to an increase in the predictability of numerical simulations, which in turn results in reduced time and cost in detector design and testing.

The main objective of this thesis is to set the ability of the TCAD simulation to adapt to different tasks and problems. In particular, the modeling of the impact of various types of defects for different radiation sensors, such as CdTe diodes and CVD diamond detectors, have been performed. Simulation studies have been performed for surface radiation damage on the Si test structures with aluminium oxide (Al_2O_3) and hafnium oxide (HfO_2) thin films and compared to experimentally measured data in the laboratory after the irradiation.

The thesis is organized into seven sections. It starts with the introduction to the back-

ground and motivation of the research in Section 1. The basics of a silicon particle detector are explained in Section 2. In Section 3 the interaction of different types of ionizing radiation with the detector material is described. Then, radiation detection and challenges that arise for different particle detectors are described in Section 4. Section 5 reports on the radiation damage and its impact on silicon detectors. Section 6 presents an outline of the TCAD simulation tools. Next, the results of the several studies that are included in this thesis are presented. Finally, the conclusions and some suggestions for future work are given.

2 Semiconductor basic structures

A basic silicon particle detector is represented by a reversed biased p-n junction. Charged particles traversing the silicon body generate electron-hole pairs by ionization. These electron-hole pairs split in the applied electric field and electrons and holes start to move in opposite directions through the detector's bulk to anode and cathode electrodes, respectively, where they are collected. This section gives a short introduction to the principles of operation of a p-n junction and basic semiconductor structures. The theory presented in this section is based on Refs. [17].

2.1 The p-n junction

Silicon is a group IV element of the periodic table and an intrinsic semiconductor. The electronic band structure of semiconductors is represented by the energy gap between valence band and conduction band. Si has an indirect bandgap with an energy of $E_g = 1.12$ eV at room temperature. Silicon can be doped by replacing some of the silicon atoms by either donors (n-type silicon) or by acceptors (p-type silicon). A donor atom has five valence electrons, four of which will form a covalent bonding with a Si atom, while the fifth electron is free and is donated to the conduction band. In such cases the remaining donor atom becomes positively charged. An acceptor atom, on the other hand, has fewer electrons than required to form covalent bonding to all neighbors. In order to complete the missing bond, an electron is accepted from the valence band, leaving a hole there. An electron capture thus changes the acceptor atom state from neutral to negatively charged.

When n-type silicon and p-type silicon are joint together, the doping of the semiconductor changes rapidly from n-type to p-type, forming a space charge region (SCR) at the boundary, the so-called p-n junction. Free electrons of the n-type silicon and free holes of the p-type silicon diffuse and combine until equilibrium is reached. Only the ionized doping atoms remain as fixed charges. Consequently, there are no free charge carriers in this region, called the depletion region. The fixed doping ions form an electric field directed from positive charge to negative charge. The electric field strength has its maximum at the pn-junction and is zero at the edges of the depletion region. The potential difference of the Fermi levels in p- and n-type semiconductors that is dropped across the depletion region is called built-in potential, V_{bi} . In this case, when the doping concentration of one side of the abrupt junction is much higher than that of the other, the so called one-sided junction, the depletion region extends much further into the less doped side of the junction.

The electric properties of the junction can be calculated using the Poisson equation:

$$-\frac{d^2\Phi}{dx^2} = \frac{dE}{dx} = \frac{\rho(x)}{\epsilon_s}, \quad (2.1)$$

where Φ is a potential energy, E is the electric field, $\rho(x)$ is the net charge density and ϵ_s is the permittivity of the semiconductor material. Assuming an abrupt junction, as shown in Fig. 2.1, and an absence of free carriers in the depleted region, the net charge density

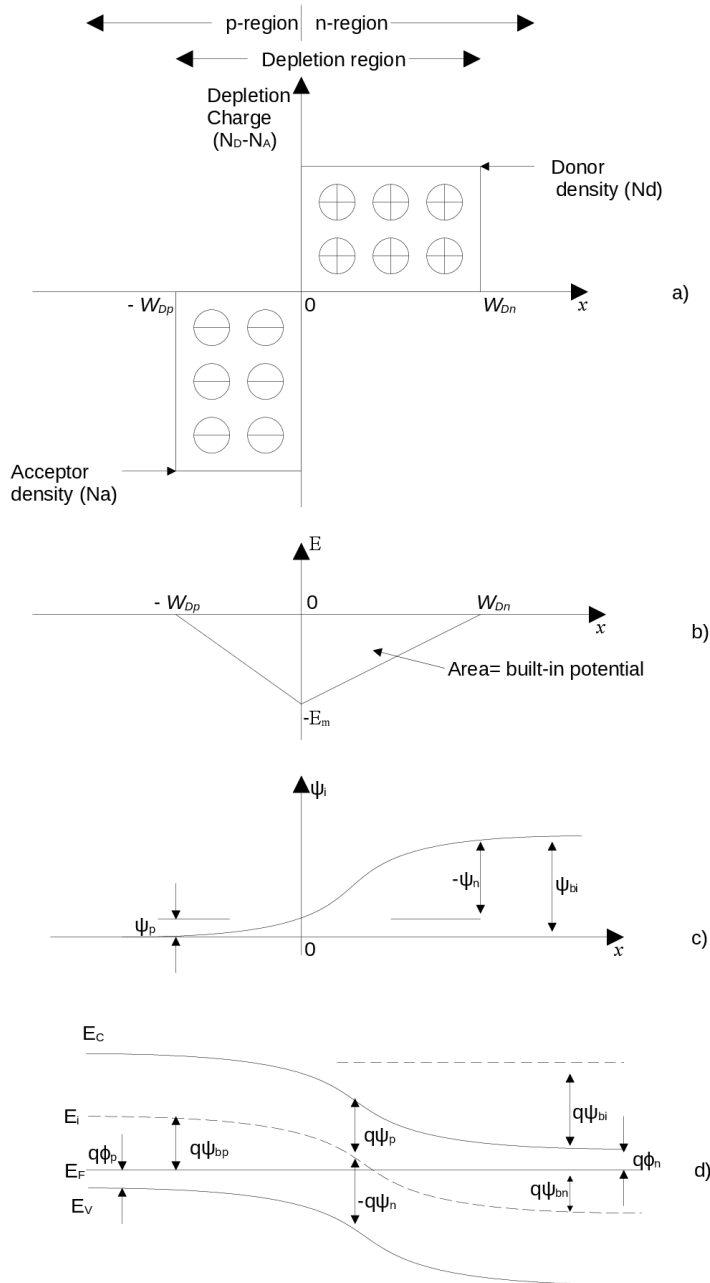


Figure 2.1: An abrupt asymmetric p-n junction in thermal equilibrium. (a) dopant distribution, (b) field distribution, (c) potential variation, and (d) energy band diagram. Modified from [18]

is defined as:

$$\rho(x) = \begin{cases} qN_a, & -x_p \leq x < 0 \\ -qN_d, & 0 < x \leq x_n \end{cases}, \quad (2.2)$$

where q is an elementary charge, N_d and N_a are donor and acceptor atom densities, respectively. From the electrical neutrality of the system the total amount of negative and positive charges in the space charge region has to be equal:

$$N_a x_p = N_d x_n. \quad (2.3)$$

The total width of the space charge region W is given by:

$$W = x_p + x_n. \quad (2.4)$$

For the condition that the electric field $E(x)$ must vanish at both edges of the charge distribution, a first integration of Eq. (2.1) gives an expression for the electric field:

$$E(x) = \frac{d\Phi}{dx} = \begin{cases} \frac{-qN_a}{\epsilon_s}(x + x_p), & -x_p \leq x < 0 \\ \frac{qN_d}{\epsilon_s}(x - x_n), & 0 < x \leq x_n \end{cases}. \quad (2.5)$$

The maximum field strength exists at the pn interface, $x = 0$, and is given by:

$$E_{max} = \frac{qN_d x_n}{\epsilon_s} = \frac{qN_a x_p}{\epsilon_s}. \quad (2.6)$$

Integration of Equation 2.6 over the depletion region gives the potential difference over the SCR with no external bias applied, the built-in potential V_{bi} :

$$V_{bi} = \frac{q}{2\epsilon_s}(N_d x_n^2 + N_a x_p^2) = \frac{1}{2} E_{max} W. \quad (2.7)$$

Combining Eqs. (2.4) and (2.7) yields the relation for the total depletion width as a function of V_{bi} :

$$W = \sqrt{\frac{2\epsilon_s}{q} \left(\frac{N_a + N_d}{N_a N_d} \right) V_{bi}}. \quad (2.8)$$

For the case of one-sided abrupt junction, when $N_a \gg N_d$ (p^+n junction) the expression for total depletion width can be rewritten as:

$$W = \sqrt{\frac{2\epsilon_s V_{bi}}{qN_d}}. \quad (2.9)$$

Application of an external bias voltage V to the p-n junction results in two cases. Forward biasing (positive voltage at the p+ contact) decreases width of SCR, while reverse bias (negative voltage at the p+ contact) increases SCR width. The voltage, at which the space-charge region width equals to the whole sensor bulk thickness d is called the full

depletion voltage V_{fd} , and is given by:

$$V_{fd} = \frac{q}{2\epsilon_s} |N_{eff}| d^2, \quad (2.10)$$

where N_{eff} is the doping concentration of the less doped part.

CV and IV characteristics

The pn-junction can be considered as a capacitor with two conductive areas separated by a non-conducting dielectric. The capacitance C per area of a p-n junction is defined as a ratio between variation of the charge of the depletion layer per unit area, dQ , and change in the applied voltage, dV , and is given as:

$$C = \frac{dQ}{dV} = \frac{dQ}{dW} \frac{dW}{dV}, \quad (2.11)$$

The space charge Q is given by $Q = qN_{eff}AW$, where A is area of the device. The depletion width on the other hand is dependent of the applied voltage. The equation for the total capacitance of the diode can be rewritten as:

$$C = \epsilon_s \frac{A}{W} = A \sqrt{\frac{\epsilon_s q |N_{eff}|}{2(V + V_{bi})}}, \quad \text{for } W \leq d \quad (2.12)$$

After reaching the full depletion voltage, the total depth of the diode contributes to the capacitance and equals to the geometric capacitance, as it depends only on the geometrical size of the device:

$$C = C_{geo} = \epsilon_s \frac{A}{d}, \quad \text{for } W = d \quad (2.13)$$

Figure 2.2b depicts a typical CV curve of a silicon diode. As the full depletion voltage of the diode is the voltage at which the device is depleted throughout its thickness, the capacitance remains constant at higher voltages. Therefore, it is possible to determine V_{fd} value from the CV measurement data. The experimentally obtained V_{fd} values enable determination of the effective doping concentration of the silicon bulk, using equation:

$$N_{eff} = \frac{2\epsilon_s V_{fd}}{qd^2} \quad (2.14)$$

Reverse-biasing of the diode enhances the width of the depletion region. Normally, current carriers do not pass through an insulator, but a small minority carrier current flows through the depletion region, called the leakage current. Since the current is determined by the depleted space charge region, the current depends on the depleted width, which in turn is proportional to the applied bias voltage and saturates as soon as the full depletion is reached.

$$I_{bulk} \propto W \propto \sqrt{V}, \quad \text{for } V \leq V_{fd} \quad (2.15)$$

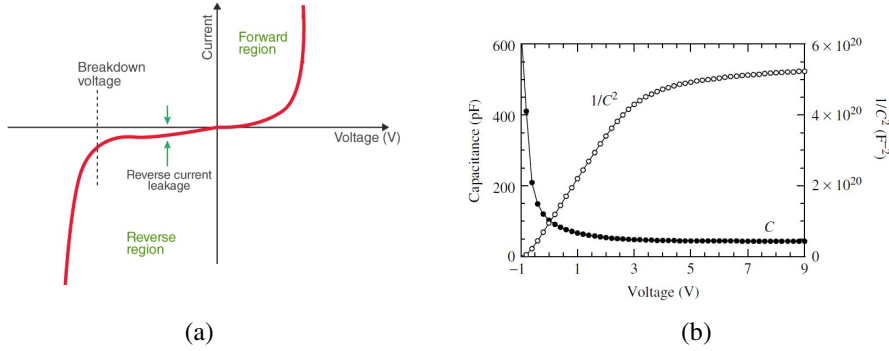


Figure 2.2: a) Typical IV curve for a pn-diode and b) CV and $1/C^2$ curves of a Si n+p diode. Adapted from [19].

The bulk generation current is often described by the generation lifetime τ_g :

$$I_{\text{bulk}} = \frac{qn_i W}{\tau_g} \quad (2.16)$$

where n_i is the intrinsic charge carrier concentration. The n_i implies that only energy levels near the intrinsic Fermi level contribute significantly to the generation current and is a temperature dependent parameter.

2.2 MOS capacitors

A Metal Oxide Semiconductor (MOS) capacitor is a very simple structure and composed of a semiconductor covered with an insulator material on one side and metal contacts on both sides of the device. Silicon dioxide is often utilized as an insulator material for silicon-based structures. However, such dielectrics as aluminium oxide (Al_2O_3) or hafnium oxide (HfO_2) are of particular interest as well. Despite of its simplicity, MOS capacitors are very important structures widely used in semiconductor industry as test structures for the measurement of interface properties.

In order to understand the working principle of the device one needs to comprehend the distribution of the charge carriers in a semiconductor (for instance, of p-type) and at the oxide-semiconductor interface for different external voltages applied between the electrodes of a MOS structure. Depending on the applied voltage, four different modes should be considered, as illustrated in Fig. 2.3: flat-band, accumulation, depletion, and inversion.

Flat-band condition

The work function is defined by the energy necessary to move an electron from Fermi to the vacuum level. Let us consider an ideal case, where work functions for metal and

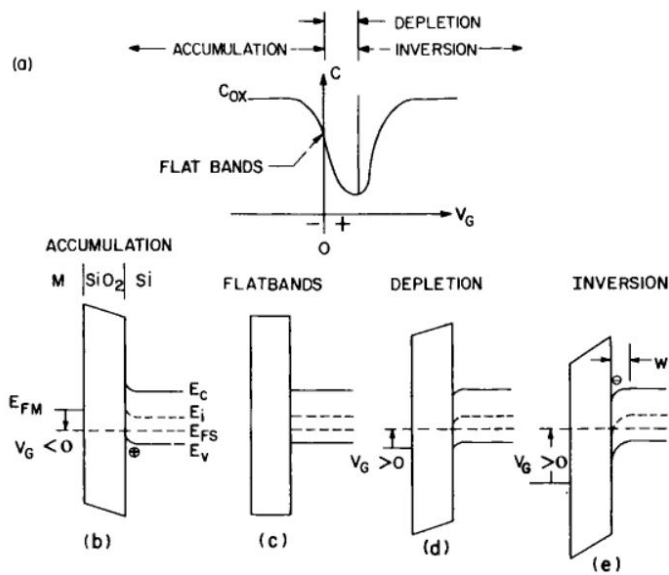


Figure 2.3: The capacitance as a function of bias and the corresponding energy-band diagrams are shown for accumulation, depletion, inversion and flatband cases, where V_G is a biasing voltage, E_{FM} is a metal Fermi energy level, E_{FS} is a semiconductor Fermi energy level, E_C is a semiconductor conduction energy level, E_V is a semiconductor valence energy level, E_i is a semiconductor intrinsic energy level. Taken from [20].

semiconductor are equal. In that case no external voltage is required to get the energy band (E_c and E_v) of the substrate flat at the Si/oxide interface and, therefore, the flat-band voltage V_{fb} is zero, as shown in Fig. 2.3c.

In reality, work functions of different materials are not equal. Thus, the flat-band condition in such a situation can be achieved by application of an external voltage V_{fb} between the metal electrode and the semiconductor to compensate for the difference in work functions:

$$V_{fb} = \Phi_m - \Phi_{Si} \quad (2.17)$$

Accumulation $V < V_{fb}$

The application of voltage less than V_{fb} to the gate, metal electrode over the oxide, pushes the band diagram on the gate side upwards, as shown in Fig. 2.3b. As the Fermi level moves closer to the conduction band edge, a large number of holes accumulates at or near the surface with a surface charge of:

$$Q_{acc} = -C_{ox}(V - V_{fb}), \quad (2.18)$$

where C_{ox} is the oxide capacitance per unit area.

Depletion $V \geq V_{fb}$

In case when a voltage higher than the flat band voltage is applied, the energy bands get pulled downwards, as depicted in Fig. 2.3d. The Fermi level is now far from both E_c and E_v and the concentration of holes near the interface decreases, building up a depleted region. The width of the depletion region is given by:

$$w_{dep} = \sqrt{\frac{2\epsilon_{Si}\psi_s}{qN_a}}, \quad (2.19)$$

where ψ_s is the surface potential.

Inversion $V \gg V_{fb}$

Finally, when a larger positive voltage is applied to the gate, the energy bands bend downwards even more so that the intrinsic level E_i at the surface crosses over the Fermi level, as shown in Fig. 2.3e. As a result, the majority of electrons accumulate at the interface. The surface becomes inverted as a consequence that the amount of electrons (minority carriers) at the surface exceeding that of holes (majority carriers).

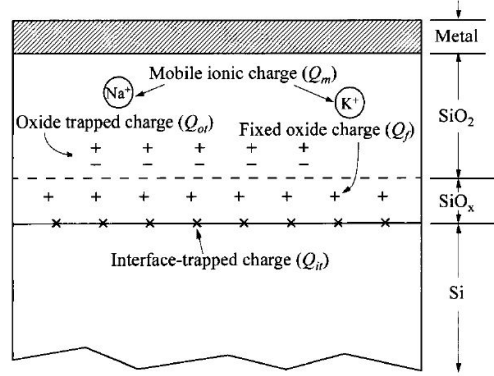


Figure 2.4: Charges and their location for thermally oxidized silicon. Taken from [18]

Oxide charges

In real MOS structures, charges are present inside the oxide and at the Si/oxide interface. There are four common types of traps and charges, as shown in Fig. 2.4: interface-trapped charge, fixed-oxide charge, oxide trapped charge, and mobile ionic charge. These charges and interface traps affect the flat band voltage V_{fb} of a capacitor.

The change in the V_{fb} depends on the amount and distribution of the charges $\rho(x)$ inside the oxide and can be described as:

$$\Delta V_{fb,ox} = \frac{1}{\epsilon_{ox}} \int_0^{d_{ox}} \rho(x)x dx, \quad (2.20)$$

where d_{ox} is oxide thickness and ϵ_{ox} is oxide dielectric constant. Taking into consideration all of the charges that are present in the oxide and the Si/oxide interface, Equation (2.16) takes the form:

$$V_{fb} = \Phi_m - \Phi_{Si} - \frac{Q_{ox}}{C_{ox}} - \frac{Q_{it}(\psi_s)}{C_{ox}}, \quad (2.21)$$

where Q_{ox} is the effective oxide charge and Q_{it} is the interface trapped charge. As occupancy of the interface trap by charges depends on the surface potentials, it is designated as $Q_{it}(\psi_s)$.

The effective concentration of oxide charges can be calculated from V_{fb} using the following equation:

$$N_{eff} = \frac{\Delta V_{fb} C_{ox}}{q}. \quad (2.22)$$

CV characteristic

Capacitance of an MOS structure is measured by variation of voltage applied to the gate. In Fig. 2.5 a CV curve of a p-type MOS capacitor for different fixed oxide charge values is depicted.

With the negative voltage applied to the gate of the p-type MOS capacitor, the accu-

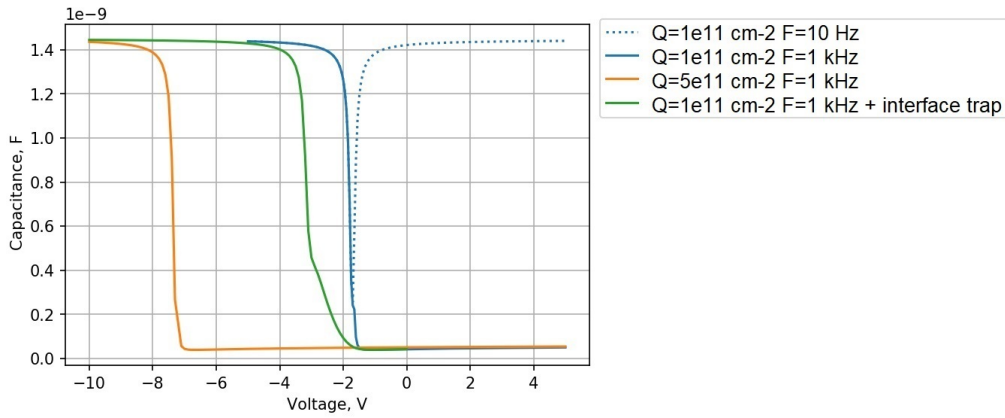


Figure 2.5: Simulated SiO_2/Si capacitance-voltage curves of an MOS capacitor with a p-substrate. The blue curve is calculated for the fixed oxide charge density of $N_{\text{ox}} = 10^{11} \text{ cm}^{-2}$ for 10 Hz (dashed) and 1 kHz (solid). The orange curve represents results for increased fixed oxide charge density equal to $5 \cdot 10^{11} \text{ cm}^{-2}$. The green curve is calculated with the same parameters as the blue one but with added interface trap.

mulation state is established and the capacitance is determined only by the oxide layer $C = C_{\text{ox}}$. Upon increase of the bias voltage, first, the depletion layer arises. Capacitance of the oxide and the depletion layers appear in series, seen in Figure 2.5 as a capacitance drop. Finally, the inversion regime is set with a further sweep to positive voltages. Structure capacitance in the inversion region is strongly frequency-dependent. For low frequencies the capacitance is equal to the one in the accumulation region $C = C_{\text{ox}}$, because minority-carrier generation screens the potential variations across the buried depletion layer. And for high frequencies the measured capacitance again appears as the capacitance of the oxide because the minority carriers are not generated fast enough and there is no formation of an inversion layer at the oxide-silicon interface.

One can also see how oxide charges affect the CV curve in Figure 2.5. The simulated CV characteristic for the fixed oxide charge density value equal to 10^{11} cm^{-2} for 10 Hz (dashed) and 1 kHz (solid) are depicted in blue. The increased value of oxide charge density $N_{\text{ox}} = 5 \cdot 10^{11} \text{ cm}^{-2}$ results in a reduction of the flat band voltage, as shown by the orange curve. A rise in the fixed oxide charge concentration gives a parallel shift of the s-curve. On the other hand, the introduction of a large number of interface traps in addition to the oxide charge results in both: shifting and stretching of the CV characteristic (green curve).

2.3 Metal semiconductor contact

Historically, a metal semiconductor contact or a junction is the oldest semiconductor device [21]. A metal semiconductor junction can be either rectifying or non-rectifying. When metal comes into close contact with a semiconductor material, there can be two

alternatives: the Fermi levels, E_f , of the metal and the semiconductor are at the same energies or at different ones. In the former case, the contact is non-rectifying and is called an ohmic contact. In the latter case, a rectifying metal-semiconductor junction (a Schottky barrier) forms, which is referred as a Schottky contact.

The situation at the Schottky barrier is similar to a p-n junction. When a semiconductor and a metal are joint together, the Fermi levels on both sides have to line up and, therefore, the Fermi level in the semiconductor, in case of n-type bulk, have to be pushed downwards by the amount of difference in the work functions of both materials. Under forward biasing, the potential barrier decreases and carriers diffuse a lot more easily from the semiconductor to the metal. Conversely, under the reverse bias the potential barrier height increases, thereby, establishing a blocking contact. The barrier height can be described by:

$$\begin{aligned} q\Phi_{bn} &= q(\Phi_m - \chi), \quad \text{for n-type Si} \\ q\Phi_{bp} &= E_g - q(\Phi_m - \chi), \quad \text{for p-type Si} \end{aligned} \quad (2.23)$$

where Φ_{bn} and Φ_{bp} are the barrier heights for electrons and for holes respectively, E_g is the bandgap and χ is the electron affinity of the semiconductor.

3 Radiation interactions

The development of the radiation hard detector requires the understanding of the fundamental mechanisms by which radiation interacts with the detector material and loses their energy in matter. The physics of the interaction with the detector material depends strongly on the type of radiation and its energy. In this section the interaction of the four major categories of radiation with matter will be discussed. The four major categories are: heavy charged particles, fast electrons, X-rays and gamma rays, and neutrons. The theory presented in this section is based on Ref. [22, 23].

3.1 Interactions of heavy charged particles with matter

In the present context, by heavy charged particles we understand alpha particles, which are the ionized He atoms. These particles interact with the matter primarily through coulomb forces. The interaction occurs between the positive charge of particles and the negative charge of orbital electrons of atoms of the absorber material. Although the interactions of particles with nuclei are also possible, those are quite rare and mainly take place at the end of the range, when the energy of alpha particles is sufficiently low for such collisions to occur.

Upon entering the medium, electrons feel the impulse from the attractive coulomb force as particles pass by. This impulse may be sufficient enough to raise the electron to a higher energy shell within the atom (excitation) or to remove the electron completely from the atom (ionization). The charged particle immediately interacts with many electrons. Heavy charged particles can transfer only a small fraction of their energy in a single collision. The maximum energy that can be transferred from a charged particle of mass m with kinetic energy E to an electron of mass m_0 in a single collision is $4Em_0/m$. Therefore, alpha particles travel along almost straight paths through matter, losing energy continuously through a large number of collisions with atomic electrons. At the end of the path of motion there is a deviation from the straight line due to nuclear collisions [23]. However, the deviation from the straight line will be not very significant as compared to the total length of particle path and hence can be approximated as such.

If a heavy charged particle transfers a sufficient impulse to an electron, it can travel a short distance from the original track of the particle. In cases where the energy of the electron is high enough to further ionize surrounding atoms, it is called a delta ray. Therefore, ionization clusters occur around the path of the particle.

The linear stopping power S for charged particles in a given absorber is defined as the differential energy loss for the particle within the material divided by the corresponding differential path length:

$$S = -\frac{dE}{dx} \quad (3.1)$$

The value $-dE/dx$ along a particle track is called specific energy loss. The classic ex-

pression that describes the specific energy loss is known as the Beth formula:

$$-\frac{dE}{dx} = \frac{4\pi e^4 z^2 N Z}{m_0 v^2} \left(\ln\left(\frac{2m_0 v^2}{I}\right) - \ln\left(1 - \frac{v^2}{c^2}\right) - \frac{v^2}{c^2} \right) \quad (3.2)$$

where v and ze are the velocity and charge of the primary particle, N and Z are the number density and atomic number of the absorber atoms, m_0 is the electron rest mass, and e is the electronic charge. The parameter I represents the average excitation and ionization potential of the absorber, which depends on the orbital frequency of the absorbing material and is normally treated as an experimentally determined parameter for each element. When the velocity is comparable with the speed of orbital electrons of the target material, the energy loss reaches a maximum depending on the sign of the charge and for lower energy drops sharply. At higher energy, the energy loss decreases until a minimum is reached. Particles with minimal energy loss in the media are called Minimum Ionizing Particles (MIP). The minimum value of dE/dx is almost the same for all particles of the same charge.

The Beth formula has some limitations: It is based on the assumption that the particle moves much faster than atomic electrons; the density effect, which can be described as atom polarization in medium screening the electromagnetic field far from particle path, therefore reducing the stopping power, should be taken into account, and it begins to fail at low particle energies where charge exchange between particle and the absorber becomes important.

The linear stopping power of a material also depends on the density of electrons within the absorber material, therefore on the atomic number of the target, as well as the energy of the particle. Another way of describing the rate of energy loss is to specify the rate in terms of the density thickness, rather than the geometric length of the path. This quantity is called mass stopping power:

$$S_m = -\frac{dE}{d\rho x} = -\frac{1}{\rho} \frac{dE}{dx} \quad (3.3)$$

where ρ is the density of the material and ρx is the density-thickness.

A plot of specific energy loss along the track of a charged particle is known as a Bragg curve Fig. 3.1. For heavy charged particles, the interaction cross-section increases as the particle's energy decreases. The energy loss of the heavy charged particles is inversely proportional to the square of their velocity, therefore the Bragg peak occurs before the particles come to rest. However, one can see that the peak has a spread due to interactions with nuclei at the end of the path.

A definite range in a given medium represents a distance beyond which no particles will penetrate. For a given material, the range will be nearly the same for all particles of the same kind with the same initial energy. Because the details of the microscopic interactions undergone by any specific particle vary randomly, a small variation in the range can be

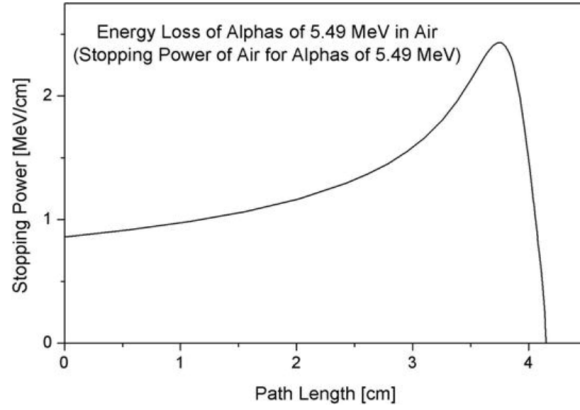


Figure 3.1: The specific energy loss along the heavy particle track. Adapted from [22].

observed. This variation is called straggling, and it is caused by the statistical nature of the energy loss process, which consists of many individual collisions. The range of alpha particles is of a cm scale in air and a micron scale in solids.

3.2 Interactions of fast electrons with matter

Fast electrons interact with matter primarily through coulomb forces. However, fast electrons lose their energy at a lower rate and have a much more tortuous path through the material because of elastic scattering from nuclei. These deviations from the straight paths can be explained by the fact that the mass of fast electrons are equal to that of orbital electrons. Therefore, a much larger fraction of energy can be transferred in a single collision. In addition, inelastic collisions with atomic electrons can sometimes occur (excitation and ionization). The specific energy loss due to ionization and excitation (the 'collisional losses') for fast electrons has been derived by Bethe:

$$-\frac{dE}{dx} = \frac{2\pi e^4 N Z}{m_0 v^2} \left(\ln \frac{m_0 v^2 E}{2I^2(1-\beta^2)} - \ln(2)(2\sqrt{1-\beta^2} - 1 + \beta^2) + (1-\beta^2) + \frac{1}{8}(1-\sqrt{1-\beta^2})^2 \right) \quad (3.4)$$

Fast electrons can also lose energy by means of radiative processes. These radiative losses take the form of bremsstrahlung radiation, which is produced by the deceleration of electrons by the atomic nucleus. The bremsstrahlung process becomes increasingly important at higher energy, in the MeV range. The ratio between the energy losses due to ionization-excitation and bremsstrahlung is approximately given by:

$$\frac{-\frac{dE}{dx} \text{ bremsstrahlung}}{-\frac{dE}{dx} \text{ collision}} = \frac{ZE(\text{MeV})}{800} \quad (3.5)$$

There is another mechanism by which fast electrons lose their energy via the production of electromagnetic radiation. When an electron moves faster than the phase velocity of light in the material, it generates a shock wave of electromagnetic radiation known as Cherenkov radiation. However, the energy loss via Cherenkov radiation is much lower than via any other mechanism, and it can be used to detect high-energy charged particles.

Positrons interact similarly with matter when they are energetic. But when the positron comes to rest, it interacts with a negatively charged electron, resulting in the annihilation of the electron-positron pair, resulting in a pair of back-to-back photons with an energy of 511 keV each.

3.3 Interactions of X-rays and gamma rays with matter

Interactions of X-rays and gamma rays with matter are similar, whereas the origin of these two rays are different. Gamma rays are produced by the nuclear transitions, while X-rays are produced by energy transitions due to accelerating electrons. There are three major types of interaction mechanisms that occur when gamma rays and x-rays interplay with matter: photoelectric absorption, Compton scattering and pair production. All these processes dominate at different energy ranges, as shown in Fig. 3.2, and lead to the partial or complete transfer of gamma-ray photon energy to electron energy. In the contrast to charged particle interactions with matter, gamma-ray interactions result in abrupt changes: either the photon disappears or it is scattered through a significant angle.

Photoelectric absorption

In photoelectric absorption, a photon is absorbed by an electron of an absorber atom. The photon transfers its energy into kinetic energy of the electron, therefore the energetic photoelectron is ejected from one of its bound shells and begins to pass through the surrounding matter. The electron rapidly loses its energy and moves only a relatively short distance from its original location. The photon's energy is, therefore, deposited in the matter close to the site of the photoelectric interaction. Photoelectric interactions are most probable when the electron binding energy is only slightly less than the energy of the photon. If the binding energy is more than the energy of the photon, a photoelectric interaction cannot occur.

In addition to the photoelectron, an ionized absorber atom with a vacancy in one of its bound shells is created. The vacancy is quickly filled by capturing a free electron from the medium or by rearrangement of the electrons from other shells of the atom. Therefore, one or more characteristic x-ray may be generated.

The photoelectric absorption dominates at relatively low energy (up to hundreds of keV) and the process is also enhanced for absorber material of a high atomic number Z .

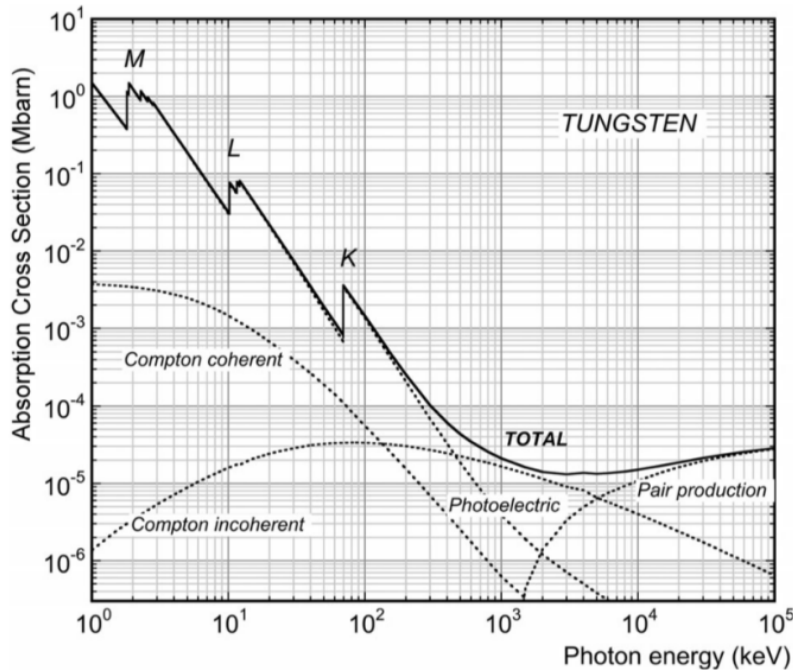


Figure 3.2: Absorption cross-section of photon in W target. Taken from [24].

Compton scattering

The interaction process of Compton scattering takes place between the incident gamma-ray photon and an electron in the absorbing material. The incoming gamma-ray photon transfers a portion of its energy to the electron and is then deflected by a Compton angle with the respect to its original direction, as shown in Fig. 7.2. The Compton angle depends on the energy lost to the electron. The probability of Compton scattering per atom of the absorber depends on the number of electrons available as scattering targets and therefore increases linearly with the atomic number Z .

In a low energy region another type of scattering can occur in which gamma-ray photons interact coherently with the electrons of the absorber atoms. During this process no excitation or ionization of atoms appear and the gamma photons preserve their original energy; however, the direction of photons are changed. Because no transfer of energy happens, the mechanism could be neglected in the present study.

Pair production

Pair production occurs only when photons have energy that exceeds twice the rest-mass of an electron (1.02 MeV). In pair production interaction, the photon is absorbed by the nucleus and an electron-positron pair is emitted. Positrons will normally annihilate quickly into two photons as a secondary products of the interaction. Pair production is completely

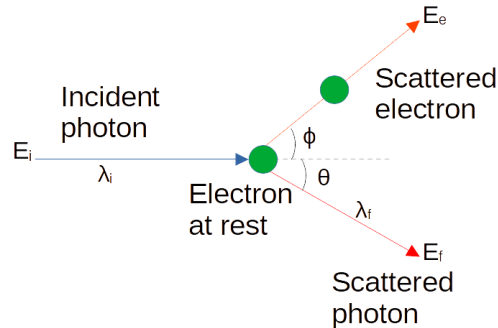


Figure 3.3: Sketch of the Compton scattering mechanism, where λ_i is the incident photon wavelength, λ_f is the scattered photon wavelength with the photon scattered by an angle θ , and the electron recoiling at an angle ϕ

dominating at high photon energies, as can be seen from Fig. 3.2.

3.4 Interactions of neutrons with matter

Similarly to gamma rays, neutrons carry no charge; therefore they do not interact electromagnetically with electrons of nuclei in matter. Neutrons can travel through many centimeters of matter without any type of interactions. Neutrons mainly undergo interactions with the nuclei of the absorbing material. The main interaction processes are elastic scattering, inelastic scattering, radiative capture, and other less frequent nuclear processes. The probabilities of the various types of neutron interactions strongly depend on the neutron energy.

For slow neutrons, that is, neutrons whose kinetic energy is below about 0.5 eV, an elastic scattering and neutron-induced nuclear reaction are much more probable. In an elastic scattering the total kinetic energy is conserved. When a neutron scatters elastically from a nucleus it transfers some of its kinetic energy to the nucleus, but the nucleus remains unexcited. Because the neutron is small in comparison with the most nuclei, it does not lose much energy in each collision and it can take many collisions before it loses its full kinetic energy.

In inelastic scattering and capture processes, some or all of the neutron energy is absorbed by the nucleus that is left in an excited state. Later it decays by emitting gamma rays or other particles that are almost always heavy charged particles. The emitted photon gives a recoil energy to the atom, which can initiate a cascade of atomic collisions, creating a localized regions of disorder [25, 26]. The capture processes occur more readily for slow neutrons, while inelastic scattering is most important for fast neutrons with kinetic energies more than about 100 keV.

4 Particle detectors

4.1 Silicon tracking sensors

As has been discussed in Section 2.1, a simple particle detector is a reversed biased p-n junction, ideally with the depletion region widened over the entire thickness of the device, thus leaving a space charge region without mobile carriers. An incident charged particle or a photon traversing through the detector body excites electrons from the valence to the conduction band, creating free electron-hole pairs along its track. Electron-hole pairs split and the charge carriers drift in the opposite directions due to the present electric field. The motion of the carriers generates a current that, according to the Shockley-Ramo theorem [27, 28], is proportional to the charge carrier drift velocity v and the weighting field E_w :

$$I = qvE_w \quad (4.1)$$

The energy required to create an electron-hole pair in silicon at room temperature is 3.6 eV. Even though the bandgap is 1.12 eV, silicon is an indirect semiconductor and an extra energy is needed for the momentum conversion [29].

The charge collection efficiency of the detector can be improved by employing a higher mobility of electrons in comparison to holes. Therefore, recent silicon detectors consist of a p-type bulk with a heavily doped n-type region on the front of the device, denoted as n+, and a heavily doped p-type region on the back electrode as a blocking contact. Position sensitivity is acquired by dividing the detector surface electrode along with the n+ implants into segments: pixel sensors in two dimensions and strip detectors in only one. The addition of a guard ring structure assures a precisely defined active volume of a pixel sensor.

In order to electrically separate segmented n+ implants from each other, p-stop or p-spray structures are often used [11]. As traditionally utilized silicon dioxide possesses a positive oxide charge, this leads to a formation of short-circuiting channels between the n+ segments. Therefore, isolating these structures requires additional implantation and high-temperature processing steps, as well as more space on the detector. An alternative is to use thin films of a field insulator with the negative oxide charge between segments, as shown in Fig. 4.1. The main candidates are HfO_2 and Al_2O_3 as they have good dielectric properties and possess a high negative charge of the order of $10^{11} - 10^{13} \text{ cm}^{-2}$ [12, 13]. One way to fabricate these insulating thin films is by atomic layer deposition (ALD), which requires rather low temperatures within the range of 200-300 °C and is beneficial in providing very conformal thin films (of tens of nm) with uniform thickness and good accuracy [30, 31]. Detailed information about the processing of the detectors can be found in Refs. [32–35].

Traditionally, for DC-coupled devices, the measurement signal that is read out comes from strips or pixels combined with the leakage current. On the other hand, AC-coupled detectors separate the signal from the leakage current by using strip or pixel capacitors.

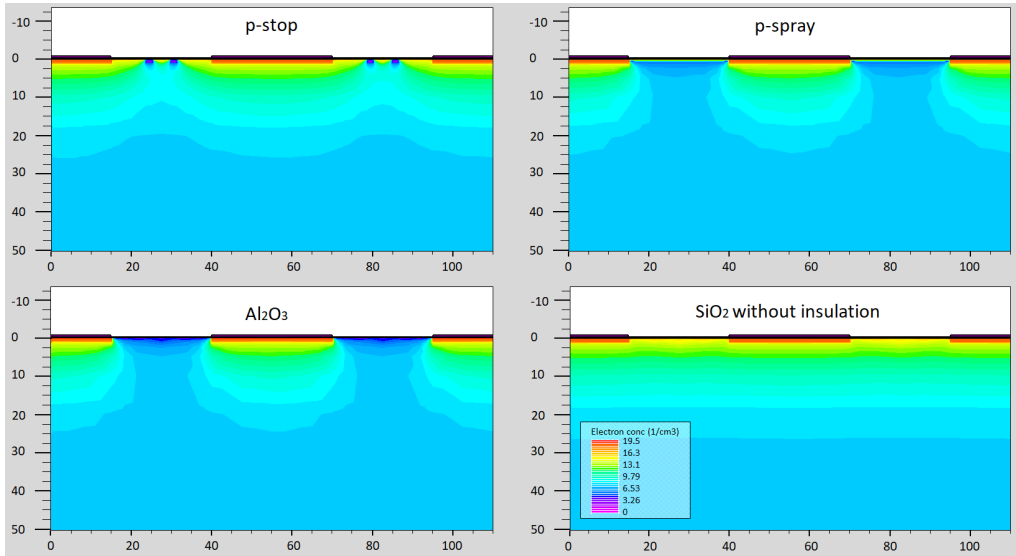


Figure 4.1: Simulated electron density distribution for segmented n+p type detector with different inter-segment insulation structures: SiO_2 without any inter-segment insulation, with p-stop, with p-spray, and with only Al_2O_3 thin film. Axes in microns.

The signal is measured through the capacitor, while the leakage current goes to the common bias line via a bias resistor.

Sensors suffer from the radiation-induced damage in the silicon bulk as well as at the silicon/oxide interface during their lifetime. In order to anticipate possible sensor degradation, it is important to have a model that can predict the behavior of the detector for high fluence irradiation.

4.2 CVD diamond radiation detectors

High energy physics is in constant search of radiation detectors that can withstand severe radiation damage and still operate with a good level of signal-to-noise ratio. Diamonds have a number of attractive properties, which are essential for durable radiation detectors [36, 37]. Apart from being the hardest material, many physical properties of diamond outstrip those of silicon. A comparison between the main properties of Si, diamond and CdTe is provided in Table 4.1. The low value of the intrinsic carrier concentration gives diamond the capability of operating at much higher temperatures compared to Si. Another advantage caused by the low intrinsic carrier concentration is the low leakage current. According to equation 2.16, the lower the intrinsic carrier concentration, the smaller the leakage current is. Large bandgap, high charge mobility, high resistivity, high breakdown voltage, and low dielectric constant result in low-noise fast signal responses. Additionally, the large displacement energy of diamond, arising from perfect tetrahedral bonding of carbon atoms, indicates its inherent radiation tolerance. Furthermore, diamond has a

very high thermal conductivity of 24 W/cmK that allows it to be cooled very effectively.

From a technological point of view, diamond-based detectors can have simple designs (diamond plate with front and back electrodes) that do not require fabrication of p - n junctions which are necessary in the production of silicon radiation detectors.

	Si	CVD diamond	CdTe
Band gap (eV)	1.2	5.47	1.47
Intrinsic carrier concentration at 300 K (cm^{-3})	$1.5 \cdot 10^{10}$	$1.1 \cdot 10^{-27}$	$1 \cdot 10^7$
Breakdown field (MV/cm)	0.3	20	
Electron mobility (cm^2/Vs)	1100	4500	1000
Hole mobility (cm^2/Vs)	480	3800	80
Relative electric permittivity	11.8	5.7	10.2

Table 4.1: Comparison between the electrical properties of Si, CVD diamond and CdTe. [38–40]

Based on such outstanding properties and recent achievements in manufacturing of single crystal scCVD diamonds, diamonds can be found in extremely harsh radiation environments, where timing and radiation sustainability are of high importance. For instance, diamond detectors are currently used in beam condition monitoring and particle tracking systems for the LHC (CERN) [41–43] and in the CMS-TOTEM Precision Proton Spectrometer [44–46].

However, despite the excellent electrical properties and radiation hardness of diamonds, signal degradation was observed in heavily irradiated diamond sensors due to a polarization effect [47]. Charge carriers generated by radiation fill deep level traps originating from radiation damage defects, which are further described in Section 5. Thereby, space charge builds up in the diamond bulk and perturbs the biasing external electric field. The altered electric field leads to changes in charge carrier transport inside the sensor and as a result, the collected signal degrades. Therefore, numerical simulations can help in describing the polarization effect in diamonds.

4.3 CdTe radiation detectors

Cadmium Telluride is a promising material for room temperature detection of X-ray and gamma-ray radiation. It has a relatively large band gap, 1.47 eV at 300 K, resulting in a small thermal noise in end-use devices. Another outstanding characteristic of this semiconductor material is its high atomic number of 50, which allows strong absorption and good detection efficiency for high-energy photons [48, 49].

The CdTe is a compound material and crystal defects are common issue, thus it has relatively poor carrier transport properties. In particular, hole mobility and lifetime are quite low compared to other competitors, as shown in Table 4.1. Undoped CdTe is a typically strongly p-type due to the presence of a large number of acceptor-like cadmium vacancies in the crystal lattice [50]. Chlorine is used to compensate for the acceptor vacancies in the crystal and thus to improve the charge transport [51]. The resulting crystal remains slightly p-type after this procedure.

CdTe detectors suffer from crystal impurities such as Te-inclusions and -defects, dislocation networks, and twin- and sub-grain boundaries, which affect the detector performance [52]. Defects and impurities at the grain boundaries can trap charge carriers and also act as charge drains, which can be seen as fluctuations in the collected signal and locally reduced charge collection efficiency [53]. Thus, quality assessment before the complex detector processing procedure is important. The employment of infrared microscopy (IRM) can help in the evaluation of the defect density inside the crystals [54], as the compound material is mostly transparent in near-infrared light, but the Te inclusions are opaque for light in this region [55]. The combination of simulations and measurement results with Transient Current Technique (TCT) (Publications II and III) and the knowledge of the defect density in the measured area can help understand the impact of these defects on detector efficiency.

5 Radiation damage in silicon detectors

In reality, it is impossible to have a perfect crystal without any imperfections. Defects and impurities, which are present in materials, can affect their properties. Defects that are found in semiconductors can be classified into three main categories:

1. Substitutional impurities; where the atom in a lattice site is replaced with a different atom
2. Native defects; crystallographic defects such as vacancies or interstitials, also commonly known as point defects
3. Clusters; these defects are formed by the combination of two or more defects

As an illustration, the most common types of the point defects are presented in the two-dimensional lattice in Fig. 5.1a: empty lattice sites (vacancies); additional atoms of the same or a foreign nature between regular lattice sites (interstitials); and pairs of interstitials next to vacancies (Frenkel pair). The density of defects in semiconductors composed of two elements, such as CdTe, is usually larger than in single element crystals. Defects can be generated during the crystal growth or during device processing, as well as when the semiconductor is irradiated.

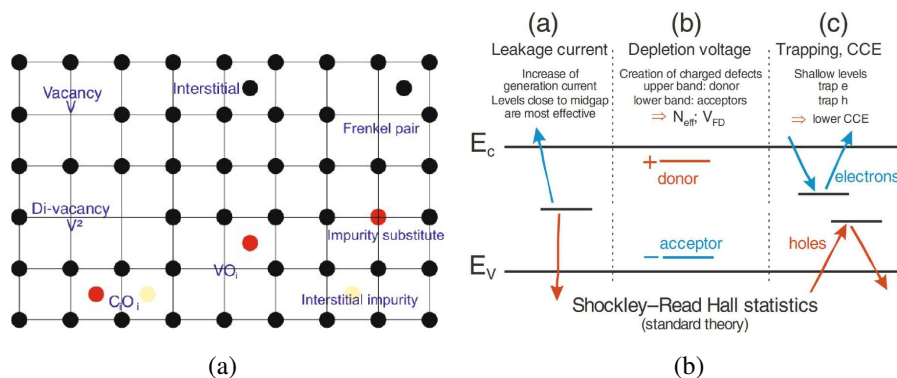


Figure 5.1: Illustration of a) important defects in semiconductor and b) the defect energy levels responsible for the change of silicon properties. Adapted from [56].

From the energy consideration point of view, defects form additional states in the band gap of the semiconductor. Depending on their energy levels with respect to the valence and conduction bands in silicon, these defects act in different ways, as visualized in Fig. 5.1b: defects with energy levels close to the middle of the band gap can act as recombination/generation centers, thus increasing the leakage current; shallow levels can contribute to the effective charge density in the space charge region; and deep levels can act as trapping centers and re-emit with some time delay, hence lowering the CCE [57].

The damage caused by irradiation can be divided into surface and bulk damage. In both cases the ionization and dislocation of atoms takes place. While the generation of electron-hole pairs by ionization does not produce any permanent damage to the bulk and can be reversible, the dislocation of atoms from the silicon lattice causes permanent damage. The surface damage occurs due to the ionizing energy loss of charged particles and creates extra fixed charges in the oxide and the oxide-Si interface. The theory presented in this section is based on Refs. [57, 58].

5.1 Bulk damage

Microscopic damage in the silicon bulk due to radiation interaction with the matter leads to macroscopic changes of the device characteristics such as: changes in depletion voltage and bulk doping concentration, degradation of CCE, and increase in leakage current.

The removal of a silicon atom from its lattice position requires a minimum recoil energy of about 25 eV [59]. A particle with energy above this minimum value is able to kick out a silicon atom from its lattice site, leaving a vacancy-interstitial pair instead. For higher recoil energies above ~ 5 keV, further defects are created, referred to as defect clusters [60, 61]. Cluster defects are a dense agglomeration of point defects that can reach sizes of tens of nanometers wide [62]. They have a more critical effect on the properties of semiconductor devices than point defects [63].

The probability of the creation of the primary knock-on atom depends on the type and energy of irradiation. Charged particles interact mainly via Coulomb interactions with the atoms of the silicon lattice, while neutrons scatter elastically with the nucleus. The energy transferred to the silicon atom is strongly dependent of the mass of the impinging radiation. In order to compare the radiation-induced damage of different particles and different energies, the concept of scaling different radiation types and energies to non-ionizing energy loss (NIEL) as 1 MeV neutron equivalents based on bulk leakage currents has been established [61].

Both cluster and point defects have a strong impact on the device properties depending on the defect parameters, such as: concentration, energy level, and the respective electron and hole capture cross-sections. Defects with deep energy levels in the middle of the forbidden gap can act as recombination/generation centers capturing and re-emitting electrons and holes, and are therefore responsible for an increase of the inverse detector current. The dependence of the current per unit volume can be parameterized as [9]:

$$\Delta I = \alpha \Phi, \quad (5.1)$$

where α is called the current related damage rate. As seen from the 5.1, the increase in the leakage current is proportional to the fluence.

High leakage currents lead to the deterioration of the signal-to-noise ratio and also to

an increase in the power consumption of the entire detector system. Bulk doping determines the effective space charge. The original dopants, such as phosphorus or boron, may be captured into new defect complexes that result in the change of the effective doping concentration or even deactivation of the doping of the semiconductor [64]. This affects the electric field distribution within the body of the semiconductor and changes the full depletion voltage. In case of full depletion voltage shift to higher biasing values, the detector is operated under-depleted, thus losing a portion of the measurement signal. Finally, radiation-induced defects can also act as trapping centers affecting the CCE [65]. Due to trapping, the charge is released too late to contribute to the signal, so fewer charge carriers reach the electrodes and a reduced signal is read out [66, 67].

5.2 Surface damage

The term surface damage refers to overall damage in the surface dielectric and the interface of the surface dielectric and bulk silicon. The surface is a very critical part of the device because already without any irradiation the crystal structure is highly irregular near the surface. Therefore, one can consider the oxide and oxide-silicon interface as a region with a high number of defects. The additional damage to the oxide crystal structure by the interaction of the radiation with nuclei is not so important, but the ionizing irradiation is crucial for surface damage. It consists of a change in the effective oxide charge in the oxide and an increase in the interface traps near the interface with silicon [68]. That can be seen in the shift in the flat-band voltage of the MOS structure and the change to the slope of the CV curve. In case of the SiO_2 , accumulation of positive charges in the insulator oxide and the formation of silicon-oxide interface traps increases the inter-segment capacitance in segmented detectors, which in turn increases the electronic noise. Surface damage is crucial, especially for AC-coupled sensors, because their electrical properties are very prone to changes at the surface. In the case of alumina, as it possesses a negative oxide charge [69], a change in the flat-band voltage to negative values can lead to a loss of the isolation between strips or pixels (Publication IV).

6 Simulation of defects

There are several providers of commercial simulation software packages, including Synopsys and Silvaco. In this work Synopsys Sentaurus TCAD (Synopsys) has been used for device simulations [70]. The Sentaurus Workbench is a framework designed to make the use of Synopsys TCAD tools easier. Several tools can be run in a series to generate a desirable device structure (Sentaurus Structure Editor) and to numerically reproduce the electrical behavior of devices (Sentaurus Device). Finally, to analyze the results of the simulation, the Sentaurus Visual tool is used. The whole silicon device manufacturing process is also possible to simulate with the use of the Sentaurus Process tool.

Initially, the required device has to be modeled. Every simulated device is described by a file that contains information about the geometry of the structure (description of the various regions, boundaries, materials, contacts shape, location, etc.) and the doping profiles. Then, the mesh is generated and this file is given as input to the Sentaurus Device tool so that the selected equations can be solved for each of these points of the grid. The equations that are needed to simulate the behavior of the semiconductor device are the Poisson equation and the electron and hole continuity equations, which are derived by replacing the derivatives of a function by differences taken on a grid. Below are once again the Poisson equation and electron and hole continuity equations:

$$-\frac{d^2\Phi}{dx^2} = \frac{dE}{dx} = \frac{\rho(x)}{\epsilon_s}, \quad (6.1)$$

$$\frac{dn}{dt} = \mu_n n \Delta E + D_n \Delta^2 n + G_n - R_n, \quad (6.2)$$

$$\frac{dp}{dt} = \mu_p p \Delta E + D_p \Delta^2 p + G_p - R_p, \quad (6.3)$$

where E is the electric field, q is the elementary charge, ϵ_s is the permittivity of the material, n is the electron density, p is the hole density, G is the generation rate, R is the recombination rate, μ is the mobility of the carrier, and D is the diffusion constant.

The device structure can be simulated in 2D and in 3D. 2D models need much fewer mesh points and therefore the simulation needs less computing time and memory. On the other hand, 3D models are much closer to the reality but they need a huge amount of mesh points, computing time, and memory to be performed.

The command file of the Sentaurus Device tool consists of the following sections:

1. File: all the input and output files needed for the simulation are specified in this section;
2. Electrode: all the electrodes of the system are defined;

3. Physics: all the physical models that are needed for numerical calculation are listed. These models can be applied for different interfaces, regions, or materials;
4. System: an external circuit can be specified here;
5. Plot: in this section the characteristics to be saved and plotted are defined;
6. Math: in this section the proper mathematical methods and error sized are listed;
7. Solve: here the type of analysis is specified (Quasistationary, Transient, and AC-Coupled);

Synopsys Sentaurus TCAD uses a set of internally defined parameters for each material. However, not all of the materials are included in the material libraries. Diamond material, CdTe, Al₂O₃ for instance, is not included in the material libraries of the Sentaurus simulation tools, but TCAD allows user-defined materials to be introduced or existing materials' entries to be modified. Therefore, a new material entry can be created, where all the physical parameters of the new material, such as permittivity, optical refractive index, and band gap, are defined by hand using data from literature. In the scope of this thesis, diamond material, CdTe, and Al₂O₃ were implemented in TCAD.

As was discussed in the previous section, radiation causes ionization and displacement of atoms in the material. The actual displacement of atoms from the lattice sites cannot be simulated, but we can consider these defects as energy levels in the energy band of the silicon. This can be simulated and the impact on the detector performance can be described in the framework of Shockley-Read-Hall (SRH) statistics [71, 72]. In principle, the variation of the defect parameters, such as capture cross-sections for holes and electrons, the position in the bandgap, the type of defect (acceptor or donor), and the concentration of the defect can give us the impact of each of the parameters on the sensor operation. The same principles can be utilized for the point defects. The following example shows one trap implementation in the silicon material:

```
Physics(Material = "Silicon")
{
Traps(Acceptor Level EnergyMid=0.5
fromCondBand conc=1e14 eXsection=1e-16
hXsection=1e-15)
}
```

The code is quite easy to understand. In the Physics section where all the physical models are described, the material to which the traps are applied is silicon. The trap type that is used in this example is an acceptor with a discrete level and an energy of 0.5 eV calculating from the conduction band. The concentration of the traps are 1e14 cm⁻³ and the electron and hole capture cross-sections are 1e-16 cm² and 1e-15 cm² respectively.

Before the building of the defect simulation model, the evaluation of the simulation prior to the irradiation has to be performed. This is done by a comparison of the simulation results to the corresponding laboratory measurements performed under equivalent conditions. This makes it possible to investigate the effects of the basic simulation parameters as well as geometry and process parameters. For the surface damage simulations, the results are compared to the CV laboratory measurements of MOS capacitors as well as IV curves of a MOSFET (Publication IV). The reliability of the simulated electric field distribution can be examined by comparing measured and simulated transient current curves.

7 Results and discussions

7.1 Simulation study of MOS capacitor and silicon detectors with Al_2O_3 and HfO_2 thin films

This study was motivated by the need to verify the characterization measurements of the heavily irradiated AC-coupling insulator thin films as well as to investigate the radiation-induced surface damage of aluminum oxide thin films (Publication IV).

For surface damage investigation, a simple structure of the MOS capacitor is the most appropriate one. MOS capacitors represent simple devices used to study semiconductor surface behavior after radiation damage. For this reason, the layout in the simulation can be kept very simple. Thus, the simulated MOS capacitor structure had the dimensions $A \times 1 \times 1 \mu\text{m}^3$, where A is the area factor to match the dimensions with the real device. Two types of passivation layers were investigated, alumina-only with a thickness of 84 nm, and hafnia on top of alumina with thicknesses of 84 nm and 63 nm, correspondingly. The bulk doping concentration was set to $6 \cdot 10^{11} \text{ cm}^{-3}$. The reverse voltage was provided from the backplane contact.

Flatband voltage V_{fb} shift can be easily estimated from the measurements. Using Equation (2.22), the effective oxide charge concentration, increased at the silicon/oxide interface due to irradiation, can be assessed. These variables are then used as input parameters for the TCAD surface damage model. As was discussed in Section 2.2, the oxide/Si interface is also characterized by interface traps distributed throughout the silicon energy gap. From a macroscopic point of view, they induce a stretching-out of the high-frequency capacitance-voltage curve. The interface trap states density D_{it} can be instead estimated by means of the capacitance high-low method [19]. Due to the technical limitations of the probing setup, only high-frequency CV curves for MOS capacitors were obtained. Therefore, the D_{it} were found by fitting simulated CV curves to the measurement results. The interface states were modeled with two single trap levels, one donor at 0.50 eV from the valence band edge and one acceptor at 0.50 eV from the conduction band edge. All the parameters that were used for the surface damage model are listed in Table 7.1.

The simulated CV curves for the MOS capacitor with alumina and alumina/hafnia as an insulators are shown in Fig. 7.1. One can see that for the first radiation fluence step there is only an increase in the effective oxide charge with no change in the interface trap concentration. However, for the highest fluence dose, an increase in the interface trap concentration occurs. The simulation adds the evidence to the fact that the interface traps play an important role for higher fluences.

Another type of structure that was used to study the surface damage was a MOS field-effect transistor (MOSFET). The schematic of a n-channel MOSFET is shown in Fig. 7.2. A p-type Si substrate with two n+ regions, called drain and source, forms a n-channel MOSFET. A metal plate on top of the oxide, in our case alumina and alumina/hafnia, is

Type of trap	Level (eV)	σ_e (cm ²)	σ_h (cm ²)	Fluence(protons/cm ²)	Density (cm ⁻²)
Donor	$E_v + 0.5$	$1 \cdot 10^{-16}$	$1 \cdot 10^{-15}$	0	$5 \cdot 10^{11}$
Acceptor	$E_c - 0.5$	$1 \cdot 10^{-15}$	$1 \cdot 10^{-16}$	0	$5 \cdot 10^{11}$
Donor	$E_v + 0.5$	$1 \cdot 10^{-16}$	$1 \cdot 10^{-15}$	$5 \cdot 10^{12}$	$5 \cdot 10^{11}$
Acceptor	$E_c - 0.5$	$1 \cdot 10^{-15}$	$1 \cdot 10^{-16}$	$5 \cdot 10^{12}$	$5 \cdot 10^{11}$
Donor	$E_v + 0.5$	$1 \cdot 10^{-16}$	$1 \cdot 10^{-15}$	$5 \cdot 10^{15}$	$7 \cdot 10^{12}$
Acceptor	$E_c - 0.5$	$1 \cdot 10^{-15}$	$1 \cdot 10^{-16}$	$5 \cdot 10^{15}$	$3 \cdot 10^{12}$

Fluence(protons/cm ²)	Oxide charge Density (cm ⁻²)
0	$-2 \cdot 10^{12}$
$5 \cdot 10^{12}$	$-4.8 \cdot 10^{12}$
$5 \cdot 10^{15}$	$-3 \cdot 10^{12}$

Table 7.1: Details of surface damage model.

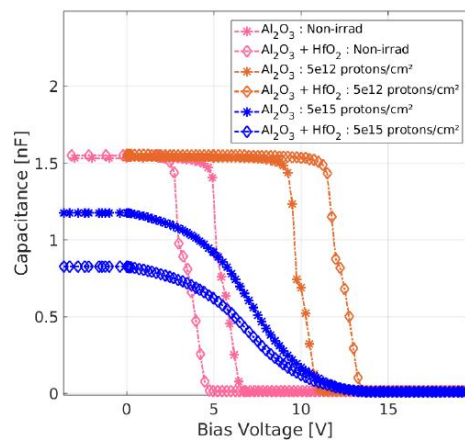


Figure 7.1: Simulated CV curves of non-irradiated and irradiated MOS capacitors with alumina and hafnia as a dielectric (Publication IV).

7.1 Simulation study of MOS capacitor and silicon detectors with Al_2O_3 and HfO_2 thin films 49

called a gate. In general, MOSFET works as a switch regulated by gate voltage. Increasing the gate voltage beyond a threshold voltage, V_{th} , generates the resistive channel for current flow between the drain and source terminals. The radiation-induced oxide charges lead to an alteration of the V_{th} value.

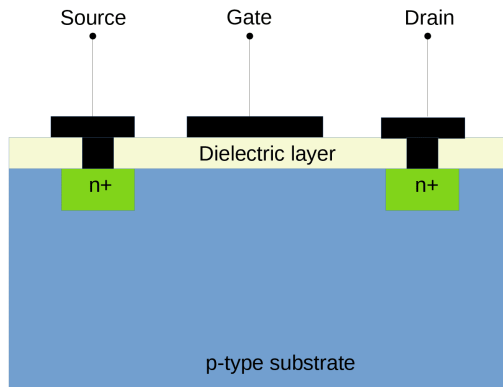


Figure 7.2: Schematic of a N-channel MOSFET.

The simulated structure reproduced the laboratory-measured transistors as closely as possible with a channel length of $250 \mu\text{m}$. The source and drain have heavily doped n+ implants with the doping concentration of $1 \cdot 10^{19} \text{cm}^{-3}$. The thickness of the alumina and hafnia layers were the same as in the MOS capacitor study. The radiation-induced oxide charges and interface traps are studied by determining the threshold voltage in transfer characteristics, which is defined as a change in the drain-to-source current (I_{ds}) with a change in a gate voltage (V_g) at a constant drain-to-source voltage (V_{ds}). The threshold voltage is the point of inflection beyond which I_{ds} increases exponentially with a gradual increase in V_g . The interface states were modeled with two single trap levels, similar to the ones in the MOS capacitor study. All of the parameters that were used for the surface damage model are listed in Tables 7.2 and 7.3.

Figure 7.3 shows the simulated I_{ds} curves for MOSFET with alumina and alumina/hafnia as gate insulators. The results are congruous to the measurements where the shift in the threshold voltage to higher bias values is observed and is attributed to the cumulative contribution of negative oxide and interface trapped charges. Both MOS capacitor and MOSFET simulations indicate that at high radiation doses of $5 \cdot 10^{14}$ protons/cm² the interface traps impact dominates the oxide charge effect.

For investigations of the electric field distribution, a larger 2D structure was created. The simulated sensor configurations were designed with parameters as close to the real sensors as possible. The sensor had a physical thickness of $320 \mu\text{m}$, a pitch of $150 \mu\text{m}$, and a pixel implant width of $100 \mu\text{m}$. The p-type bulk doping was set to $8 \cdot 10^{11} \text{cm}^{-3}$. The heavily doped phosphorus and boron implantations on the front and back planes had peak

Type of trap	Level (eV)	σ_e (cm ²)	σ_h (cm ²)	Fluence(protons/cm ²)	Density (cm ⁻²)
Donor	$E_v + 0.5$	$1 \cdot 10^{-16}$	$1 \cdot 10^{-15}$	0	0
Acceptor	$E_c - 0.3$	$1 \cdot 10^{-15}$	$1 \cdot 10^{-16}$	0	0
Donor	$E_v + 0.5$	$1 \cdot 10^{-16}$	$1 \cdot 10^{-15}$	$5 \cdot 10^{12}$	$2 \cdot 10^{12}$
Acceptor	$E_c - 0.3$	$1 \cdot 10^{-15}$	$1 \cdot 10^{-16}$	$5 \cdot 10^{12}$	$6 \cdot 10^{12}$
Donor	$E_v + 0.5$	$1 \cdot 10^{-16}$	$1 \cdot 10^{-15}$	$5 \cdot 10^{13}$	$3 \cdot 10^{12}$
Acceptor	$E_c - 0.3$	$1 \cdot 10^{-15}$	$1 \cdot 10^{-16}$	$5 \cdot 10^{13}$	$7 \cdot 10^{12}$
Donor	$E_v + 0.5$	$1 \cdot 10^{-16}$	$1 \cdot 10^{-15}$	$5 \cdot 10^{14}$	$3 \cdot 10^{12}$
Acceptor	$E_c - 0.3$	$1 \cdot 10^{-15}$	$1 \cdot 10^{-16}$	$5 \cdot 10^{14}$	$7 \cdot 10^{12}$

Fluence(protons/cm ²)	Oxide charge Density (cm ⁻²)
0	$-3 \cdot 10^{11}$
$5 \cdot 10^{12}$	$-7 \cdot 10^{12}$
$5 \cdot 10^{13}$	$-8 \cdot 10^{12}$
$5 \cdot 10^{14}$	$-1.5 \cdot 10^{13}$

Table 7.2: Details of surface damage model for MOSFET with alumina as a dielectric layer.

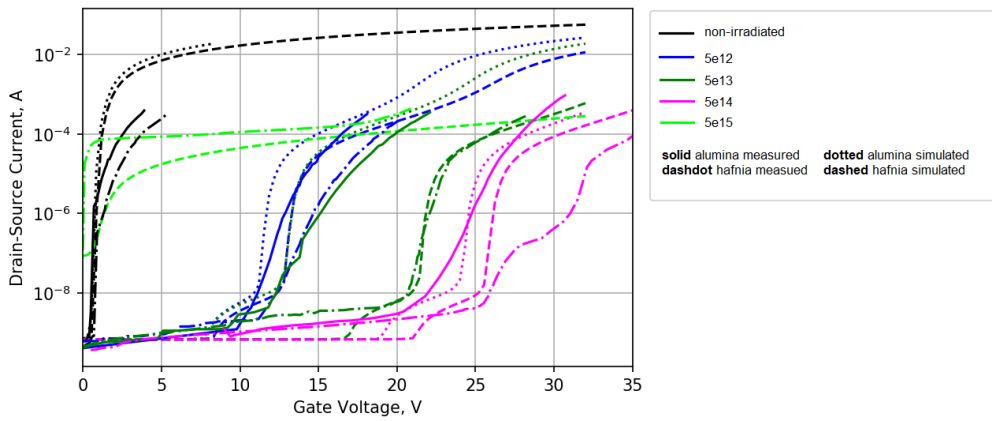


Figure 7.3: Simulated and measured CV curves of a non-irradiated and irradiated MOSFET with alumina and hafnia as a dielectric.

Type of trap	Level (eV)	σ_e (cm ²)	σ_h (cm ²)	Fluence(protons/cm ²)	Density (cm ⁻²)
Donor	$E_v + 0.5$	$1 \cdot 10^{-16}$	$1 \cdot 10^{-15}$	0	0
Acceptor	$E_c - 0.3$	$1 \cdot 10^{-15}$	$1 \cdot 10^{-16}$	0	0
Donor	$E_v + 0.5$	$1 \cdot 10^{-16}$	$1 \cdot 10^{-15}$	$5 \cdot 10^{12}$	$2 \cdot 10^{12}$
Acceptor	$E_c - 0.3$	$1 \cdot 10^{-15}$	$1 \cdot 10^{-16}$	$5 \cdot 10^{12}$	$6 \cdot 10^{12}$
Donor	$E_v + 0.5$	$1 \cdot 10^{-16}$	$1 \cdot 10^{-15}$	$5 \cdot 10^{13}$	$2 \cdot 10^{12}$
Acceptor	$E_c - 0.3$	$1 \cdot 10^{-15}$	$1 \cdot 10^{-16}$	$5 \cdot 10^{13}$	$6 \cdot 10^{12}$
Donor	$E_v + 0.5$	$1 \cdot 10^{-16}$	$1 \cdot 10^{-15}$	$5 \cdot 10^{14}$	$2 \cdot 10^{12}$
Acceptor	$E_c - 0.3$	$1 \cdot 10^{-15}$	$1 \cdot 10^{-16}$	$5 \cdot 10^{14}$	$6 \cdot 10^{12}$
Donor	$E_v + 0.5$	$1 \cdot 10^{-16}$	$1 \cdot 10^{-15}$	$5 \cdot 10^{15}$	$2.1 \cdot 10^{13}$
Acceptor	$E_c - 0.3$	$1 \cdot 10^{-15}$	$1 \cdot 10^{-16}$	$5 \cdot 10^{15}$	$1.5 \cdot 10^{13}$

Fluence(protons/cm ²)	Oxide charge Density (cm ⁻²)
0	$-3 \cdot 10^{11}$
$5 \cdot 10^{12}$	$-6 \cdot 10^{12}$
$5 \cdot 10^{13}$	$-1 \cdot 10^{13}$
$5 \cdot 10^{14}$	$-1.2 \cdot 10^{12}$
$5 \cdot 10^{15}$	$-3 \cdot 10^{11}$

Table 7.3: Details of surface damage model for MOSFET with alumina and hafnia as a dielectric layer.

Type of trap	Level (eV)	σ_e (cm ²)	σ_h (cm ²)	Concentration (cm ⁻³)
Donor	$E_v + 0.48$	$4 \cdot 10^{-14}$	$4 \cdot 10^{-14}$	$0.8 \cdot F$
Acceptor	$E_c - 0.525$	$4 \cdot 10^{-14}$	$4 \cdot 10^{-14}$	$0.8 \cdot F$

Table 7.4: Details of two-level bulk damage model. F is the fluence in $n_{eq} \cdot \text{cm}^{-2}$

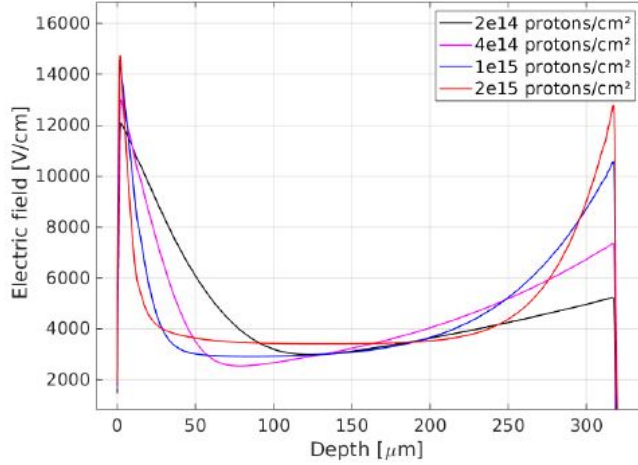


Figure 7.4: Simulated electric field distribution across the bulk of an irradiated p-type silicon detector at different fluences biased at 150 V (Publication IV).

concentrations of $1 \cdot 10^{15} \text{ cm}^{-3}$ and $5 \cdot 10^{15} \text{ cm}^{-3}$, respectively. Each pixel had a biasing electrode as well as AC-coupled charge collecting contacts. The reverse bias voltage was provided by the backplane contact.

In the simulation, the bulk damage is approximated by an effective two-defect model [73] with the parameters listed in Table 7.4. Surface damage is modeled in the simulation by placing a fixed charge Q_f at the oxide/Si interface and the interface traps that were assessed from the MOS capacitor simulation.

The simulated electric field profiles in Fig. 7.4 are compared to the measured drift velocity distributions based on edge-TCT measurements [74]. From the comparison one can see that both the simulated and the measured profiles exhibit a similar double-peak effect that gets more pronounced for heavily irradiated samples above $2 \cdot 10^{14} \text{ protons/cm}^2$.

The characterization of MOS and MOSFET devices indicated a negative charge accumulation induced by proton irradiation. The study shows that MOS devices with Al_2O_3 and HfO_2 are more sensitive to irradiation in comparison to samples with Al_2O_3 alone as the oxide layer. At higher fluences, above $5 \cdot 10^{14} \text{ protons/cm}^2$, the interface traps impact dominates over the oxide charge effect, and the increase in the concentration of interface traps leads to the negative shift in threshold and a subsequent increase in the leakage current. From TCT measurements, the double junction effect, as a consequence of deep-level traps in the bandgap of silicon, was identified in proton-irradiated AC-pixel sensors. That was confirmed with the corresponding simulations using the two-defect model for proton irradiation.

7.2 Simulation study of CVD diamond sensors

The initial motivation for this research was to explore and understand the single crystal CVD (scCVD) diamond bulk internal properties and polarization mechanism better with numerical simulations using Synopsys Sentaurus TCAD software (Publication I).

The detector design was kept very simple for this study. The simulated pad diode structure had dimensions of $100 \times 300 \times 1 \mu\text{m}^3$, where $300 \mu\text{m}$ corresponded to the device thickness, while width and length were scaled with an area factor of A to the match dimensions of the real devices. In the simulation, Schottky-type contacts were considered with a low barrier height of 0.8 eV .

Diamond material is not included in the material libraries of TCAD simulation tools, but TCAD allows the introduction of user-defined materials or the modification of existing materials' entries. Therefore, a scCVD diamond material entry was created where all the physical parameters of the scCVD diamond, such as permittivity, optical refractive index, and band gap, were defined by hand using data from Refs. [75, 76]. The bandgap energy was 5.47 eV with electron affinity 1.73 eV for the oxygen-terminated diamond surfaces.

The intrinsic carrier concentration in the diamond bulk was considered equal to $n_i = 10^{-27} \text{ cm}^{-3}$. However, there are also technology-related impurities present. Nitrogen and boron are known donor and acceptor species that incorporate in diamond during the CVD growth process. In order to take into account the effect of these impurities, two impurity levels, each with a concentration of 10^{12} cm^{-3} , were introduced into the diamond bandgap. A nitrogen-based acceptor energy level was located at $E_v + 0.368 \text{ eV}$, and donor-type energy levels originating from boron impurities had an energy of $E_c - 1.7 \text{ eV}$. The impurities' electron $\sigma_e = 1 \cdot 10^{-14} \text{ cm}^2$ and hole $\sigma_h = 1 \cdot 10^{-13} \text{ cm}^2$ capture cross-sections were found by fitting simulated transients to the measurement results. The obtained cross-section for electrons in boron is in good agreement with the experimentally measured value [77], but nitrogen shows a larger cross-section than is found experimentally [77].

Laboratory transient currents measured with an α -particle source at various bias voltages were used as references for the simulated TCT signals. In the TCT measurements, α -particles deposit the charge close to the surface of entry, which enables the probing of only one type of charge carriers. One type of the charge carrier is immediately collected by the nearest electrode, while the other one drifts through the whole detector thickness to the other electrode. Using the Shockley-Ramo theorem [27], the electric field inside the sensor can be deduced.

Single crystal diamonds, which were used as a reference for the simulation current transients, were irradiated at the CERN IRRAD facility with 24 GeV/c protons to a target fluence of 10^{14} p/cm^2 . Radiation damage to the scCVD diamond is currently explained by the introduction of neutral vacancy defects that affect both holes and electrons collec-

tion [78]. Thus, a neutral level with the energy of $E_v + 2.85$ eV corresponding to a neutral mono-vacancy [79] was introduced in the simulation model. The alpha particle interaction was simulated using the TCAD built-in heavy ion model with $12 \mu\text{m}$ radiation length.

Polarization phenomena due to charge trapping is observed in irradiated diamond materials as the deterioration of the CCE of the detector. It occurs as a build-up of charge occurs inside the detector's bulk, which eventually reduces charge collection efficiency. It can be countered by either filling all traps, e.g., by irradiating with a beta-source or with UV light, or periodically releasing trapped charge e.g. by periodically switching the bias voltage on and off.

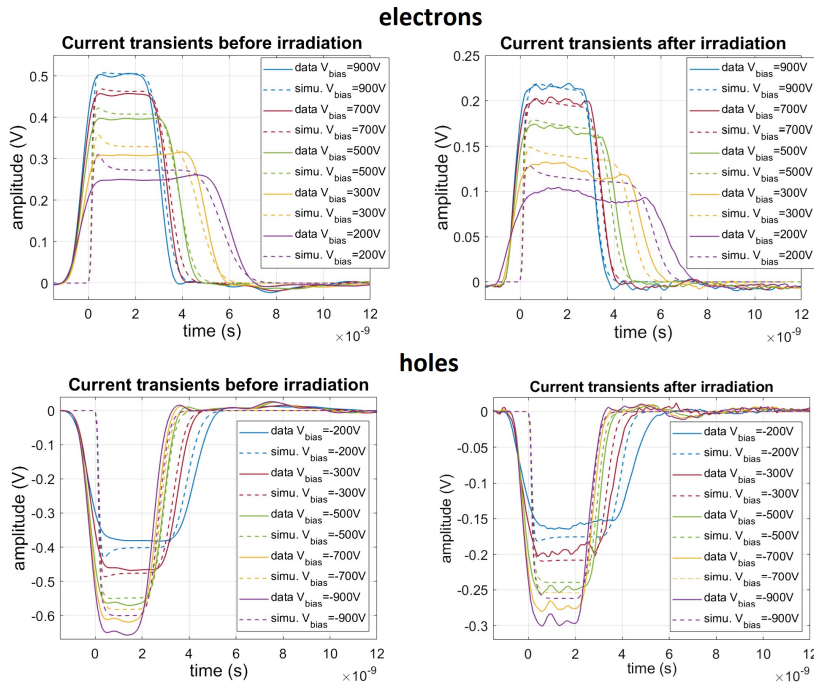


Figure 7.5: Simulated TCT transients of non-irradiated (left) and irradiated (right) diamond detectors for electron (upper) and hole (lower) drifts at various bias voltages (Publication I).

The mobility of charge carriers and their drift velocities were determined from experimental TCT signals measured while the diamond bulk was in a non-polarized state. Drift velocity for different bias voltages can be calculated as the distance passed by a charge divided by the average time of traveling. In terms of a detector, distance is the thickness of the detector, d , and time is the full width at half maximum (FWHM) of the TCT pulse at a certain bias voltage. On the other hand, mobilities can be found from the Caughey and Thomas empirical formula for drift velocity [80]. The found electron mobility values for non-irradiated and irradiated detectors were quite noisy, but considering calculations

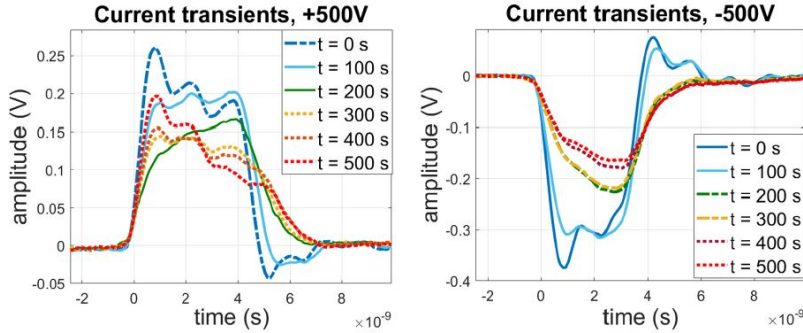


Figure 7.6: Transient current for electrons at different times after turning bias voltage on for the diamond detector that has been irradiated to $10^{14} p/cm^2$ (Publication I) .

$\mu_e = 4500 \text{ cm}^2/V\cdot\text{s}$ and $\mu_e = 1000 \text{ cm}^2/V\cdot\text{s}$ for non-irradiated and irradiated diamonds, respectively, seem reasonable [40]. The hole mobilities of non-irradiated and irradiated diamond detectors were $2000 \text{ cm}^2/V\cdot\text{s}$ and $1520 \text{ cm}^2/V\cdot\text{s}$, correspondingly.

The CVD diamond model was developed reproducing the laboratory measurements for non-irradiated and irradiated detectors to the fluence of $10^{14} p/cm^2$, which can be seen in Fig. 7.5. The laboratory measurements' transients were recorded within 10 s after turning on the bias voltage. Electron and hole signal before irradiation show the expected rectangular shape, indicating a constant electric field. A polarization effect, where charge collection efficiency drops suddenly, is observed for all diamond detectors after irradiation with protons and is absent in the same detectors before the irradiation. In Fig. 7.6 the time evolution of current transient is shown. For the low fluence ($10^{14} p/cm^2$) detectors, turning bias voltage off periodically for 1 min and back on is an effective method for removing polarization. For high fluence ($5 \cdot 10^{14} p/cm^2$) detectors, switching high voltage off and back on is not sufficient for restoring charge collection efficiency. Alternate methods for improving detector performance, such as filling traps or reprocessing, are recommended for consideration in the high particle rate environment. However, the polarization effect, that was observed during the measurements, needs to be studied more in order to achieve good predictive capabilities of the numerical model.

7.3 Simulation study of CdTe detectors

This work was motivated by the need to study the effects of defects in CdTe pad detectors with the red laser TCT and the effect of the surface passivation on the signal (Publications II and III).

The CdTe pad detectors discussed in this section represent a simple structure of CdTe single crystals with metal electrodes on the front side (with an optical window) and a back side. The simulated diode structure reproduced the sample as closely as possible and had

dimensions of $A \times 3000 \times 1000 \mu\text{m}^3$ with a 50 nm-thick aluminum nitride (AlN) passivation layer, where A is an area factor to match the dimensions of the real diode. The thicknesses of the Au contacts on the front and back planes were 500 nm. The Schottky-type contacts with a work function of 5 eV were considered. In the simulation, a CdTe bulk with a uniform charge carrier concentration of $1 \cdot 10^7 \text{ cm}^{-3}$ was assumed [81]. A full depletion bias voltage of -450 V from the backplane was utilized in the simulations. There is a circular opening with a diameter of 2 mm without metallization on one side of the detector for TCT measurements. In order to consider a highly defected bulk of the CdTe body, two mid-gap levels (a deep acceptor and a donor level) were implemented with energies 0.72 eV and concentration $1 \cdot 10^{12} \text{ cm}^{-3}$ [82]. The electron and hole capture cross-sections were found by fitting simulated transients to the measurement results.

In the red laser TCT, electron-hole pairs are generated close to the surface of the illuminated side of the device. One type of the charge carriers is immediately collected by the nearest electrode. Thus, the induced current is an outcome of a single carrier type drift, depending on the bias voltage sign. The collected signal is rich in information about the detector. Various parameters, such as rise time, charge collection efficiency, and peaking amplitude can be extracted from the signal. By mounting the setup on a XYZ-stage and combining the signal output with the position information from the stages, the locations of defects and other non-uniformities can be mapped, and their effect on the charge collection efficiency can be studied [83]. In the simulation, the laser beam was pointed at three different positions at the surface—the center of the opening, the left and right edges of the opening—in order to consider electric field variation near the interface.

In simulations, large-scale defects (grain boundaries, crystal non-uniformities) in the detector bulk were reproduced by introducing an inclusion with high amount of traps into the detector body to the CdTe semiconductor material, as depicted in Fig. 7.7. The conventional method of introducing energy levels into the CdTe bulk bandgap does not have a local impact of such a defect inclusion. A circular-shaped inclusion with a diameter of $10 \mu\text{m}$ imitated a local defect. For the trap levels in the inclusion material, the same two mid-gap levels (a deep acceptor and a donor level) were implemented with energies of 0.72 eV, with the same concentration for acceptor and donor traps as in the bulk.

Different test structure simulations have been performed in order to systematically study the impact of different variations of the structure on the TCT results. Bulk defects, defect inclusion, and passivation on top of the optical opening were the main alternations in the simulation model.

First, a comparison of the transverse distribution of the electrical field at the position of the defect for the simulated diode with and without defect incorporation and no bulk traps and no surface passivation was conducted. The simulations show the effect of local defect on the electric field distribution and transient current, which is illustrated in Fig. 7.8a. It can be seen from Fig. 7.8b that the transient response of the diode with the local defect rapidly decreases after the narrow peak produced by collected electrons. The hole current

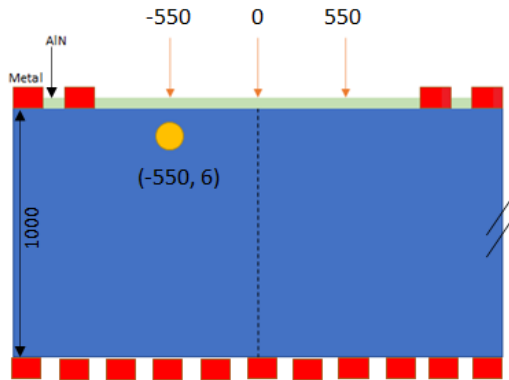


Figure 7.7: A schematic of the simulated structure with the optical opening and a defect inclusion. All the dimensions are in μm . The optical opening is from $-1000 \mu\text{m}$ to $1000 \mu\text{m}$ and the defect inclusion center position is $(-550, 6)$. The laser beam was pointed at three different positions on the surface: the middle of the opening (0), and the left and right edges of the opening (-550 and 550) (Publication III).

in this case is by two orders of magnitude less than the signal without inclusion. As the creation point of $e-h$ pairs is very close to the defect area with lots of traps, part of the charge carriers are captured by the trap levels in the inclusion.

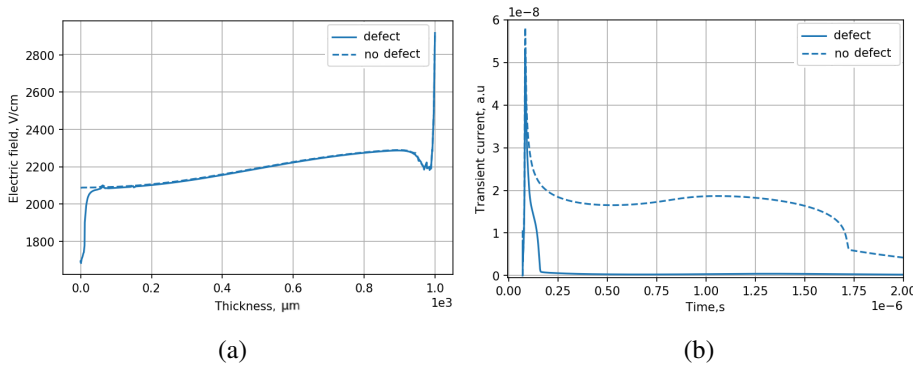


Figure 7.8: a) Comparison of the transverse distribution of the electrical field at the position of the defect for the simulated diode with and without defect incorporation. No bulk traps and no surface passivation were considered. b) Comparison of the transient current at the position of the defect for the simulated diode with and without defect incorporation. No bulk traps and no surface passivation were considered (Publication III).

Additionally, the effect of passivation on the electric field distribution has been studied. Comparing the structure with and without passivation on top of the optical opening shows the difference in electric field distribution.

In Fig. 7.9 one can see that the electric field strength is almost two times higher for the

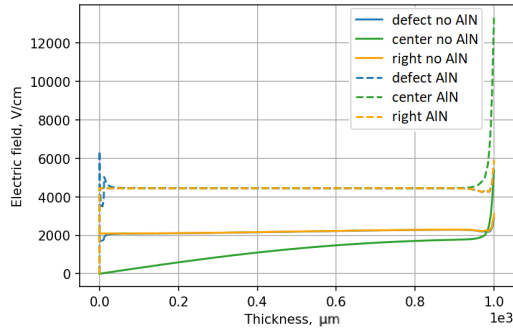


Figure 7.9: Simulated transverse distribution of the electrical field for the diode with the defect inclusion, no bulk traps, and with and without passivation on top of the optical opening (Publication III).

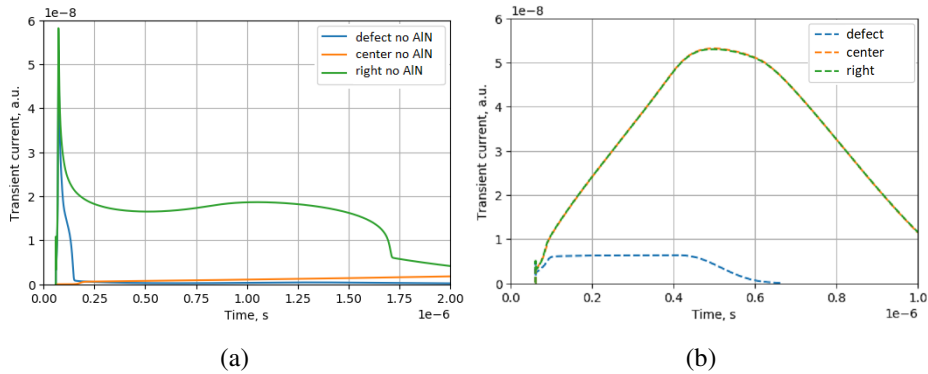


Figure 7.10: a) Simulated transient current for the simulated diode with the defect inclusion, no surface passivation, and no bulk traps. b) Simulated transient current for the simulated diode with the defect inclusion, surface passivation, and no bulk traps (Publication III).

detector with dielectric on top of the optical opening. In the simulation a positive fixed oxide charge was used with the absolute value of Q_f equal to $1 \cdot 10^{12} \text{ cm}^{-2}$. With the AlN layer on top of the optical opening the potential difference increases and the strength of the electric field changes to a higher value. The corresponding waveforms for the CdTe diode with and without AlN on top of the optical opening are shown in Fig. 7.10a. A smaller electric field in a non-passivated detector results in a longer signal duration, a lot more than $1 \mu\text{s}$. At the center of the opening without AlN film, the electric field near the surface is zero, so the charge carrier drift velocity decreases in the low potential region and the signal evolves very slowly. Only the beginning of the signal with very low amplitude can be observed. On the right side of the opening the current reproduces the signal with no defect depicted in Fig. 7.10b. The electric field strength at the center of the optical opening with the dielectric on top is almost the same as for the right side of the device, therefore, the transient currents are also identical. By comparing two transient signals at the position of the defect inclusion with and without the passivation layer, one can notice that the resulting current duration is of 600 ns with the AlN deposited, while for the case without dielectric on the optical opening the signal is longer than 1000 ns. The narrow peak at the beginning of the signal disappears in the presence of the positive fixed charge from the passivation layer, as the increased electric field strength raises the electron drift velocity, and the electrons are immediately collected by the nearby contact. It should be pointed out that the shape of the signal with the defect inclusion and AlN on top of the opening has a characteristic form at a defect position, which can be easily identified from the surroundings.

Figure 7.11 presents the distribution of a simulated transverse field for different oxide charge values as well as corresponding transient currents. It can be noted that with the higher value of the interface oxide charge the electric field strength has a higher value. For the corresponding current signals the higher value of the interface oxide charge gives a lower value of the amplitude of the signal. In Publication II, the simulation for a structure with Al_2O_3 was performed and compared with the laboratory measurements. The surface passivation, especially the fixed oxide charge value, plays an important role in the electric field formation and should be taken into account when designing a detector.

Finally, the bulk trap levels were implemented so as to take into account the highly defected CdTe bulk material. Our results systematically indicate longer pulse durations, i.e., higher CCE and longer charge carrier lifetime in Al_2O_3 -passivated detectors than in those passivated by the AlN (Publication II). This is likely due to the negative oxide charge in ALD-grown Al_2O_3 thin films. A model of local bulk defect shows that the presence of the local defect leads to a reduction in charge collection efficiency. The transient current signals possess different shapes depending on the laser beam position and the size of a defect inclusion. From the simulations it is seen that inclusions that are closer to the surface and with larger diameter, assuming constant trap level energies, trap concentration, and electron and hole capture-cross sections, have a greater impact on the waveforms using the red laser. Also the shifted laser beam position from the center of the defect results in the fluctuations of the signal form. These simulations confirm that defects can be clearly dis-

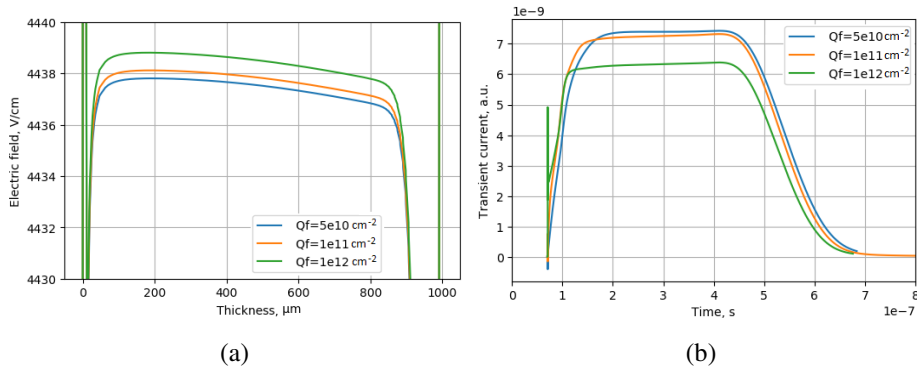


Figure 7.11: a) Simulated transverse electric field distribution and b) corresponding transient current at the position of the defect inclusion with AlN on top of the optical opening for different oxide charges Q_f (Publication III).

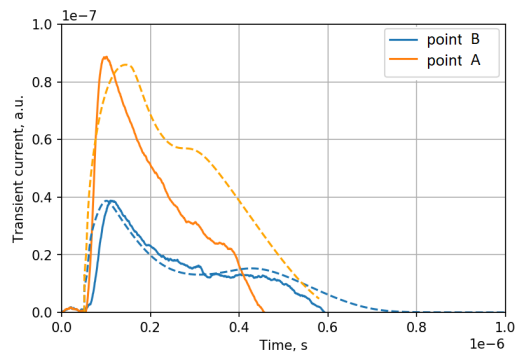


Figure 7.12: Simulated (dashed) and measured (solid) transient currents of the CdTe detector (Publication III).

tinguished from the surroundings using transient current technique due to a characteristic shape of the TCT signal in a defect position. We were able to reproduce the measurement results adequately with a simple simulation model with one defect inclusion, as can be noticed in Fig. 7.12.

8 Conclusion

Nowadays, numerical simulations have become a widely used tool for the mathematical modeling of many natural systems as well as human systems. The ability to predict the behavior of the system, whether it is an electronic device or the dynamics of the economy, is of major interest as it eases experiments significantly.

The purpose of the work was to use TCAD simulations to investigate the impact of defects on the device performance. In particular, three different radiation sensors have been studied: CdTe diodes, chemical vapor deposited (CVD) diamond detectors, and Si detectors with aluminium oxide thin film.

For the CVD diamond diode, the model reproducing the measurement results has been developed for non-irradiated and irradiated samples up to the fluence of 10^{14} p/cm² samples. A polarization effect, where charge collection efficiency drops suddenly, is observed for all diamond detectors after irradiation with protons, which is not seen with those detectors before the irradiation treatment. For the low fluence (10^{14} p/cm²) detectors, turning bias voltage off periodically for 1 min and back on is an effective way of removing polarization. For the high fluence ($5 \cdot 10^{14}$ p/cm²) detectors, switching high voltage off and back on is not sufficient for restoring charge collection efficiency. It is advised to consider alternate methods for improving detector performance, such as filling traps or reprocessing in high particle rate environment. However, in order to study the polarization phenomenon more measurements and simulation studies are needed.

A simulation study of irradiated Si MOS capacitors and MOSFET with aluminium oxide and hafnium oxide as an insulator layer has been performed and surface damage is modeled up to $5 \cdot 10^{15}$ p/cm². Characterization of MOS and MOSFET devices indicated a negative charge accumulation induced by proton irradiation. The study shows that MOS devices with Al₂O₃ and HfO₂ are more sensitive to irradiation in comparison to samples with Al₂O₃ alone at the oxide layer. At higher fluences, above $5 \cdot 10^{14}$ protons/cm², the impact of interface traps dominates over the oxide charge effect, and increases in the concentration of interface traps leads to a negative shift in threshold voltage and a subsequent increase in the leakage current. The values of the fixed oxide charge and interface traps that were assessed from the MOS capacitor simulations were combined with the bulk two-defect model in order to achieve a model that considers bulk damage and surface damage for a detector with Al₂O₃. The double-junction effect was observed in proton-irradiated AC-pixel sensors, due to the radiation-induced deep level traps in the bandgap of silicon. In order to construct a model with better predictive power more statistics is needed.

A simulation model of a CdTe diode with a defect incorporation was implemented. The impact of the defect on the electric field distribution as well as the effect of the surface passivation have been studied. The reproduction of the measurement results has been achieved with a developed simple model with one defect. The model shows that structures with the inclusion closer to the surface and with larger diameter have higher impact

on the red laser transient current signals. Another finding is that the surface passivation, especially the value of the fixed oxide charge, plays an important role in electric field formation and should be taken into account while designing the detector.

More measurement data is needed for all of the detector types in order to expand the statistical data. One of the objectives is to stretch the simulation defect models for higher fluences, in case of sensors with alumina thin films. Irradiation of the same sensors with different types of radiation could be an advantage. Low frequency laboratory CV measurements of MOS structures could help with the precise definition of the interface trap energy level and concentration and therefore create a more reliable model.

A combination of different types of characterization techniques, such as infrared microscopy, transient current technique, and scanning electron microscopy with TCAD simulations would help to identify the impact of the different kind of patterns of higher local defect densities on the device performance in the case of CdTe. Material science research is of ultimate interest for CdTe devices with alumina thin films. CV characterization of the CdTe MOS capacitor structures with alumina thin films would provide us with important information on the fixed oxide charge concentration for various processing parameters. Combining CV laboratory measurements with the quality assessment of the surface could help to identify the effect of defects close to the surface on the fixed oxide charge and interface traps formation. TCAD supports all of the measurements and helps in the understanding of dependencies.

Numerical simulation is a link between semiconductor physics and the electrical performance of the device. The results presented in this work encourage further usage of TCAD for the investigation of the defect impact on the device performance to gain predictive power.

References

- [1] P.W. Higgs. Broken symmetries, massless particles and gauge fields. *Physics Letters*, 12(2):132–133, 1964.
- [2] ATLAS Collaboration. Observation of a new particle in the search for the Standard Model Higgs boson with the ATLAS detector at the LHC. *Physics Letters B*, 716(1):1–29, 2012.
- [3] CMS Collaboration. Observation of a new boson at a mass of 125 GeV with the cms experiment at the LHC. *Physics Letters B*, 716(1):30–61, 2012.
- [4] B. Abelev et al. Technical design report for the upgrade of the ALICE inner tracking system. *Journal of Physics G: Nuclear and Particle Physics*, 41(8):087002, jul 2014.
- [5] ATLAS Collaboration. Technical design report: A high-granularity timing detector for the atlas phase-ii upgrade. Technical report, CERN, Geneva, Jun 2020.
- [6] CMS Collaboration. The phase-2 upgrade of the cms tracker. Technical report, CERN, Geneva, Jun 2017.
- [7] LHCb Collaboration. Lhcb tracker upgrade technical design report. Technical report, Feb 2014.
- [8] S. Orfanelli. The phase 2 upgrade of the CMS inner tracker. *Nuclear Instruments and Methods in Physics Research Section A: Accelerators, Spectrometers, Detectors and Associated Equipment*, 980:164396, 2020.
- [9] G. Lindström. Radiation damage in silicon detectors. *Nuclear Instruments and Methods in Physics Research Section A: Accelerators, Spectrometers, Detectors and Associated Equipment*, 512(1):30–43, 2003. Proceedings of the 9th European Symposium on Semiconductor Detectors: New Developments on Radiation Detectors.
- [10] Stuart K. Tewksbury. *Fabrication Defects*, pages 75–114. Springer US, Boston, MA, 1989.
- [11] G. Pellegrini, C. Fleta, F. Campabadal, M. Minano, M. Lozano, J.M. Rafi, and M. Ullan. Technology of p-type microstrip detectors with radiation hard p-spray, p-stop and moderated p-spray insulations. *Nuclear Instruments and Methods in Physics Research Section A: Accelerators, Spectrometers, Detectors and Associated Equipment*, 579(2):599–603, 2007. Proceedings of the 6th "Hiroshima" Symposium on the Development and Application of Semiconductor Detectors.
- [12] J. Härkönen, E. Tuovinen, P. Luukka, A. Gädda, T. Mäenpää, E. Tuominen, T. Arsenovich, A. Junkes, X. Wu, and Z. Li. Processing of n+/p-/p+ strip detectors with atomic layer deposition (ALD) grown Al_2O_3 field insulator on magnetic czochralski silicon (MCz-si) substrates. *Nuclear Instruments and Methods in Physics Research Section A: Accelerators, Spectrometers, Detectors and Associated Equipment*, 828:46–51, 2016.

- [13] J. Härkönen, J. Ott, M. Mäkelä, T. Arsenovich, A. Gädda, T. Peltola, E. Tuovinen, P. Luukka, E. Tuominen, A. Junkes, J. Niinistö, and M. Ritala. Atomic layer deposition (ALD) grown thin films for ultra-fine pitch pixel detectors. *Nuclear Instruments and Methods in Physics Research Section A: Accelerators, Spectrometers, Detectors and Associated Equipment*, 831:2–6, 2016. Proceedings of the 10th International Hiroshima Symposium on the Development and Application of Semiconductor Tracking Detectors.
- [14] S. Del Sordo, L. Abbene, E. Caroli, A. Mancini, A. Zappettini, and P. Ubertini. Progress in the development of CdTe and CdZnTe semiconductor radiation detectors for astrophysical and medical applications. *Sensors*, 9(5):3491–3526, 2009.
- [15] A. Winkler, T. Naaranoja, A. Gädda, J. Ott, P. Luukka, A. Karadzhinova-Ferrer, M. Kalliokoski, and J. Härkönen. Optical and electrical characterization of cadmium telluride x-ray pad detectors. *Nuclear Instruments and Methods in Physics Research Section A: Accelerators, Spectrometers, Detectors and Associated Equipment*, 924:28–32, 2019. 11th International Hiroshima Symposium on Development and Application of Semiconductor Tracking Detectors.
- [16] G. A. Armstrong and C. K. Maiti. *TCAD for Si, SiGe and GaAs Integrated Circuits*. Inspec/Iee, 2008.
- [17] S.M. Sze. *Semiconductor Devices: Physics and Technology*. John Wiley & Sons Singapore Pte. Limited, 2006.
- [18] S.M. Sze. *Semiconductor Devices: Physics and Technology*. John Wiley & Sons Singapore Pte. Limited, 1981.
- [19] D. K. Schroder. *Semiconductor Material and Device Characterization*. Wiley-Interscience, USA, 2006.
- [20] E. H. Nicollian and John R. Brews. *MOS (Metal Oxide Semiconductor) Physics and Technology*. Wiley-Interscience, USA, 1982.
- [21] F. Braun. On the Current Transport in Metal Sulfides (in German). *Annal. Phys. Chem*, 153:556–563, 1874.
- [22] G. Knoll. *Radiation detection and measurement*. John Wiley, Hoboken, N.J, 4th edition, 2010.
- [23] G. Was. *Fundamentals of Radiation Materials Science*. Springer, 2007.
- [24] F. Sauli. *Interaction of photons and neutrons with matter*, pages 43–75. Cambridge Monographs on Particle Physics, Nuclear Physics and Cosmology. Cambridge University Press, 2014.
- [25] K. J. Wetzel. Recoil broadening of secondary transitions in neutron-capture gamma-ray cascades. *Phys. Rev.*, 181:1465–1476, May 1969.

- [26] S. Raman, E. T. Journey, J. W. Starner, A. Kuronen, J. Keinonen, K. Nordlund, and D. J. Millener. Lifetimes in ^{15}N from gamma-ray line shapes produced in the $^2\text{H}(^{14}\text{n,p}\gamma)$ and $^{14}\text{N}(\text{thermal n},\gamma)$ reactions. *Phys. Rev. C*, 50:682–697, Aug 1994.
- [27] S. Ramo. Currents induced by electron motion. *Proc. Ire.*, 27:584–585, 1939.
- [28] W. Shockley. Currents to conductors induced by a moving point charge. *Journal of Applied Physics*, 9(10):635–636, 1938.
- [29] R.C. Alig and S. Bloom. Electron-hole pair creation energies in semiconductors. *Physical Review Letters*, 35(22):1522–1525, December 1975.
- [30] T. Suntola. Atomic layer epitaxy. *Thin Solid Films*, 216(1):84–89, 1992. Papers presented at the International Workshop on Science and Technology of Thin Films for the 21st Century, Evanston,IL, USA, July 28-August 2, 1991.
- [31] M. Leskelä and M. Ritala. Atomic layer deposition (ALD): from precursors to thin film structures. *Thin Solid Films*, 409(1):138–146, 2002. Proceedings of the 2nd Asian Conference on Chemical Vapour Deposition.
- [32] J. Ott, A. Gädda, S. Bharthuar, E. Brücken, M. Golovleva, J. Härkönen, M. Kalliokoski, A. Karadzhinova-Ferrer, S. Kirschenmann, V. Litichevskyi, P. Luukka, L. Martikainen, and T. Naaranoja. Processing of AC-coupled n-in-p pixel detectors on MCz silicon using atomic layer deposited aluminium oxide. *Nuclear Instruments and Methods in Physics Research Section A: Accelerators, Spectrometers, Detectors and Associated Equipment*, 958:162547, 2020. Proceedings of the Vienna Conference on Instrumentation 2019.
- [33] A. Gädda, J. Ott, S. Bharthuar, E. Brücken, M. Kalliokoski, A. Karadzhinova-Ferrer, M. Bezak, S. Kirschenmann, V. Litichevsky, M. Golovleva, L. Martikainen, A. Winkler, V. Chmill, E. Tuovinen, P. Luukka, and J. Härkönen. AC-coupled n-in-p pixel detectors on MCz silicon with atomic layer deposition (ALD) grown thin film. *Nuclear Instruments and Methods in Physics Research Section A: Accelerators, Spectrometers, Detectors and Associated Equipment*, 986:164714, 2021.
- [34] J. Ott, S. Bharthuar, A. Gädda, T. Arsenovich, M. Bezak, E. Brücken, M. Golovleva, J. Härkönen, M. Kalliokoski, A. Karadzhinova-Ferrer, S. Kirschenmann, V. Litichevskyi, P. Luukka, L. Martikainen, and T. Naaranoja. Characterization of magnetic czochralski silicon devices with aluminium oxide field insulator: effect of oxygen precursor on electrical properties and radiation hardness. *Journal of Instrumentation*, 16(05):P05011, may 2021.
- [35] J. Härkönen, J. Ott, A. Gädda, M. Bezak, E. Brücken, E. Tuovinen, S. Bharthuar, P. Luukka, and E. Tuominen. Processing and interconnections of finely segmented semiconductor pixel detectors for applications in particle physics and photon detection. *Frontiers in Physics*, 9:32, 2021.

- [36] C. E. Nebel. Electronic properties of CVD diamond. *Semiconductor Science and Technology*, 18(3):S1–S11, feb 2003.
- [37] S.E. Coe and R.S. Sussmann. Optical, thermal and mechanical properties of CVD diamond. *Diamond and Related Materials*, 9(9):1726–1729, 2000.
- [38] A. Owens and A. Peacock. Compound semiconductor radiation detectors. *Nuclear Instruments and Methods in Physics Research Section A: Accelerators, Spectrometers, Detectors and Associated Equipment*, 531(1):18–37, 2004. Proceedings of the 5th International Workshop on Radiation Imaging Detectors.
- [39] C. Bauer, I. Baumann, C. Colledani, J. Conway, P. Delpierre, F. Djama, W. Dulinski, A. Fallou, K.K. Gan, R.S. Gilmore, E. Grigoriev, G. Hallewell, S. Han, T. Hessian, K. Honscheid, J. Hrubec, D. Husson, R. James, H. Kagan, D. Kania, R. Kass, K.T. Knäpfle, M. Krammer, T.J. Llewellyn, P.F. Manfredi, D. Meier, L.S. Pan, H. Pernegger, M. Pernicka, V. Re, S. Roe, D. Roff, A. Rudge, M. Schaeffer, M. Schieber, S. Schnetzer, S. Somalwar, V. Speziali, R. Stone, R.J. Tapper, R. Tesarek, W. Trischuk, R. Turchetta, G.B. Thomson, R. Wagner, P. Weilhammer, C. White, H.J. Zioc, and M. Zoeller. Recent results from the RD42 diamond detector collaboration. *Nuclear Instruments and Methods in Physics Research Section A: Accelerators, Spectrometers, Detectors and Associated Equipment*, 383(1):64–74, 1996. Development and Application of Semiconductor Tracking Detectors.
- [40] J. Isberg, J. Hammersberg, E. Johansson, T. Wikström, D. J. Twitchen, A. J. Whitehead, S. E. Coe, and G. A. Scarsbrook. High carrier mobility in single-crystal plasma-deposited diamond. *Science*, 297(5587):1670–1672, 2002.
- [41] V. Cindro, D. Dobos, I. Dolenc, H. Frais-Kölbl, A. Gorišek, E. Griesmayer, H. Kagan, G. Kramberger, B. Macek, I. Mandić, M. Mikuž, M. Niegl, H. Pernegger, D. Tardif, W. Trischuk, P. Weilhammer, and M. Zavrtanik. The ATLAS beam conditions monitor. *Journal of Instrumentation*, 3(02):P02004–P02004, feb 2008.
- [42] M. Červ. The ATLAS diamond beam monitor. *Journal of Instrumentation*, 9(02):C02026–C02026, feb 2014.
- [43] W. Trischuk, M. Artuso, F. Bachmair, L. Bäni, M. Bartosik, V. Bellini, V. Belyaev, B. Bentele, E. Berdermann, P. Bergonzo, A. Bes, J.-M. Brom, M. Bruzzi, M. Cerv, C. Chau, G. Chiodini, D. Chren, V. Cindro, G. Claus, J. Collot, S. Costa, J. Cumalat, A. Dabrowski, R. D’Alessandro, W. de Boer, B. Dehning, D. Dobos, W. Dulinski, V. Eremin, R. Eusebi, G. Forcolin, J. Forneris, H. Frais-Kölbl, K.K. Gan, M. Gastal, M. Goffe, J. Goldstein, A. Golubev, L. Gonella, A. Gorišek, L. Graber, E. Grigoriev, J. Grosse-Knetter, M. Guthoff, I. Haughton, D. Hidas, D. Hits, M. Hoferkamp, T. Hofmann, J. Hosslet, J.-Y. Hostachy, F. Hüging, H. Jansen, J. Janssen, H. Kagan, K. Kanxheri, G. Kasieczka, R. Kass, F. Kassel, M. Kis, G. Kramberger, S. Kuleshov, A. Lacoste, S. Lagomarsino, A. Lo Giudice, C. Maa-zouzi, I. Mandic, C. Manfredotti, C. Mathieu, N. McFadden, G. McGoldrick,

- M. Menichelli, M. Mikuz, A. Morozzi, J. Moss, R. Mountain, S. Murphy, A. Oh, P. Olivero, G. Parrini, D. Passeri, M. Pauluzzi, H. Pernegger, R. Perrino, F. Piccolo, M. Pomorski, R. Potenza, A. Quadt, A. Re, G. Riley, S. Roe, M. Sapinski, M. Scaringella, S. Schnetzer, T. Schreiner, S. Sciortino, A. Scorzoni, S. Seidel, L. Servoli, A. Sfyrla, G. Shimchuk, S. Smith, B. Sopko, V. Sopko, S. Spagnolo, S. Spanier, K. Stenson, R. Stone, C. Suter, A. Taylor, M. Traeger, D. Tromson, W. Trischuk, C. Tuve, L. Uplegger, J. Velthuis, N. Venturi, E. Vittone, S. Wagner, R. Wallny, J.C. Wang, P. Weilhammer, J. Weingarten, C. Weiss, T. Wengler, N. Wermes, M. Yamouni, and M. Zavrtanik. Diamond particle detectors for high energy physics. *Nuclear and Particle Physics Proceedings*, 273-275:1023 – 1028, 2016. 37th International Conference on High Energy Physics (ICHEP).
- [44] G. Antchev, P. Aspell, I. Atanassov, V. Avati, J. Baechler, V. Berardi, M. Berretti, E. Bossini, U. Bottigli, M. Bozzo, P. BroulÅm, A. Buzzo, F.S. Cafagna, M.G. Catanesi, M. Csanad, T. Csörge, M. Deile, F. De Leonardis, A. D’Orazio, M. Doubek, K. Eggert, V. Eremin, F. Ferro, A. Fiergolski, F. Garcia, V. Georgiev, S. Giani, L. Grzanka, C. Guaragnella, J. Hammerbauer, J. Heino, A. Karev, J. Kaspar, J. Kopal, V. Kundra, S. Lami, G. Latino, R. Lauhakangas, R. Linhart, M.V. Lokajicek, L. Losurdo, M. Lo Vetere, F. Lucas Rodriguez, D. Lucsanyi, M. Macri, A. Mercadante, N. Minafra, S. Minutoli, T. Naaranoja, F. Nemes, H. Niewiadomski, T. Novak, E. Oliveri, F. Oljemark, M. Oriunno, K. Österberg, P. Palazzi, L. Palocko, V. Passaro, Z. Peroutka, V. Petruzzelli, T. Politi, J. Prochazka, F. Pruden-zano, M. Quinto, E. Radermacher, E. Radicioni, F. Ravotti, E. Robutti, C. Royon, G. Ruggiero, H. Saarikko, A. Scribano, J. Smajek, W. Snoeys, J. Sziklai, C. Taylor, N. Turini, V. Vacek, J. Welti, P. Wyzkowski, and K. Zielinski. Diamond detectors for the TOTEM timing upgrade. *Journal of Instrumentation*, 12(03):P03007, 2017.
- [45] K. Österberg. Timing Measurements in the Vertical Roman pots of the TOTEM experiment, technical report. Technical report, CERN-LHCC-2014-020 TOTEM-TDR-002, 2014.
- [46] CMS-TOTEM. CMS-TOTEM Precision Proton Spectrometer. Technical report, CERN-LHCC-2014-021 TOTEM-TDR-003 CMS-TDR-13, 2014.
- [47] V. Grilj, N. Skukan, M. Jakšič, M. Pomorski, W. Kada, T. Kamiya, and T. Ohshima. The evaluation of radiation damage parameter for CVD diamond. *Nuclear Instruments and Methods in Physics Research Section B: Beam Interactions with Materials and Atoms*, 372:161–164, 2016.
- [48] H. Tsutsui, T. Ohtsuchi, K. Ohmori, and S. Baba. X-ray energy separation method using a CdTe semiconductor X-ray imaging sensor and photon counting method. *IEEE Transactions on nuclear science*, 40(1):40–44, 1993.
- [49] C. Szeles. CdZnTe and CdTe materials for X-ray and gamma ray radiation detector applications. *Physica status solidi (b)*, 241(3):783–790, 2004.

- [50] A. Lindström, S. Mirbt, B. Sanyal, and M. Klintonberg. High resistivity in undoped CdTe: carrier compensation of Te antisites and Cd vacancies. *Journal of Physics D: Applied Physics*, 49(3):035101, dec 2015.
- [51] A. Cola, I. Farella, J. Pousset, and A. Valletta. On the relation between deep level compensation, resistivity and electric field in semi-insulating CdTe:Cl radiation detectors. *Semiconductor Science and Technology*, 31(12):12LT01, oct 2016.
- [52] Y. Eisen, A. Shor, and I. Mardor. CdTe and CdZnTe X-ray and gamma-ray detectors for imaging systems. *IEEE Transactions on Nuclear Science*, 51(3):1191–1198, 2004.
- [53] I. Visoly-Fisher, S. R. Cohen, and D. Cahen. Direct evidence for grain-boundary depletion in polycrystalline CdTe from nanoscale-resolved measurements. *Applied physics letters*, 82(4):556–558, 2003.
- [54] S. Kirschenmann, S. Bharthuar, E. Brücken, M. Golovleva, A. Gädda, M. Kalliokoski, P. Luukka, J. Ott, and A. Winkler. Employing infrared microscopy (IRM) in combination with a pre-trained neural network to visualise and analyse the defect distribution in cadmium telluride crystals. *Journal of Instrumentation*, 16(8), August 2021.
- [55] Alexander Winkler. *Comparison of characterization methods for CdTe/ CdZnTe radiation detector materials and development of an automated test system*. PhD thesis, May 2011.
- [56] F. Hartmann. *Evolution of Silicon Sensor Technology in Particle Physics*. Springer Tracts in Modern Physics. Springer Berlin Heidelberg, 2008.
- [57] G. Lutz. *Semiconductor Radiation Detectors*. Springer-Verlag Berlin Heidelberg, 1999.
- [58] A. Junkes. *Influence of radiation induced defect clusters on silicon particle detectors*. PhD thesis, Hamburg U., 2011.
- [59] V. A. J. Van Lint. *Mechanisms of Radiation Effects in Electronic Materials (Volume 1)*. Wiley, 1980.
- [60] R. Radu, I. Pintilie, L. C. Nistor, E. Fretwurst, G. Lindstroem, and L. F. Makarenko. Investigation of point and extended defects in electron irradiated silicon - dependence on the particle energy. *Journal of Applied Physics*, 117(16):164503, 2015.
- [61] M. Moll. *Radiation damage in silicon particle detectors: Microscopic defects and macroscopic properties*. PhD thesis, Hamburg U., 1999.
- [62] B. R. Gossick. Disordered regions in semiconductors bombarded by fast neutrons. *Journal of Applied Physics*, 30(8):1214–1218, 1959.

- [63] I. Pintilie, E. Fretwurst, and G. Lindström. Cluster related hole traps with enhanced-field-emission - the source for long term annealing in hadron irradiated si diodes. *Applied Physics Letters*, 92(2):024101, 2008.
- [64] Y. Gurinskaya, P. Dias de Almeida, M. Fernandez Garcia, I. Mateu Suau, M. Moll, E. Fretwurst, L. Makarenko, and I. Pintilie. Radiation damage in p-type EPI silicon pad diodes irradiated with protons and neutrons. *Nuclear Instruments and Methods in Physics Research Section A: Accelerators, Spectrometers, Detectors and Associated Equipment*, 958:162221, 2020. Proceedings of the Vienna Conference on Instrumentation 2019.
- [65] M. Moll. Development of radiation hard sensors for very high luminosity colliders - cern-RD50 project. *Nuclear Instruments and Methods in Physics Research Section A: Accelerators, Spectrometers, Detectors and Associated Equipment*, 511(1):97–105, 2003. Proceedings of the 11th International Workshop on Vertex Detectors.
- [66] G. Kramberger, V. Cindro, I. Mandić, M. Mikuž, and M. Zavrtanik. Determination of effective trapping times for electrons and holes in irradiated silicon. *Nuclear Instruments and Methods in Physics Research Section A: Accelerators, Spectrometers, Detectors and Associated Equipment*, 476(3):645–651, 2002. Proc. of the 3rd Int. Conf. on Radiation Effects on Semiconductor Materials, Detectors and Devices.
- [67] A.G. Kozorezov, J.K. Wigmore, A. Owens, R. den Hartog, A. Peacock, and Hala A Al-Jawhari. Resolution degradation of semiconductor detectors due to carrier trapping. *Nuclear Instruments and Methods in Physics Research Section A: Accelerators, Spectrometers, Detectors and Associated Equipment*, 546(1):209–212, 2005. Proceedings of the 6th International Workshop on Radiation Imaging Detectors.
- [68] J. Zhang, I. Pintilie, E. Fretwurst, R. Klanner, H. Perrey, and J. Schwandt. Study of radiation damage induced by 12keV X-rays in MOS structures built on high-resistivity *n*-type silicon. *Journal of Synchrotron Radiation*, 19(3):340–346, May 2012.
- [69] O. A. Dicks, J. Cottom, A. L. Shluger, and V. V. Afanas'ev. The origin of negative charging in amorphous Al_2O_3 films: the role of native defects. *Nanotechnology*, 30(20):205201, mar 2019.
- [70] Synopsys. Synopsys webpage. <https://www.synopsys.com/>, 2018. Accessed: January, 2018.
- [71] W. Shockley and W. T. Read. Statistics of the recombinations of holes and electrons. *Phys. Rev.*, 87:835–842, Sep 1952.
- [72] R. N. Hall. Electron-hole recombination in germanium. *Phys. Rev.*, 87:387–387, Jul 1952.

- [73] V. Eremin, E. Verbitskaya, and Z. Li. The origin of double peak electric field distribution in heavily irradiated silicon detectors. *Nuclear Instruments and Methods in Physics Research Section A: Accelerators, Spectrometers, Detectors and Associated Equipment*, 476(3):556–564, 2002. Proc. of the 3rd Int. Conf. on Radiation Effects on Semiconductor Materials, Detectors and Devices.
- [74] G. Kramberger, V. Cindro, I. Mandic, M. Mikuz, M. Milovanovic, M. Zavrtanik, and K. Zagar. Investigation of irradiated silicon detectors by Edge-TCT. *IEEE Transactions on Nuclear Science*, 57(4):2294–2302, 2010.
- [75] A. Morozzi. *Development and application of state-of-the-art device/circuit level TCAD simulation tools for the optimization of innovative Silicon-on-Diamond (SoD) semiconductor devices*. PhD thesis, Universita' Di Perugia, 2015/2016.
- [76] M. Brezeanu. *Diamond Schottky Barrier Diodes*. PhD thesis, University of Cambridge, 2007.
- [77] T. Shimomura, Y. Kubo, J. Barjon, N. Tokuda, I. Akimoto, and N. Naka. Quantitative relevance of substitutional impurities to carrier dynamics in diamond. *Physical Review Materials*, 2(9), Sep 2018.
- [78] F. Kassel, M. Guthoff, A. Dabrowski, and W. de Boer. Severe signal loss in diamond beam loss monitors in high particle rate environments by charge trapping in radiation-induced defects. *physica status solidi (a)*, 213(10):2641–2649, 2016.
- [79] A. Pu, V. Avalos, and S. Dannefaer. Negative charging of mono- and divacancies in IIa diamonds by monochromatic illumination. *Diamond and Related Materials*, 10(3):585 – 587, 2001. 11th European Conference on Diamond, Diamond-like Materials, Carbon Nanotubes, Nitrides and Silicon Carbide.
- [80] D. M. Caughey and R. E. Thomas. Carrier mobilities in silicon empirically related to doping and field. *Proceedings of the IEEE*, 55(12):2192–2193, Dec 1967.
- [81] C.-H. Su. Energy band gap, intrinsic carrier concentration, and fermi level of CdTe bulk crystal between 304 and 1067k. *Journal of Applied Physics*, 103(8):084903, 2008.
- [82] A. Castaldini, A. Cavallini, B. Fraboni, P. Fernandez, and J. Piqueras. Deep energy levels in CdTe and CdZnTe. *Journal of Applied Physics*, 83(4):2121–2126, 1998.
- [83] G. Kramberger. Advanced transient current technique systems. *Proc. Sci.*, 227:032, 2014.

Publication I

Naaranoja, T., Golovleva, M., Martikainen, L., Berretti, M., and Österberg, K.
Space charge polarization in irradiated single crystal CVD diamond

Reprinted with permission from
Diamond and Related Materials
Vol. 96, pp. 167–175, 2019.
© 2019, Elsevier B.V.



Contents lists available at ScienceDirect

Diamond & Related Materials

journal homepage: www.elsevier.com/locate/diamond

Space charge polarization in irradiated single crystal CVD diamond

T. Naaranoja^{a,b,*}, M. Golovleva^{a,c}, L. Martikainen^{a,b}, M. Berretti^a, K. Österberg^{a,b}^a Helsinki Institute of Physics, Gustaf Hällströmin katu 2, P.O. Box 64, FI-00014, University of Helsinki, Finland^b Department of Physics, Gustaf Hällströmin katu 2, P.O. Box 64, FI-00014, University of Helsinki, Finland^c Lappeenranta University of Technology, Skinnarilankatu 34, 53850 Lappeenranta, Finland

ARTICLE INFO

Keywords:

Single crystal diamond radiation induced effects
 Electrical properties characterization
 Defects
 Detectors
 Sensors

ABSTRACT

Single crystal CVD (scCVD) diamond is an attractive material for particle detection in high energy physics for its good time resolution and reported outstanding radiation tolerance. In addition to direct signal loss via charge carrier trapping, polarization effect, caused by non-homogeneous filling of trap defects, is a known cause of signal degradation in irradiated scCVD diamond. This phenomenon was studied by intentionally polarizing irradiated diamonds. Even the relatively lightly irradiated (10^{14} protons/cm²) diamonds exhibited strong enough polarization to collapse the electric field with moderate rate of 5 MeV alpha particles. The transient current measurements were reproduced with TCAD simulations. The hypothesis that the polarization is caused by single neutral defect type in the bulk, was tested using two generic models. Neither one has a satisfactory agreement with the measurement data, which indicates that trapping at the interfaces play a significant role in space charge polarization.

1. Introduction

Diamonds are an attractive material for radiation detectors first of all due to their outstanding radiation tolerance [1] and excellent time resolution, when measuring the time-of-flight for hadrons [2]. Its wide band gap results in high resistivity and small leakage currents in diamond-based detectors. Hence, diamond has found its way to such harsh radiation environments as experiments at CERN's Large Hadron Collider and is currently used in CMS-TOTEM Precision Proton Spectrometer [3] as time-of-flight detector and previously in TOTEM timing upgrade [4].

Radiation damage in scCVD diamond is currently explained by introduction of neutral vacancy defects that affect both holes and electrons collection. Slightly higher trapping probability of electrons than holes has previously been observed [5–7]. Polarization under irradiation with heavy ions, has reportedly higher trapping probability for holes [8].

However, it has been observed that low fluence laboratory studies and high fluence in situ experience differ from each other [5]. One possible explanation for the difference is the polarization due to charge trapping, which is more easily avoided in laboratory than in a particle physics experiment, where the particle flux is not a controlled parameter. Polarization occurs as build-up of charge inside detector's bulk that eventually reduces charge collection efficiency (CCE) of the

detector. It can be countered by either filling all traps, e.g. by irradiating with a beta-source or with UV light, or periodically releasing trapped charge e.g. by periodically switching bias voltage on and off.

Similar effects might arise from charge trapping in the diamond-metal interface. Such Schottky contact would also enhance the trapping of charge in bulk defects. To avoid polarization effectively in the experiments, the mechanism leading to it needs to be understood.

The detector design in this study corresponds to the largest pixel size that has been used in the TOTEM and PPS timing detectors. This corresponds to the worst case scenario for interface trapping in these experiments. Especially the efficacy for mitigating polarization by switching bias voltage on and off was investigated since it is easy method to adapt in experiments. The polarization in this study is expected to have contribution both from the non-homogeneous trapping in the diamond bulk, trapping at the interfaces and interface potential enhanced trapping in bulk. As the bulk defects are often assumed to be the sole contributor to polarization and bulk defects are relatively well known, polarization originating on trapping in the bulk only is used as the null hypothesis.

* Corresponding author at: Helsinki Institute of Physics, Gustaf Hällströmin katu 2, P.O. Box 64, FI-00014, University of Helsinki, Finland.

E-mail address: tiina.naaranoja@helsinki.fi (T. Naaranoja).

<https://doi.org/10.1016/j.diamond.2019.03.007>

Received 31 October 2018; Received in revised form 5 February 2019; Accepted 11 March 2019

Available online 15 March 2019

0925-9635/ © 2019 Published by Elsevier B.V.

Table 1
Summary of the scCVD diamond samples.

Thickness (μm)	Electrode	Fluence (protons/ cm^2)
340 ± 10	TiW	$(1.10 \pm 0.08) \times 10^{14}$
340 ± 10	Cr/Au	$(0.97 \pm 0.07) \times 10^{14}$
540 ± 10	TiW	$(1.06 \pm 0.07) \times 10^{14}$
540 ± 10	TiW	$(4.5 \pm 0.3) \times 10^{15}$
540 ± 10	Cr/Au	$(4.4 \pm 0.3) \times 10^{15}$

2. Material and methods

2.1. Samples

The diamond substrate for this study was procured from Element Six [9]. The used material was the highest purity single crystal Chemical Vapor Deposition (scCVD) diamond available, so-called “electronic grade”. For the electrodes a simple test pattern was used: single $4.2 \times 4.2 \text{ mm}^2$ square pad on a $4.5 \times 4.5 \text{ mm}^2$ diamond surface. For the electrodes two materials were used: TiW produced by Princeton [10] and Cr/Au by Applied Diamond [11]. The samples are summarized in Table 1 and one of the samples is depicted in Fig. 1.

2.2. Irradiation

Five single crystal diamonds were irradiated at CERN IRRAD facility with 24 GeV/c protons, three to a target fluence of 10^{14} protons/ cm^2 and two to 5×10^{15} protons/ cm^2 . The dosimetry results for all irradiation in 2017 are publicly available [12]. The standard beam parameters were used and the full width at half maximum of the Gaussian beam was $14.0 \pm 0.4 \text{ mm}$ in vertical direction and $14.3 \pm 0.07 \text{ mm}$ in horizontal direction at the sample location. The fully processed diamond detectors were irradiated with bias in ambient conditions and the beam induced currents in diamond were monitored.

2.3. Transient current technique

After irradiation the diamond detectors were studied with a mixed nuclide α -source with nuclides (and α particle energies) Am-241 (5.486 MeV), Cm-244 (5.805 MeV) and Pu-239 (5.156 MeV) in equal quantities. The particle energies are below the level where plasma effect is expected i.e. single interaction does not inject enough charge to

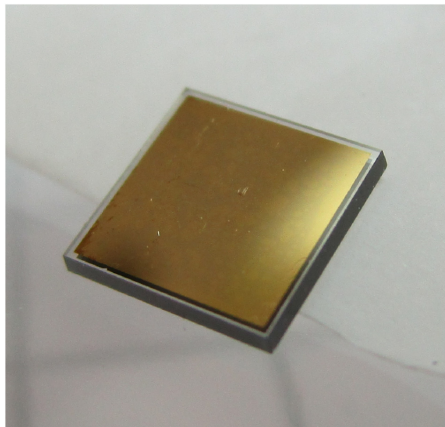


Fig. 1. Photograph of a 500 μm thick diamond with Cr/Au electrode.

significantly perturb the electric field. The α particles deposit charge close to the surface, which allows the investigation of the hole and electron transport properties separately. One type of charge carrier is almost immediately collected at the closest electrode and the other drifts through the bulk to the other electrode. Using Shockley-Ramo theorem [13,14], the electric field inside the detector can be deduced.

The bias voltage was supplied using a Keithley 2410 SourceMeter unit. A single-channel readout electronics system was used. It consisted of a Particulars AM-01 A broadband amplifier, that has a bandwidth of 10 kHz–2 GHz and gain of 53 dB, and a Particulars bias T with bandwidth of 100 kHz–2 GHz. The signal was read out using a LeCroy WavePro 7300A 3 GHz digital oscilloscope and a custom-written data acquisition software. For the used oscilloscope settings the sampling period was 100 ps and jitter 1 ps.

The α source was placed at a 2 mm distance from the diamond, which is as close as possible without touching in the transient current technique (TCT) setup in order to achieve as strong space charge polarization as possible. The estimated particle rate was 5000 ± 800 particles/s at the detector surface in an area of $A_{irr} = (14 \pm 3) \text{ mm}^2$. The maximum observed hit rate was restricted to about 14 events/s by the readout system.

The radiation source was placed on the diamond and bias voltage was ramped up with speed of 200 V/s. The time for polarization was recorded from turning on the bias voltage. After reaching the polarized state, the bias voltage was turned off until the polarization had fully dissipated and the measurement was repeated 5 to 10 times. The initial state before polarization was recorded during the first 10 s after turning bias on.

2.4. TCAD simulations

In order to investigate and understand the scCVD diamond bulk internal properties better, numerical simulations of the initial state before the polarization were carried out using Synopsys Sentaurus Technology Computer-Aided Design (TCAD) software [15].

The simulated device structure had dimensions $(100 \times 300 \times 1) \mu\text{m}^3$, where 300 μm corresponds to the device thickness, and it was scaled with an area factor A to match the dimensions of the real device. In the simulation the diamond bulk was considered with the concentration $n_i = 10^{-27} \text{ cm}^{-3}$ and Schottky type contacts with a low barrier height of 0.8 eV. At present this material is not included in the material libraries of TCAD simulation tools, therefore, all the physical parameters of the scCVD diamond, such as permittivity, optical refractive index and band gap, were defined by hand using data from Refs. [16, 17]. The band gap energy used was 5.47 eV with electron affinity 1.73 eV for the oxygen-terminated diamond surfaces.

Nitrogen and boron are known donor and acceptor species in diamond. In order to take into account the effect of these impurities, two impurity levels were introduced into the diamond band gap: acceptor and donor type levels with energies $E_v + 0.368 \text{ eV}$ and $E_c - 1.7 \text{ eV}$, respectively, each having concentration 10^{12} cm^{-3} . The concentration was let vary between the maximum concentration 10^{14} cm^{-3} declared by the producer [9] and the minimum concentration required for stable simulation 10^{12} cm^{-3} . The used concentration 10^{12} cm^{-3} is the best fitting value in this regime. The impurities' electron $\sigma_e = 10^{-14} \text{ cm}^2$ and hole $\sigma_h = 10^{-13} \text{ cm}^2$ capture cross sections were found by fitting simulated transients to the measurement results. The obtained cross section for electron in boron is in good agreement with the experimentally measured value [18], but nitrogen has larger obtained cross section than found experimentally [18]. The mobilities were determined experimentally in Section 4.1 and used as an input parameter in the simulations.

Transient analysis with α -particles was performed on the described above structure and then compared with the corresponding measurements carried out on real devices stimulated with alpha particles. The α -particle interaction was simulated using the inbuilt Heavy Ion Model

with 12 μm radiation length.

To reproduce the TCT data for irradiated samples, a neutral level with energy $E_v + 2.85$ eV corresponding to a neutral mono-vacancy [19] was introduced. A good agreement with the experimental data was obtained by tuning the defect concentration to 10^{14} cm^{-3} , which was also measured in Section 4.1, and electron and hole capture cross sections to $\sigma_e = 1 \times 10^{-14} \text{ cm}^2$ and $\sigma_h = 5 \times 10^{-15} \text{ cm}^2$, respectively. When compared to measured defect concentrations for 26 MeV proton irradiated diamonds by Pomorski [20], defect concentration in the order of 10^{14} cm^{-3} is expected. Capture cross section close to the order of 10^{-15} cm^2 is also expected for neutral defects [21].

3. Theory

3.1. Current transient form

The form of the current transient follows the electric field inside the detector according to the Shockley-Ramo theorem [13,14]. The induced current for single charge carrier is

$$i(x) = q\nu \cdot E_0(x), \quad (1)$$

where q is the elementary charge, ν is the instantaneous velocity, and $E_0(x)$ is the electric field. In case of parallel plates geometry, the current is given by

$$i = \frac{q\mu V_{bias}^2}{d^2}, \quad (2)$$

where μ is the mobility of the charge carrier, V_{bias} is the voltage difference applied between the electrodes, and d is the distance between the electrodes.

When the charge carrier lifetime $\tau_{e,h}$ becomes shorter than the transient time $t_{tr} = d/\nu$, the time that it takes for charge carrier to drift through detector, the transient form is affected by the loss of charge due to trapping. When the trapped charge is not significantly distorting the electric field (i.e. before the crystal starts to polarize), the induced current for single charge carrier type with initial injected charge q_0 is given by

$$i_{e,h} = \frac{q_0\mu V_{bias}^2}{d^2} e^{-\frac{t}{\tau_{e,h}}}. \quad (3)$$

Such change in charge carrier lifetime is expected when defects (e.g. radiation damage) are introduced.

The charge carrier velocity $v = d/t_{tr}$ can be also expressed by using an empirical formula by Caughey and Thomas [22].

$$v = v_{sat} \frac{(E/E_c)}{[1 + (E/E_c)^\beta]^{1/\beta}}, \quad (4)$$

where v_{sat} is the saturation velocity, $E = V_{bias}/d$ is the electric field, E_c is the critical field, and β is an empirical fit parameter. Then the mobility μ is given by

$$\mu = \frac{\mu_0}{[1 + (E/E_c)^\beta]^{(1+\frac{1}{\beta})}}, \quad (5)$$

where μ_0 is the zero-field mobility that is calculated as

$$\mu_0 = \frac{v_{sat}}{E_c}. \quad (6)$$

3.2. Polarization

Since no model describing the charge accumulation during polarization developed specifically for diamond was found, two models, multiple scales model describing the polarization in Cd(Zn)Te detectors [23] and a simple model based on general equations for charge trapping [24], were used. In both models the electrode-diamond interface is assumed Ohmic, high active trap concentration is assumed (i.e.

$qN_{trap} \gg C_{detector}V_{bias}$) and increased trapping probability due to partial polarization is not taken into account. Only one charge carrier is considered at a time, while the other charge carrier is assumed to be immediately collected and not contributing to the polarization.

The crystal is fully polarized, when a sufficient charge is trapped to collapse the electric field in the detector. The minimum charge required to collapse the electric field is denoted by Q^* , whereas the time t^* it takes to reach this critical state is obtained by numerically solving the time dependent accumulated charge $Q(t = t^*) = Q^*$.

3.2.1. Multiple scales model

The mathematical model for describing polarization in wide-bandgap semi-conductor has been developed by Bale and Szeles [23] mainly for Cd(Zn)Te applications. It was named multiple scales model for taking into account the different time scales for charge transport, trapping, and de-trapping.

The time dependence of charge accumulation in this model is given by

$$Q(t) = \frac{qA_{irr}\phi E_c}{v_{eff} \epsilon_E} \begin{cases} 1 - e^{-\frac{v_{eff} T}{\Lambda}} - \frac{v_{eff} T}{\Lambda} e^{-\frac{T}{\Lambda}}, & T \leq L/v_{eff} \\ 1 - \left(1 + \frac{L}{\Lambda}\right) e^{-\frac{T}{\Lambda}}, & T > L/v_{eff} \end{cases} \quad (7)$$

where q is the elementary charge, A_{irr} is the area under irradiation, ϕ is the particle flux, E_c is the kinetic energy of one alpha-particle, ϵ_E is the energy required to produce an electron-hole pair, L is the distance between parallel electrodes, Λ describes the initial spatial distribution of accumulated charge, $T = t_{tr}t$ is time scaled with transient time in non-polarized detector, and v_{eff} is the effective charge carrier speed reduced by the so called 'stop and go' process, where the carriers go through multiple trapping in the process of traversing through the detector:

$$v_{eff} = \frac{\tau_{e,h}}{\tau_{e,h} + \tau_D} \mu_{e,h} E, \quad (8)$$

where $\tau_{e,h}$ is the electron or hole lifetime, $\mu_{e,h}$ is mobility, E is the electric field, and τ_D is the mean detrapping time.

The model was adjusted for diamond by choosing the mean free path of charge carrier as the characteristic length of spatial distribution of trapped charge

$$\Lambda = v_{e,h} \tau_{e,h}, \quad (9)$$

where charge carrier velocity v is given by Eq. (4). In addition to charge distribution, the minimum accumulated charge, Q^* , required to collapse the electric field is affected by the Λ . In the original formulation $mbda$ is the radiation length of X-rays and also the spatial distribution of generated charge carriers follows the exponential form $e^{-x/\Lambda}$. However, it does not hold in our case. The difference in spatial distribution of generated charge carriers affects the location of the pinch point x^* , where the electric field has its minimum. This means that the equation for the minimum accumulated charge Q^* , that is required to collapse the electric field, might not be accurate. It is, however, used in the calculations.

$$redblackQ^* = \frac{A\epsilon V_{bias,black}}{\Lambda} \quad (10)$$

where $\epsilon = \epsilon_r \epsilon_0 = 5.0468 \cdot 10^{-11} \text{ F/m}$ is the permittivity of diamond.

3.2.2. Simple model

An alternative model was derived from the classic formulation of time dependence on charge collection in presence of traps by Martini and McMath [24] originally for Ge(Li) and Si(Li) detectors. They presented an analytic solution for the case $t \leq t_{tr}$

$$Q_{coll} = Q_0 \frac{\tau_{eff}}{t_{tr}} \left[\frac{t}{\tau_D} + \frac{\tau_{eff}}{\tau_{e,h}} (1 - e^{-t/\tau_{eff}}) \right], \quad (11)$$

where $\tau_{e,h}$ is the lifetime of a charge carrier and τ_{eff} is given by

$$\tau_{eff} = \frac{\tau_{e,h}\tau_D}{\tau_{e,h} + \tau_D}. \quad (12)$$

Then the charge in the detector at a given time is

$$Q(t) = Q_0 - Q_{coll}. \quad (13)$$

where Q_0 is the injected charge. Assuming $\tau_{e,h} < \tau_D$ and $t_{tr} < \tau_D$ and requiring $Q_{coll}(t > \tau_D) = Q_0$, the charge remaining in detector is derived

$$Q(t) = Q_0 \begin{cases} 1 - \kappa \frac{\tau_{eff}}{t_{tr}} \left[\frac{t}{\tau_D} + \frac{\tau_{eff}}{\tau_{e,h}} (1 - e^{-t/\tau_{eff}}) \right], & t \leq t_{tr} \\ 1 - \kappa \frac{\tau_{eff}}{t_{tr}} \left[\frac{t}{\tau_D} + \frac{\tau_{eff}}{\tau_{e,h}} (1 - e^{-t_{tr}/\tau_{eff}}) \right], & t_{tr} < t \leq \tau_D \\ 0, & t > \tau_D, \end{cases} \quad (14)$$

where κ is a dimensionless normalization constant

$$\frac{1}{\kappa} = \frac{\tau_{eff}}{t_{tr}} \left[1 + \frac{\tau_{eff}}{\tau_{e,h}} (1 - e^{-t_{tr}/\tau_{eff}}) \right]. \quad (15)$$

The charge begins to accumulate, when the total injected charge also depends on time:

$$Q_0(t) = \frac{q\phi A_{irr} E_{\alpha}}{\epsilon_E}. \quad (16)$$

The total accumulated charge is obtained by convoluting the injected charge with the time dependence of charge collection $f(t) = Q(t)/Q_0$ from Eq. (14)

$$Q_{acc}(t) = f(t) * Q_0(t) = \int_0^{\infty} f(t') Q_0(t - t') dt', \quad (17)$$

which is performed numerically.

The minimum trapped charge Q_{min}^* required to collapse the electric field is taken to be equal to the capacity of the detector, as a capacitor, to store charge:

$$Q_{min}^* = V_{bias} \frac{\epsilon A}{d} \quad (18)$$

where ϵ is the permittivity of diamond, A is the area of the parallel electrodes, and d is the thickness of the diamond crystal. For instance, the minimum number of charge carriers required to collapse the electric field in a 300 μm thick diamond used in this study is approximately $2 \cdot 10^{10}$ electrons/holes when the diamond is biased to 1 kV.

4. Results and discussion

4.1. State prior to polarization

The transients recorded within 10 s of turning on the bias voltage and replicated with simulations are shown in Figs. 2 and 3. The measured signals have been post-processed to correct reflections and under- or overshoots. The factor 2 difference in transient amplitudes in Figs. 2 and 3 is due to different gain in electronics. Electron and hole TCT measurements of non-irradiated detectors in Fig. 2 show the expected rectangular pulse shape, indicating a constant electrical field. Simulated and experimental transients are in good agreement. In the beginning of the simulated transients a peak from the minority charge carrier is observed, which is filtered by the electronics in the measurements. In simulations it was dampened with a 50 Ω resistor in series with the detector. From Fig. 2 one can observe that the signal amplitudes for the negative voltages get higher than the simulated ones, which could be explained by much more probable trapping of the electrons comparing to holes, or by increased mobility.

The charge collection efficiency (CCE) of the sensors can be obtained by numerically integrating over the current transient with

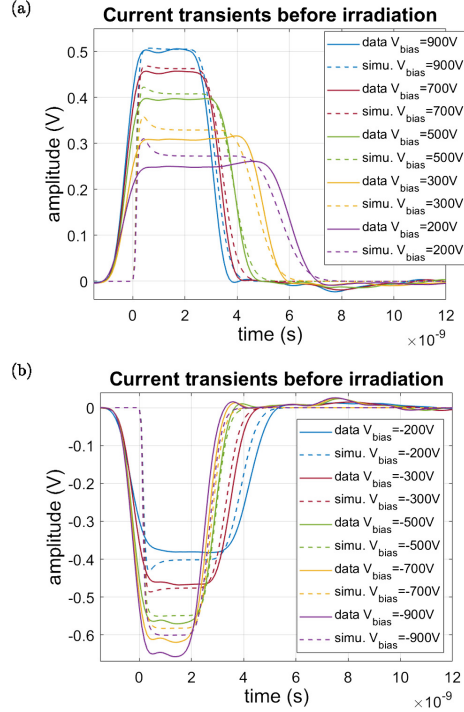


Fig. 2. Measured and simulated TCT transients for 300 μm thick non-irradiated diamond collecting electrons (a) and holes (b).

respect to time and comparing the result to non-irradiated reference. Fig. 4 shows the CCE measured in this manner for all of the irradiated sensors in a non-polarized state. The low fluence samples show no significant deterioration of CCE. The 300 μm thick diamond shows a better charge collection than the reference, which is most likely caused by the normal level of nitrogen impurities present in the 500 μm thick non-irradiated reference diamond and is not related to irradiation. The high fluence samples show severely reduced CCE.

The charge transport properties such as mobility and its high-field dependence were determined experimentally and used as parameters in the simulations. The drift velocity was obtained by dividing the transient time with the detector thickness. The transient time was measured from reaching 20% of the signal maximum on the rising edge to going below 15% of the signal maximum on the falling edge. In Fig. 5 the drift velocities of both non-irradiated diamond and diamond irradiated to fluence of 10^{14} p/cm² are fitted with Eq. (4) and compared with the similar fits by Pomorski in his thesis [20]. In Table 2 the results of these fits are summarized. It is important to notice that in the case of the irradiated diamond, the detector is often partially polarized with the lower bias voltages ($V_{bias}/d < 1$ V/ μm). The zero field mobility μ_0 and critical field E_c are not very reliable. The saturation velocity, however, is not very sensitive to low-field velocities and in the case of electrons it is significantly lowered from the value prior to irradiation.

In the simulations the electron transport properties of Pomorski fit was used, since it is in good agreement with the data in this study ($R^2 = 0.9678$) and it takes into account higher electric fields than accessible in this study. The Pomorski fit is, however, not applicable to the

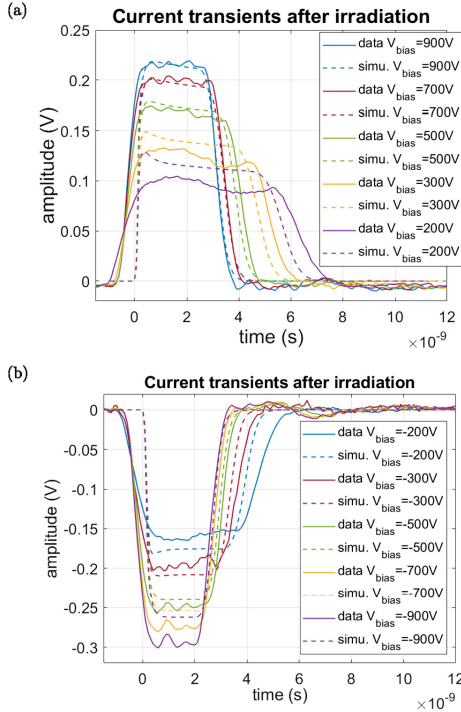


Fig. 3. Measured and simulated TCT transients for 300 μm thick diamond irradiated to 10^{14} p/cm² collecting electrons (a) and holes (b).

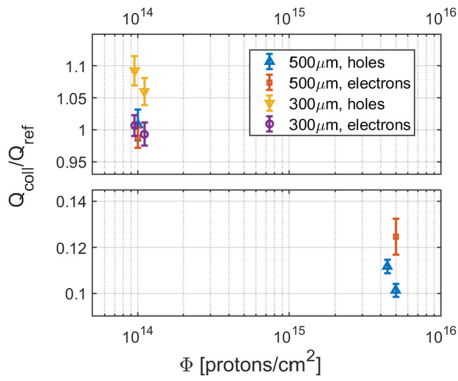


Fig. 4. Collected charge Q_{coll} (area of current transient) for different irradiation fluences Φ . Scaled with the collected charge Q_{ref} of non irradiated reference with thickness of 500 μm. Note that the y-axis has been broken for a better illustration of the data points.

holes transport and there the fit in this study is used. In the simulation of the irradiated diamond, the values for obtained for non-irradiated diamond were used for simplicity.

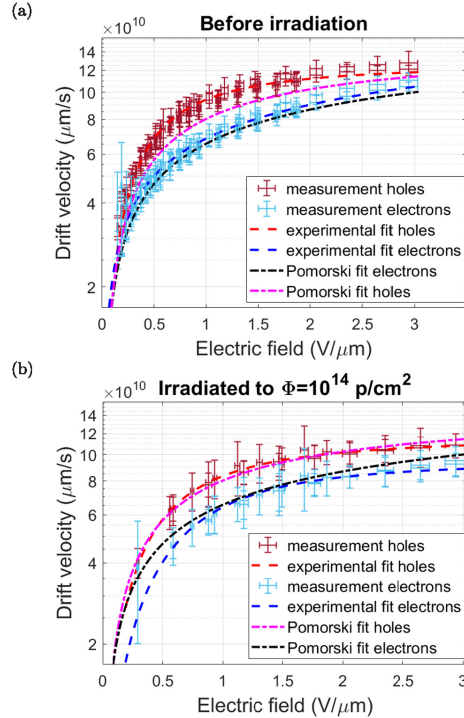


Fig. 5. The measured charge transport velocities both (a) before and (b) after irradiation to 10^{14} p/cm² are fitted with Eq. (4) and compared to fits by Pomorski [20].

A clear state before polarization could be observed for the detectors with lower fluence of 10^{14} p/cm². The electron and hole lifetimes $\tau_e = (23 \pm 2)$ ns and $\tau_h = (80 \pm 30)$ ns, respectively, were found by fitting Eq. (3) to the reflection and undershoot corrected transient at bias voltage roughly corresponding to the electric field of 1 V/μm.

With the settings used in this study, a non polarized state could not be observed for the sensors irradiated to the higher fluence of $5 \cdot 10^{15}$ p/cm². When radiation source was moved to a distance of 12 mm from the detector surface and their radiated area was reduced to 50% of the original with a grid-like collimator, a non polarized state could be briefly observed for collecting holes with bias voltage -1 kV over 500 μm thick detector. The duration of the current transient at 20% of the amplitude maximum was approximately 1 ns. The charge carrier lifetime was estimated to be in order of $\tau_h = 0.25 \dots 0.5$ ns. With positive voltages (collecting electrons) a non polarized state could not be observed for detectors irradiated to fluence of $5 \cdot 10^{15}$ p/cm².

4.2. Polarization

A polarization effect, where charge collection efficiency drops suddenly, is observed for all diamond detectors after irradiation with protons and is absent in the same detectors before the irradiation. In Fig. 6 the time evolution of current transient is shown. Fig. 7 summarizes the evolution charge carrier collection properties during the polarization. The transient amplitude and charge carrier velocity decrease first slowly, while charge collection efficiency (CCE) and

Table 2
Charge transport properties for electrons (e) and holes (h) before and after irradiation compared to experimental values by Pomorski [20] and Kassel et al. [5].

		E_c (kV/cm)	μ_0 (cm ² /V·s)	v_{sat} (cm/s)	β	R ²
$\Phi = 0$ p/cm ²	e	3.3 ± 0.9	15,000 ± 9900	(5 ± 3) · 10 ⁷	0.27 ± 0.07	0.977
	h	6.4 ± 0.2	2000 ± 80	(1.28 ± 0.03) · 10 ⁷	1.4 ± 0.1	0.983
$\Phi = 10^{14}$ p/cm ²	e	10.5 ± 0.9	910 ± 90	(0.95 ± 0.05) · 10 ⁷	1.9 ± 0.5	0.947
	h	7.7 ± 0.4	1520 ± 90	(1.17 ± 0.03) · 10 ⁷	1.5 ± 0.2	0.987
Pomorski $\Phi = 0$	e	5.8 ± 0.8	4500 ± 500	(2.6 ± 0.2) · 10 ⁷	0.42 ± 0.01s	0.998
	h	5.7 ± 0.5	2750 ± 70	(1.57 ± 0.14) · 10 ⁷	0.81 ± 0.01	0.999
Kassel	e	4.8 ± 0.9	10,000 ± 2000	(4.5 ± 1.2) · 10 ⁷	0.30 ± 0.03	–
	h	5.8 ± 0.1	2660 ± 40	(1.54 ± 0.03) · 10 ⁷	0.86 ± 0.02	–

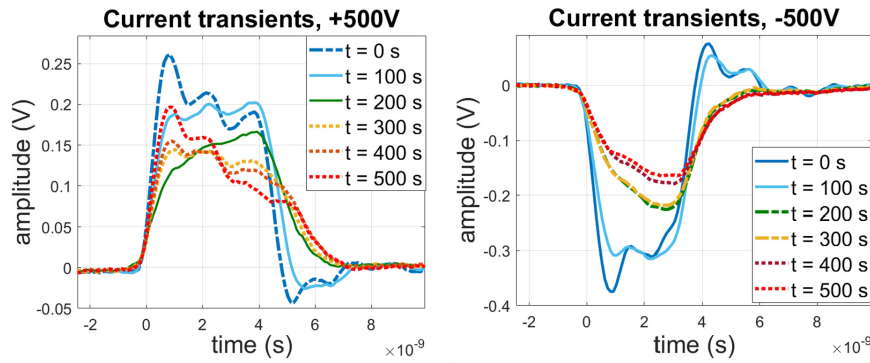


Fig. 6. Current transients for electrons at different times after turning bias voltage on. The transient form follows the electric field in the 300 μ m thick diamond detector with TiW electrodes that has been irradiated to 10¹⁴ protons/cm².

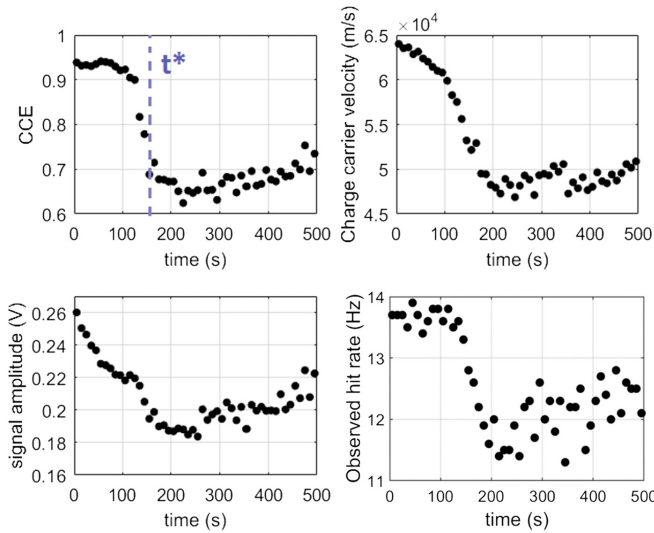


Fig. 7. Evolution of electron transport properties with time within a sensor undergoing polarization. Charge collection efficiency (CCE) is the normalized integral of current transient, signal amplitude the maximum of the current transient. The observed hit rate is first limited by the set-up. The sudden drop indicates a drop in device efficiency. The detector used is same as in Fig. 6.

observed rate remain constant. At a certain point CCE, transient amplitude, charge carrier velocity and observed rate drop abruptly. This happens when the critical amount of charge Q^* has accumulated in the detector volume.

To investigate the polarization further, the time t^* it takes for the irradiated detectors to polarize was measured under constant alpha-particle rate. The polarization times t^* were obtained by fitting a straight line to the falling edge in the charge collection. The time, when

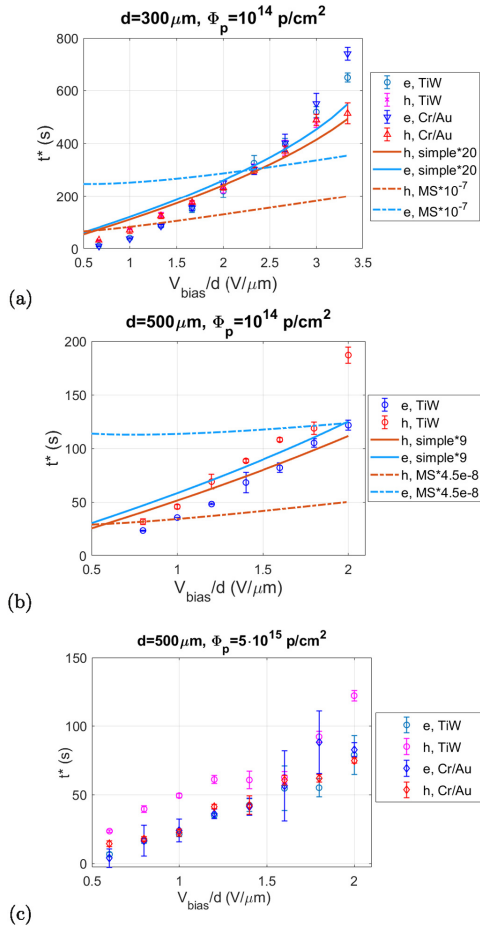


Fig. 8. Time t^* to reach critical field Q^* as a function of bias voltage for a) 300 μm thick detectors irradiated to 10^{14} protons/ cm^2 , b) 500 μm thick detector irradiated to 10^{14} protons/ cm^2 and c) 500 μm thick detectors irradiated to $5 \cdot 10^{15}$ protons/ cm^2 compared to model calculations with simple model and multiple scales (MS) model discussed in Section 3.2. The model parameters were either measured or retrieved from literature. The calculated values are scaled by factors of 20, 8 and 2 for simple model, and 10^{-7} and $4.5 \cdot 10^{-8}$ for multiple scales model in order to place them comfortably in the same figure with measurement results.

the fitted line crosses noise threshold, was taken as t^* . The error bars in the measurements reflect the goodness of fit for the linear fit. This approach was chosen, because in some cases the polarization started developing already during voltage ramp-up and only the falling edge could be observed. For the high fluence samples only few measurement points were collected on the falling edge and this is reflected in the error bars. The polarization times grouped by detector thickness and proton fluence are presented in Fig. 8 with example calculations of the computational models in Section 3.2. The experimental values found for fluence 10^{14} p/ cm^2 in Section 4.1 were used in the models together

with literature values already discussed in Section 2.4. De-trapping time $\tau_D = 40$ s was used. In the measurements, the polarization was observed to dissipate within 20 to 45 s after turning the bias voltage off. The used 40 s was shortest de-trapping time that consistently led to full polarization with both models. The model calculations for 500 μm thick diamond irradiated to $5 \cdot 10^{15}$ p/ cm^2 were not successful. The simple model is valid only for $\tau_{e,h} > \tau_D$, which is no longer true.

The multiple scales model predicts considerably longer time for reaching polarization, $t^* = \text{few years}$, than the measured few minutes. This is most likely due to pinch point for the electric field extending outside the detector volume, which may result in erroneous results. The multiple scales model takes the spatial distribution of the trapped charge into consideration. In the original formulation the spatial distribution depends primarily from the initial spatial distribution of the injected charge. This was adapted to diamond by taking the mean free path of the charge carrier as a measure of the charge spatial distribution. As the transient time of the charge carriers is close to the charge carrier lifetime, this might lead to unexpected behavior of the model.

The simple model predicts faster polarization than observed. This is most likely because the model does not take into account the spatial distribution of the trapped charge. Evenly distributed charge does not contribute to the collapse of the electric field in the same degree as locally clustered charge. The simple model result is closer to the measurement with 500 μm thick detector.

Fig. 9 shows the ratio of polarization times for all samples and model calculations of the two models. The prediction of the multiple scales model differs significantly from all measurements. The simple model is similar to the measurement data in high field regime. At low field, the ratio of the polarization times is significantly different between different samples. The samples seem to be divided into two groups: ones having nearly constant relation and others distinctive direct proportionality to electric field. The first group is similar to the simple model, where polarization is caused solely by neutral deep trap level in the bulk of the detector. The other group deviates significantly from the simple model at low field regime. This could indicate, for example, a non-neutral trap level in bulk or significant trapping in the diamond-metal interface in addition to the neutral defect level(s) in the bulk. The latter interpretation is supported by the fact that both 300 μm samples fall into the category that deviates from the model prediction.

The conditions assumed in Section 3.2 might not be valid. In particular the condition that the number of trapping defects in the detector volume is much larger than trapped charge required to collapse the electric field. The simulations are in agreement with the defect concentration of 10^{14} cm^{-3} for diamond irradiated to fluence of 10^{14} protons/ cm^2 . This means that the maximum trapped charge in the active volume of a 300 μm thick detector is approximately equivalent to $5 \cdot 10^{11}$ electrons. The minimum charge required to collapse the field is equivalent to $2 \cdot 10^{10}$ electrons. Clearly there is enough defects to collapse the field, but, to achieve the buildup of space charge necessary to collapse the electric field, nearly all traps might need to be filled.

5. Conclusions

Five high purity single crystal diamond-based detectors were investigated for space charge polarization using α -TCT measurements and TCAD simulations. Strong enough polarization effect to collapse electric field under the high flux of injected charge from α -particles in proton irradiated diamond was observed.

Estimated charge carrier lifetimes that favor the trapping of electrons in irradiated diamond are in accordance with previous studies [5–7].

For the low fluence (10^{14} p/ cm^2) detectors, turning bias voltage periodically off for 1 min and back on is an effective method for removing polarization. In this case full charge collection can be restored. In the measurement of minimum ionizing particles the injected charge per particle is much less than in this experiment. It follows, that the

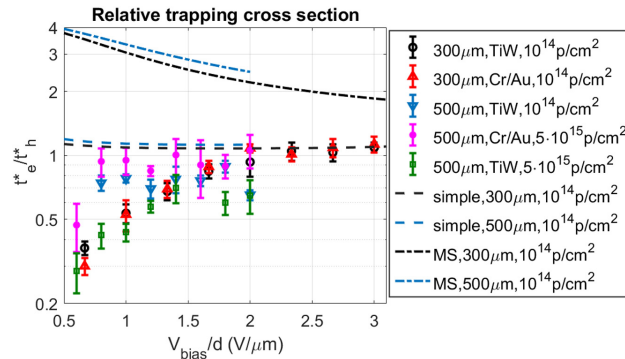


Fig. 9. Relation between polarization time for holes and electrons as a function of bias voltage normalized with detector thickness for irradiated diamonds. Measurement data is compared to model calculations with the simple and multiple scales (MS) computational models.

detector is expected to be operational for extended period of time before polarization occurs, especially, if high bias voltage is used.

For the high fluence ($5 \cdot 10^{14}$ p/cm²) detectors, switching high voltage off and back on is not enough to restore charge collection efficiency and alternative methods for improving detector performance, such as filling traps or re-processing, are advised to be considered in high particle rate environment.

There is need for development of numerical model to describe the polarization in diamond. The two models considered in this study are originally developed for other materials and do not take into account all the relevant aspects for diamond.

The models compared to the data are in better agreement with 500 μm than 300 μm thick detectors. This could indicate significant trapping at the diamond-metal interfaces.

Acknowledgements

Special thanks for the help provided by TOTEM collaboration, CMS-TOTEM Precision Proton Spectrometer community and the IRRAD-team. This project has received funding from the H2020 project AIDA-2020, GA no. 654168, Magnus Ehrnrooth Foundation, Svenska kulturfonden, Academy of Finland and Waldemar von Frenckell Foundation.

References

- [1] N. Venturi, A. Alexopoulos, M. Artuso, F. Bachmair, L. Bani, M. Bartosik, J. Beacham, H. Beck, V. Bellini, V. Belyaev, B. Bentele, P. Bergonzo, A. Bes, J.-M. Brom, M. Bruzzi, G. Chiodini, D. Chen, V. Cindro, G. Claus, J. Collot, J. Cumalat, A. Dabrowski, R. D'Alessandro, D. Dauvergne, W. de Boer, C. Dorfer, M. Dunser, V. Eremin, G. Forcolin, J. Forneris, L. Gallin-Martel, M.-L. Gallin-Martel, K. Gan, M. Gastal, C. Giroletti, M. Goffe, J. Goldstein, A. Golubev, A. Gorišek, E. Grigoriev, J. Grosse-Knetter, A. Grummer, B. Gul, M. Guthoff, I. Houghton, B. Hiti, D. Hits, M. Hoferkamp, T. Hofmann, J. Hosslet, J.-Y. Hostachy, F. Hügging, C. Hutton, J. Janssen, H. Kagan, K. Kanxheri, G. Kasieczka, R. Kass, F. Kassel, M. Kis, G. Kramberger, S. Kuleshov, A. Lacoste, S. Lagomarsino, A. L. Giudice, E. Lukosi, C. Maazouzi, I. Mandic, C. Mathieu, M. Menichelli, M. Mikuž, A. Morozzi, J. Moss, R. Mountain, S. Murphy, M. Muškinja, A. Oh, P. Olivero, D. Passeri, H. Pernegger, R. Perrino, F. Pic, Results on radiation tolerance of diamond detectors, Nuclear Instruments and Methods in Physics Research Section A: Accelerators, Spectrometers, Detectors and Associated Equipment doi: <https://doi.org/10.1016/j.nima.2018.08.038>, <http://www.sciencedirect.com/science/article/pii/S0168900218309914>.
- [2] G. Antchev, P. Aspell, I. Atanassov, V. Avati, J. Baechler, V. Berardi, M. Berretti, E. Bossini, U. Bottigli, M. Bozzo, P. Broulim, A. Buzzo, F. Cafagna, M. Catanesi, M. Csanád, T. Csörgő, M. Deile, F.D. Leonardi, A. D'Orazio, M. Doubek, K. Eggert, V. Eremin, F. Ferro, A. Fiergolski, F. Garcia, V. Georgiev, S. Giani, L. Grzanka, C. Guaragnella, J. Hammerbauer, J. Heino, A. Karev, J. Kašpar, J. Kopal, V. Kundrát, S. Lami, G. Latino, R. Lauhakangas, R. Linhart, M. Lokajíček, L. Losardo, M.L. Veteř, F.L. Rodríguez, D. Lucsanayi, M. Macrí, A. Mercadante, N. Minafra, S. Minutoli, T. Naaranoja, F. Nemes, H. Niewiadomski, T. Novak, E. Oliveri, F. Oljemark, M. Oriunno, K. Österberg, P. Palazzi, L. Paločko, V. Passaro, Z. Peroutka, V. Petruzzelli, T. Politi, J. Procházka, F. Prudenzano, M. Quinto, E. Radermacher, E. Radicioni, F. Ravotti, E. Robutti, C. Royon, G. Ruggiero, H. Saarikko, A. Scribano, J. Smajek, W. Snoeys, J. Sziklai, C. Taylor, N. Turini, V. Vacek, J. Welti, P. Wyzkowski, K. Zielinski, Diamond detectors for the TOTEM timing upgrade, Journal of Instrumentation 12 (03) (2017) P03007 <http://stacks.iop.org/1748-0221/12/i=03/a=P03007>.
- [3] CMS-TOTEM Precision Proton Spectrometer, Technical Report, CERN-LHCC-2014-021 TOTEM-TDR-003 CMS-TDR-13, (2014).
- [4] Timing Measurements in the Vertical Roman Pots of the TOTEM Experiment, Technical report, CERN-LHCC-2014-020 TOTEM-TDR-002, 2014.
- [5] F. Kassel, M. Guthoff, A. Dabrowski, W. de Boer, Severe signal loss in diamond beam loss monitors in high particle rate environments by charge trapping in radiation-induced defects, Phys. Status Solidi A 213 (10) (2016) 2641–2649, <https://doi.org/10.1002/pssa.201600185>.
- [6] M. Pomorski, E. Berdermann, W. de Boer, A. Furgeri, C. Sander, J. Morse, Charge transport properties of single crystal cvd-diamond particle detectors, Diam. Relat. Mater. 16 (4) (2007) 1066–1069, Proceedings of Diamond 2006, the 17th European Conference on Diamond, Diamond-Like Materials, Carbon Nanotubes, Nitrides and Silicon Carbide. doi: <https://doi.org/10.1016/j.diamond.2006.11.016>, <http://www.sciencedirect.com/science/article/pii/S0925963506004006>.
- [7] V. Griji, N. Skukan, M. Jakšić, M. Pomorski, W. Kada, T. Kamiya, T. Ohshima, The evaluation of radiation damage parameter for cvd diamond, Nucl. Instrum. Methods Phys. Res., Sect. B 372 (2016) 161–164. doi: <https://doi.org/10.1016/j.nimb.2015.12.046>, <http://www.sciencedirect.com/science/article/pii/S0168583X16000021>.
- [8] W. Kada, N. Iwamoto, T. Satoh, S. Onoda, V. Griji, N. Skukan, M. Koka, T. Ohshima, M. Jakšić, T. Kamiya, Continuous observation of polarization effects in thin sc-cvd diamond detector designed for heavy ion microbeam measurement, Nucl. Instrum. Methods Phys. Res., Sect. B 331 (2014) 113–116 11th European Conference on Accelerators in Applied Research and Technology <https://doi.org/10.1016/j.nimb.2013.11.040> <http://www.sciencedirect.com/science/article/pii/S0168583X14001347>.
- [9] Element Six Ltd., Kings Ride Park, Ascot, Berkshire SL5 8BP, UK, 2018 <https://www.e6.com>.
- [10] PRISM, Micro Fabrication Laboratory at Princeton Institute for the Science and Technology of Materials, <https://materials.princeton.edu>, (2018).
- [11] Applied Diamond Inc., 3825 Lancaster Pike, Wilmington, DE 19805, USA, 2018 <http://usapplieddiamond.com/>.
- [12] Irradiation dosimetry results 2017 (2018). <https://ps-irrad.web.cern.ch/assets/doc/after/results/2017/Sets-2017.html>.
- [13] W. Shockley, Currents to conductors induced by a moving point charge, J. Appl. Phys. 9 (10) (1938) 635–636, <https://doi.org/10.1063/1.1710367>.
- [14] S. Ramo, Currents induced by electron motion, Proc. IRE (1939) 584.
- [15] Synopsis, Synopsis webpage, <https://www.synopsys.com/>, accessed: January, 2018 (2018).
- [16] M. Breznanu, Diamond Schottky Barrier Diodes, Ph.D. thesis, 2007. <https://www.repository.cam.ac.uk/handle/1810/226757>.
- [17] A. Morozzi, Development and Application of State-of-the-Art Device/Circuit Level Tead Simulation Tools for the Optimization of Innovative Silicon-on-Diamond (Sod) Semiconductor Devices, Ph.D. thesis (2015/2016). http://www.infni.it/thesis/thesis_dettaglio.php?tid=12391.
- [18] T. Shimomura, Y. Kubo, J. Barjon, N. Tokuda, I. Akimoto, N. Naka, Quantitative relevance of substitutional impurities to carrier dynamics in diamond, Phys. Rev. Materials 2 (2018) 094601, <https://doi.org/10.1103/PhysRevMaterials.2.094601> <https://link.aps.org/doi/10.1103/PhysRevMaterials.2.094601>.
- [19] S. Dannefaer, A. Pu, D. Kerr, Positron annihilation study of vacancies in type IIA diamonds illuminated with monochromatic light, Diam. Relat. Mater. 10 (12)

- (2001) 2113–2117, [https://doi.org/10.1016/S0925-9635\(01\)00489-7](https://doi.org/10.1016/S0925-9635(01)00489-7) <http://www.sciencedirect.com/science/article/pii/S0925963501004897>.
- [20] M. Pomorski, Electronic Properties of Single Crystal Cvd Diamond and its Suitability for Particle Detection in Hadron Physics Experiments, Ph.D. thesis, 2008. http://www.norhdia.gsi.de/publications/pomorski_thesis_final_LQ.pdf.
- [21] C.E. Nebel, Electronic properties of cvd diamond, *Semicond. Sci. Technol.* 18 (3) (2003) S1 <http://stacks.iop.org/0268-1242/18/i=3/a=301>.
- [22] D.M. Caughey, R.E. Thomas, Carrier mobilities in silicon empirically related to doping and field, *Proc. IEEE* 55 (12) (1967) 2192–2193, <https://doi.org/10.1109/PROC.1967.6123>.
- [23] D.S. Bale, C. Szeles, Nature of polarization in wide-bandgap semiconductor detectors under high-flux irradiation: Application to semi-insulating $\text{cd}_{1-x}\text{zn}_x\text{Te}$, *Phys. Rev. B* 77 (2008) 035205, <https://doi.org/10.1103/PhysRevB.77.035205>.
- [24] M. Martini, T. McMath, Trapping and detrapping effects in lithium-drifted germanium and silicon detectors, *Nucl. Inst. Methods* 79 (2) (1970) 259–276, [https://doi.org/10.1016/0029-554X\(70\)90149-7](https://doi.org/10.1016/0029-554X(70)90149-7) <http://www.sciencedirect.com/science/article/pii/0029554X70901497>.

Publication II

Gädda, A., Ott, J., Karadzhinova-Ferrer, A., Golovleva, M., Kalliokoski, M., Winkler, A., Luukka, P., and Härkönen, J.

Cadmium Telluride X-ray pad detectors with different passivation dielectrics

Reprinted with permission from

Nuclear Instruments and Methods in Physics Research Section A: Accelerators, Spectrometers, Detectors and Associated Equipment

Vol. 924, pp. 33–37, 2019.

© 2018, Elsevier B.V.



Contents lists available at ScienceDirect

Nuclear Inst. and Methods in Physics Research, A

journal homepage: www.elsevier.com/locate/nima

Cadmium Telluride X-ray pad detectors with different passivation dielectrics

A. Gädda^{a,*}, J. Ott^a, A. Karadzhinova-Ferrer^b, M. Golovleva^{a,c}, M. Kalliokoski^b, A. Winkler^{a,d},
P. Luukka^a, J. Härkönen^b

^a Helsinki Institute of Physics, Gustaf Hällströmin katu 2, 00014 University of Helsinki, Finland

^b Ruder Bošković Institute, Bijenička cesta 54, 10000 Zagreb, Croatia

^c Lappeenranta University of Technology, Skinnarilankatu 34, 53850 Lappeenranta, Finland

^d Detection Technology Plc, Ahventie 4B, FI-02170 Espoo, Finland

ARTICLE INFO

Keywords:

Cadmium Telluride (CdTe)
Atomic layer deposition (ALD)
X-ray detector

ABSTRACT

The suitability of two low-temperature dielectric passivation layer processes for the fabrication of Cadmium Telluride (CdTe) X-ray detectors has been investigated. The CdTe crystals with a size of $(10 \times 10 \times 1) \text{ mm}^3$ were coated with sputtered aluminum nitride (AlN) or with aluminum oxide (Al_2O_3) grown by the atomic layer deposition (ALD) method. The metallization contacts of the detectors were made by titanium tungsten (TiW) and gold (Au) metal sputtering depositions. The pad detector structures were patterned with proximity-contactless photolithography techniques followed by lift-off patterning of the electrodes. The detector properties were characterized at room temperature by Transient Current Technique (TCT) measurements. The obtained results were compared and verified by numerical TCAD simulations of the detector response. Our results indicate that higher signal charge was collected from samples with Al_2O_3 . Furthermore, no significant laser light induced signal decay by CdTe material polarization was observed within order of 30 min of continuous illumination.

Contents

1. Introduction	33
2. Design and processing	34
3. Measurements	34
3.1. Transient Current Technique Measurement	34
3.2. Simulations	35
4. Conclusions and summary	36
Acknowledgments	36
References	36

1. Introduction

Photon detectors made of high atomic number (Z) semiconductor materials are utilized for a wide variety of applications, such as for spectroscopy of nuclear isotopes, or medical imaging [1,2]. Generally desired properties of such detector systems are good energy resolution ($\Delta E/E$) and an X-ray image quality that is as sharp as possible. One of the semiconductor materials that frequently used for room temperature spectroscopic applications is CdTe [3,4]. Its high effective atomic number $Z_{eff} = 50$ is essential for the good attenuation of up to several hundred keV of ionizing radiation, and the band gap of 1.44 eV allows low noise operation at room temperature.

Assuming an appropriate signal generation in a CdTe detector of certain thickness, a measure of spectroscopic or imaging performance is the Charge Collection Efficiency (CCE) [5,6]. The CCE is simply the ratio of electrical charge collected by electrodes divided by the amount of deposited charge. The charge transport in a semiconductor detector and CCE are often modeled by the well-known Hecht equation published in 1932 [7]. The Hecht equation implies that, in addition to geometrical parameters, charge transport in the electric field depends on the product of carrier mobility and trapping lifetime. Qualitatively, good CCE results in improved energy resolution and thus better image quality. The CCE is reduced by trapping/recombination of photon generated charge

* Corresponding author.

E-mail address: akiko.gadda@helsinki.fi (A. Gädda).

<https://doi.org/10.1016/j.nima.2018.08.063>

Received 20 February 2018; Received in revised form 22 July 2018; Accepted 20 August 2018

Available online 23 August 2018

0168-9002/© 2018 Elsevier B.V. All rights reserved.

carriers. Trapping/recombination processes take place inside of the active volume of a detector as well as at the front and back surfaces [8]. If the ratio of detector thickness (L) and drift velocity of charge carriers (v_{drift}) is larger than the charge lifetime ($\tau_{e,h}$), then the CCE will be degraded. The $\tau_{e,h}$ is inversely proportional to the concentration of the trapping centers, i.e. defects in the bulk of semiconductor. Due to the complex growth process of CdTe [9], the concentration of bulk defects (i.e. Te inclusion) is almost always very high. Typical values are around 3×10^6 inclusion/cm³ [10].

The carrier drift velocity is directly proportional to the product of the carrier mobility ($\mu_{e,h}$) and the local electric field ($E(x)$); however, saturation effects occur in CdTe at the field strength of > 100 V/cm for electrons ($\tau_e \approx 5-10$ μ s) [9,11] and several kV/cm for holes, due to the short $\tau_h \leq 1$ μ s of holes. Thus, high voltage operation of a CdTe detector is beneficial in order to reach saturation drift velocity of electrons. The electron mobility (μ_e) in CdTe is in the order of 1100 cm²/Vs, which is comparable with electron mobility e.g. in silicon [12]. The hole mobility (μ_h) in CdTe is in turn about an order of magnitude less than (88 cm²/Vs) [12]. This suggests that it is more favorable to collect a signal which is dominantly formed by electrons, since most of the holes are lost due to trapping in CdTe bulk [5,13]. Moreover, poor transport properties of holes in CdTe are known to cause a “hole tailing” effect, which results in an asymmetric broadening of peaks in measured spectra [6,14].

In order to minimize signal losses due to surface recombination processes, a proper field insulation layer on the CdTe detector surfaces is needed for the formation of the CdTe Schottky diode. This can be achieved by implementing a dielectric thin film on the surface. Dielectric thin films often have certain electrical charge, which is a complex combination of e.g. interface charge, mobile ionic charge and fixed oxide charge [8]. If the oxide charge is positive, then the Coulomb force is repulsing holes from the damaged surface, thus providing electrical passivation of hole current. In case of negative oxide charge, a similar field effect passivation is established for electrons. The electrical passivation is also needed in order to provide resistive insulation between the electrodes of a segmented detector, and furthermore, provide protection against environmental effects such as moisture, corrosion, mechanical damages, or ambient light that would induce additional noise.

The electrical passivation of CdTe by deposition of dielectric thin films is challenging due to thermal expansion properties of CdTe crystals, which limits the maximum processing temperature to about 150 °C [15,16]. It is also well-known that the electrical and mechanical quality of dielectric CVD films typically improve with respect to the increasing deposition temperature [17]. In this report two thin film passivation materials, aluminum nitride (AlN) and aluminum oxide (Al₂O₃), were studied. They were both deposited at a low temperature by using magnetron sputtering and Atomic Layer Deposition (ALD), respectively. The applied ALD method is based on the successive, separated, and self-terminating gas–solid reactions of typically two gaseous precursors and the deposition may take place at low temperature, compatible with CdTe detector processing [18,19]. Moreover, studies performed on silicon solar cells [20,21] and particle detectors [22,23] indicate that Al₂O₃ has a negative oxide charge, thus providing field effect passivation for electrons and allowing preferred signal formation mode for CdTe photon detectors. In this report, the passivation effects have been studied by Transient Current Technique (TCT) by recording current transients from laser illuminated CdTe pad detectors.

2. Design and processing

The starting material is detector grade ($> 10^9 \Omega \cdot \text{cm}$ bulk resistivity) and (111) oriented crystal dies that were obtained from Acrorad Ltd. [24]. Crystals sizes are (10×10) mm² and 1 mm in thickness. As shown in Fig. 1a, the chip layout contains a (5.5×5.5) mm² pad detector at the middle of the 1 cm² crystal front plane. It is surrounded by a single $200 \mu\text{m}$ wide guard ring. The gap between the pad and guard ring is

$50 \mu\text{m}$. At the center of the detector pad, there is a 2 mm diameter round metal opening area allowing for optical excitations. At the periphery of the detector pad (East and West direction) eight round 1 mm detector pads are located, which are intended for other studies.

The AlN passivation was deposited on both front and back surfaces of the CdTe crystals, hence the Al₂O₃ ALD process is by nature a conformal coating. Al₂O₃ was deposited at 120 °C in a Beneq TFS-500 batch-type ALD reactor, using trimethylaluminum (TMA) as the metal precursor and water as the oxidant. AlN was deposited in a MRC-903 sputtering tool using the mixture of Ar (200 sccm) and N₂ (505 sccm) gases under the deposition current condition of 10 A. Following dielectric deposition, the contact openings were created by wet etching for both passivation types. The fabrication process sequence is described in Ref. [25].

3. Measurements

3.1. Transient Current Technique Measurement

The Transient Current Technique (TCT) is a commonly adopted method to characterize semiconductor detectors. The TCT setup used in this study was constructed by Particulars d.o.o (Ljubljana, Slovenia) [26]. Optical excitation was performed with a red laser ($\lambda = 660$ nm) directed on the sensor front plane. The illumination generates a cloud of charge carriers within less than $1 \mu\text{m}$ depth from the detector surface. One type of charge carriers, either electrons or holes depending on the device structure, drifts only a few micrometers and is gathered to the electrode so quickly that the resulting signal is damped by the rise-time of the data acquisition electronics. Carriers of the other type drift through the entire thickness of the device resulting in transient current signal, which is detected by an oscilloscope.

In this case, the CdTe detectors were biased with positive high voltage from the back plane, so the TCT signal displays electrons drifting through the device, while the holes are immediately collected away at the front contact. This allowed us to study the electron dominated signal formation, which would be the preferred operation mode for segmented CdTe detectors as described above.

In addition to the red laser, the other components in the measurement setup were focusing optics, a sample holder mounted on a XYZ stage for scanning the entire surface of the detector, a 2 kV Bias-T (model BT-01), a wide band current amplifier (model AM-02) all by Particulars d.o.o., a Keithley 2410 1100 V Source Meter unit, a Tenna power supply, a LeCroy WaveRunner 8404M-MS 4 GHz oscilloscope and a PC and DAQ with MATLAB [27] based software. The laser pulse was transmitted to the detector by an optical fiber. A probehead needle was placed on the active area and a Cu plate connected the bias circuit to the front and back surfaces, respectively. The laser illumination was directed to the $50 \mu\text{m}$ gap between the pad and guard ring (see Fig. 2).

The current reading of the sourcing power supply was recorded during the measurements. As it can be seen in Figs. 3(a) and (b), the AlN-passivated detector could be biased only up to 160 V. The Al₂O₃ passivated detector, on the other hand, could be biased up to 500 V, while the current remained about three orders of magnitude smaller than for the AlN sample. Another notable feature when comparing these two detectors is the different pulse shapes. The AlN sample shows rather quick drop of the pulse amplitude, while the signals recorded from Al₂O₃ sample remain more flat over longer period of time indicating potentially longer carrier lifetimes. In both cases, the pulse duration is in the order of 80 ns as expected to be seen from 1 mm thick detectors.

Long signal decay times are known to be a problem in detectors made of highly defected materials such as CdTe [28,29]. The polarization in CdTe was studied by continuously illuminating the samples with different red laser pulse repetition rates for up to half an hour. An example of results is shown in Figs. 4(a) and (b).

The repetition rate of the laser is adjustable from 5 kHz to 500 kHz. During the measurements, more than one hundred waveforms were

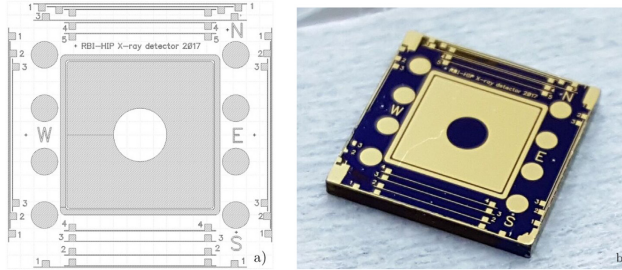


Fig. 1. (a) Layout of the CdTe pad detector. (b) Photograph of a processed detector chip

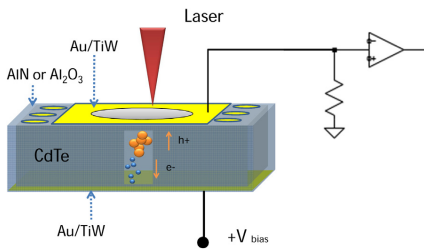


Fig. 2. Schematic cross section view of the detector package.

recorded both for the Al_2O_3 and the AlN passivated detectors. An illustrative presentation of the results is shown in Figs. 3(a) and (b).

It was observed that the signal (integral of current over the time) did not essentially change in the AlN-passivated sample (Fig. 4(a)). In the Al_2O_3 sample (Fig. 4(b)) providing generally stronger TCT signals, a decay in the order of about 20% could be observed. The signal decay was notably independent of optical excitation level from 5 to 500 kHz in range.

3.2. Simulations

In order to understand the experimental results, numerical simulations were performed using Synopsys Sentaurus Technology Computer-Aided Design (TCAD) [30] software. The simulated diode structure had dimensions $(100 \times 1000 \times 1) \mu\text{m}^3$ with a 50 nm thick AlN, or Al_2O_3 passivation layer. The material for the contacts on the front and backplanes was Ti. In the simulation, an n-type doped CdTe bulk with a uniform constant

doping concentration of $1 \times 10^{11} \text{ cm}^{-3}$ was considered. The diode was biased from the backplane contact. To reproduce the highly defected bulk of the diode, two mid-gap levels (a deep acceptor and a donor level) were implemented with energies 0.58 eV and 0.48 eV and concentration $1 \times 10^{12} \text{ cm}^{-3}$ and $1 \times 10^{15} \text{ cm}^{-3}$, respectively, and electron and hole capture cross sections $1 \times 10^{-13} \text{ cm}^2$ and $1 \times 10^{-14} \text{ cm}^2$. Furthermore, an additional interface trap at the CdTe/ Al_2O_3 interface was added as an acceptor level with the density of $1 \times 10^{12} \text{ cm}^{-3}$.

AlN deposition at low temperatures, such as 150°C without a post heat treatment results in a formation of positive fixed oxide charge, Q_f , at the interface [31]. Whereas, Al_2O_3 has a negative fixed oxide charge. Therefore, a positive and negative fixed oxide charges were used for AlN and Al_2O_3 , respectively, with the absolute value of Q_f equal to $1 \times 10^{12} \text{ cm}^{-3}$ each.

The TCT simulations were carried out using optical excitation induced by a laser with 660 nm wavelength and a Gaussian-shaped 1 ns pulse with sigma of 50 ps. The illumination was applied next to the front collecting contact. For the generation–recombination mechanism in the CdTe, the doping-dependent Shockley–Reed–Hall model (Scharfetter relation [30]) and impact ionization (van Overstraeten–de Man model [32]) were used. Fig. 5 shows a simulated current transients of AlN (a) and Al_2O_3 (b) passivated CdTe detectors. In simulations, 150 V bias voltage is assumed in both cases.

One can observe a sharply rising signal in the first part of transients. Unlike in simulations, which are based on ideal models, this part of transient is filtered out from experimental data since signal rise time is limited by time constants of electrical measurement circuit. Similar pulse shapes as shown Figs. 3(a) and (b) are, however, reproduced by numerical calculations, with the Al_2O_3 sample exhibiting a longer pulse duration and a larger signal than the AlN-passivated detector. The electron current transient results in a negative polarity signal, while hole current transient has a positive polarity. In the case of Fig. 5(b), it can be seen that for the first few nanoseconds the signal

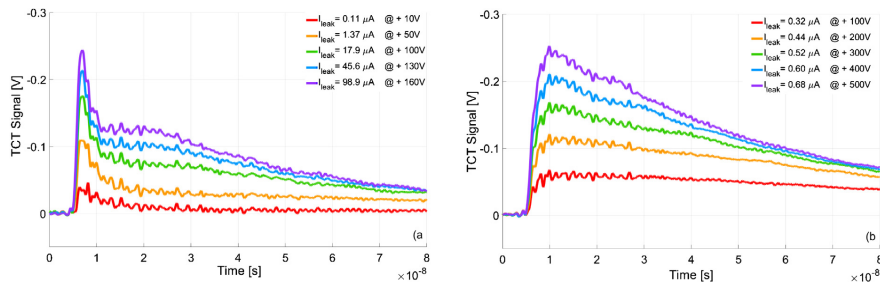


Fig. 3. Current transients of (a) AlN and (b) Al_2O_3 passivated CdTe detectors at different bias voltages. (Note: vertical scales are arbitrary units.)

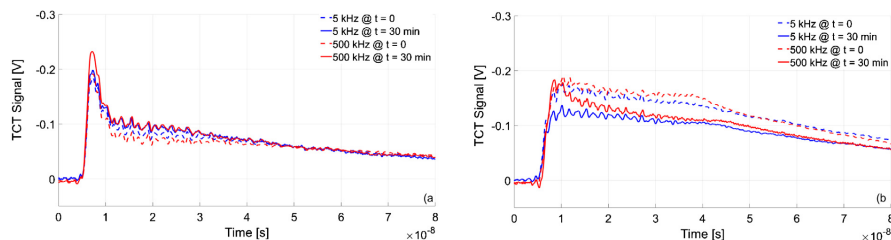


Fig. 4. Time evolution of current transients recorded at 5 kHz and 500 kHz laser repetition rates from (a) AlN and (b) Al₂O₃ passivated detector. (Note: vertical scales are arbitrary units.)

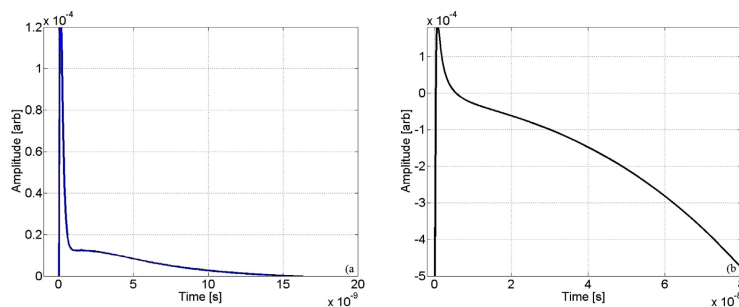


Fig. 5. Simulated current transients of (a) AlN and (b) Al₂O₃ passivated CdTe detectors.

consists of the hole carriers and as time progress it diminishes and electron current prevails. On the material level, transient pulse duration depends on various parameters, e.g. charge carrier lifetime, mobility, and inhomogeneities in bulk and interfaces. Therefore, we account the difference in transient time between simulation and experimental data towards the crystallographic imperfections that were not modeled, as well as the limited time constants of the read out circuit. On the other hand, the fast decreasing signal in case of AlN-passivated sensor is due to changes in electric field induced by positive fixed oxide charge.

4. Conclusions and summary

We produced CdTe detectors with different passivation layers: aluminum oxide (Al₂O₃) grown by Atomic Layer Deposition (ALD) method and sputtered aluminum nitride (AlN). The CCE of the detectors was studied by recording 660 nm wavelength laser induced current transients with a TCT measurement setup. During the measurement campaign more than one hundred waveforms were recorded in different areas of Al₂O₃ and AlN samples.

Our results systematically indicate longer pulse duration, i.e. higher CCE and longer charge carrier lifetime in Al₂O₃-passivated detectors than in ones passivated by the AlN. This is likely due to the negative oxide charge in ALD grown Al₂O₃ thin films. The negative charge repulses drifting electrons to be trapped/recombined at the heavily defected surfaces and thus resulting in higher CCE. This experimental observation is supported by numerical TCAD calculations, which reveal longer pulse duration if the oxide charge polarity of a field insulator is swapped from positive to negative and no change in polarization effect of CdTe was observed. These results coincide with our earlier studies made on CdTe pixel detectors fabricated by the same TiW/CdTe/TiW and Al₂O₃ passivation methodology. As reported in [25], we detected at room temperature a photopeak at 662 keV with about 2% energy resolution. Additionally, we observed about 20% relative signal decay when CdTe detectors were illuminated at different laser repetition rates,

i.e. different charge injection levels, for up to half an hour. While the laser repetition rate has influence onto the TCT signal amplitude, hence the amount of induced and trapped charges, no significant differences were observed for the polarization effect of the CdTe for either of the passivation methods. An operation of 30 min is a substantially longer time than what for instance patients would be exposed to by typical medical X-ray imaging devices. Thus, we are confident that Al₂O₃ grown at 120° C by ALD is a suitable method to provide electrical passivation for CdTe X-ray detectors.

Acknowledgments

This study has partially been funded by the Horizon 2020 ERA Chair project, grant agreement 669014 and by Academy of Finland project number 314473, “Multispectral photon-counting for medical imaging and beam characterization”. J. Ott acknowledges funding from the Viljo, Yrjö and Kalle Väisälä Foundation of the Finnish Academy of Science and Letters. Detector fabrication was performed in the cleanroom facilities of Micronova Nanofabrication Centre in Espoo, Finland. The authors are grateful to Dr. Eija Tuominen, coordinator of the Detector Laboratory at Helsinki Institute of Physics at the University of Helsinki Department of Physics, for providing the environment for electrical measurements.

References

- [1] G. Knoll, *Radiation Detection and Measurement*, fourth ed., John Wiley, Hoboken, N.J, ISBN: 978-0-470-13148-0, 2010.
- [2] W.A. Kalender, D. Kolditz, C. Steiding, V. Ruth, F. Lück, A.C. Rößler, E. Wenkel, Technical feasibility proof for high-resolution low-dose photon-counting CT of the breast, *Eur. Radiol.* (2016) 1–6.
- [3] P. Simon R Cherry, J.A. Sorenson, M.E. Phelps, *Physics in Nuclear Medicine*, fourth ed., ScienceDirect, sciencedirect.com, 2012.
- [4] A. Winkler, H. Koivunoro, V. Reijonen, I. Auterinen, S. Savolainen, Prompt gamma and neutron detection in BNCT utilizing a CdTe detector, *Appl. Radiat. Isot.* 106 (2015) 139–144, <http://dx.doi.org/10.1016/j.apradiso.2015.07.040>.

- [5] S. Del Sordo, L. Abbene, E. Caroli, A.M. Mancini, A. Zappettini, P. Ubertini, Progress in the development of CdTe and CdZnTe semiconductor radiation detectors for astrophysical and medical applications, *Sensors* 9 (2009) 3491–3526.
- [6] A.G. Kozorezov, J.K. Wigmore, A. Owens, R. den Hartog, A. Peacock, H. A Al-Jawhari, Resolution degradation of semiconductor detectors due to carrier trapping, *Nucl. Instrum. Methods Phys. Res. A* 546 (1–2) (2005) 209–212, <http://dx.doi.org/10.1016/j.nima.2005.03.026>.
- [7] K. Hecht, Zum Mechanismus des lichtelektrischen Primärstromes in isolierenden Kristallen, *Z. Phys.* 77 (3–4) (1932) 235–245.
- [8] S.M. Sze, K.K. Ng, *Physics of Semiconductor Devices*, Wiley, 2006.
- [9] S. Csaba, CdZnTe and CdTe materials for X-ray and gamma ray radiation detector applications, *Phys. Status Solidi b* 241 (3) (2004) 783–790, <http://dx.doi.org/10.1002/psb.200304296>.
- [10] A.E. Bolotnikov, N. Abdul-Jabber, S. Babalola, G.S. Camarda, Y. Cui, A. Hossain, E. Jackson, H. Jackson, J. James, K.T. Kohman, A. Luryi, R.B. James, Effects of Te inclusions on the performance of CdZnTe radiation detectors, in: 2007 IEEE Nuclear Science Symposium Conference Record, IEEE, 2009, pp. 1788–1797.
- [11] A. Cola, I. Farella, Electric field and current transport mechanisms in schottky cdte x-ray detectors under perturbing optical radiation, *Sensors* (ISSN: 1424-8220) 13 (7) (2013) 9414–9434, <http://dx.doi.org/10.3390/s130709414>, <http://www.mdpi.com/1424-8220/13/7/9414>.
- [12] K. Suzuki, S. Seto, T. Sawada, K. Imai, Carrier transport properties of HPB CdZnTe and THM CdTe:Cl, *IEEE Trans. Nucl. Sci.* 49 (2002) 1287–1291, <http://dx.doi.org/10.1109/TNS.2002.1039653>.
- [13] T. Takahashi, S. Watanabe, Recent progress in CdTe and CdZnTe detectors, *IEEE Trans. Nucl. Sci.* 48 (4) (2001) 950–959.
- [14] R.H. Redus, J.A. Pantazis, T.J. Pantazis, A.C. Huber, B.J. Cross, Characterization of CdTe detectors for quantitative X-ray spectroscopy, *IEEE Trans. Nucl. Sci.* (2009).
- [15] H. Heikkinen, A. Gädda, S. Vähänen, J. Salonen, P. Monnoyer, G. Blaj, L. Tiustos, M. Campbell, Low-temperature bump bonding of timepix readout chips and CdTe sensors at different sensor pitches, in: 2011 IEEE Nuclear Science Symposium Conference Record, 2011, pp. 4770–4775, <http://dx.doi.org/10.1109/NSSMIC.2011.6154712>.
- [16] R.N. Jacobs, J. Markunas, J. Pellegrino, L.A. Almeida, M. Groenert, M. Jaime-Vasquez, N. Mahadik, C. Andrews, S.B. Qadri, Role of thermal expansion matching in CdTe heteroepitaxy on highly lattice-mismatched substrates, *J. Cryst. Growth* 310 (12) (2008) 2960–2965, <http://dx.doi.org/10.1016/j.jcrysgro.2008.02.029>.
- [17] S. Sze, *Semiconductor Devices: Physics and Technology*, John Wiley & Sons Singapore Pte. Limited, ISBN: 9780470873670, 2012.
- [18] T. Suntola, Atomic layer epitaxy, *Mater. Sci. Rep.* 4 (5) (1989) 261–312.
- [19] M. Leskelä, M. Ritala, Atomic layer deposition (ALD): from precursors to thin film structures, *Thin Solid Films* 409 (1) (2002) 138–146, [http://dx.doi.org/10.1016/S0040-6090\(02\)00117-7](http://dx.doi.org/10.1016/S0040-6090(02)00117-7).
- [20] J.M. Sturm, A.I. Zinine, H. Wormeester, B. Poelsema, R.G. Bankras, J. Holleman, J. Schmitz, Imaging of oxide charges and contact potential difference fluctuations in atomic layer deposited Al₂O₃ on Si, *J. Appl. Phys.* 97 (6) (2005) 063709, <http://dx.doi.org/10.1063/1.1870113>.
- [21] P. Repo, H. Talvitie, S. Li, J. Skarp, H. Savin, Silicon surface passivation by Al₂O₃: Effect of ALD reactants, *Energy Procedia* 8 (2011) 681–687, <http://dx.doi.org/10.1016/j.egypro.2011.06.201>.
- [22] J. Härkönen, E. Tuovinen, P. Luukka, A. Gädda, T. Maenpää, E. Tuominen, T. Arsenovich, A. Junkes, X. Wu, Z. Li, Processing of n+/p-/p+ strip detectors with atomic layer deposition (ALD) grown Al₂O₃ field insulator on magnetic Czochralski silicon (MCz-si) substrates, *Nucl. Instrum. Methods Phys. Res. A* 828 (2016) 46–51, <http://dx.doi.org/10.1016/j.nima.2016.04.069>.
- [23] J. Härkönen, J. Ott, M. Mäkelä, T. Arsenovich, A. Gädda, T. Peltola, E. Tuovinen, P. Luukka, E. Tuominen, A. Junkes, J. Niinistö, M. Ritala, Atomic layer deposition (ALD) grown thin films for ultra-fine pitch pixel detectors, *Nucl. Instrum. Methods Phys. Res. A* 831 (2016) 2–6, <http://dx.doi.org/10.1016/j.nima.2016.03.037>.
- [24] Acrorad Ltd., Acrorad webpage, <https://www.acrorad.co.jp>. (Accessed January 2018).
- [25] A. Gädda, A. Winkler, J. Ott, J. Härkönen, A. Karadzhinova-Ferrer, A. Koponen, P. Luukka, J. Tikkanen, S. Vähänen, Advanced processing of CdTe pixel radiation detectors, *J. Instrum.* 12 (2017) <http://dx.doi.org/10.1088/1748-0221/12/12/C12031>.
- [26] Particulars, advanced measurement systems, <http://particulars.si/index.php>. (Accessed January 2018).
- [27] Mathworks Inc., Matlab webpage, <https://www.mathworks.com>. (Accessed January 2018).
- [28] A. Cola, I. Farella, The polarization mechanism in CdTe Schottky detectors, *Appl. Phys. Lett.* 94 (10) (2009) 102113, <http://dx.doi.org/10.1063/1.3099051>.
- [29] B. Dezillie, V. Eremin, Z. Li, E. Verbitskaya, Polarization of silicon detectors by minimum ionizing particles, *Nucl. Instrum. Methods Phys. Res. A* 452 (3) (2000) 440–453, [http://dx.doi.org/10.1016/S0168-9002\(00\)00450-2](http://dx.doi.org/10.1016/S0168-9002(00)00450-2).
- [30] Synopsys, Synopsys webpage, <https://www.synopsys.com>. (Accessed January 2018).
- [31] P. Repo, Reducing Surface Recombination in Black Silicon Photovoltaic Devices Using Atomic Layer Deposition (Ph.D thesis), Aalto University, Helsinki, Finland, ISBN: 978-952-60-6918-0, 2016, <http://urn.fi/URN:ISBN:978-952-60-6919-7>.
- [32] R. Van Overstraeten, H. De Man, Measurement of the ionization rates in diffused silicon p-n junctions, *Solid-State Electron.* 13 (5) (1970) 583–608.

Publication III

Golovleva, M., Bezak, M., Bharthuar, S., Brücken, E., Gädda, A., Härkönen, J.,
Kalliokoski, M., Kirschenmann, S., Luukka, P., Ott, J., and Tuuva, T.

**Modeling the impact of defects on the charge collection efficiency of a Cadmium
Telluride detector**

Reprinted with permission from

Journal of Instrumentation

Vol. 16, P08027, 2021.

© IOP Publishing Ltd and Sissa Medialab

Modeling the impact of defects on the charge collection efficiency of a Cadmium Telluride detector

M. Golovleva,^{a,b,*} M. Bezak,^{a,b} S. Bharthuar,^a E. Brücken,^a A. Gädda,^{a,c} J. Härkönen,^{a,e}
M. Kalliokoski,^{a,f} S. Kirschenmann,^a P. Luukka,^{a,b} J. Ott^{a,d} and T. Tuuva^b

^aHelsinki Institute of Physics,

Gustaf Hällströmin katu 2, FI-00014 University of Helsinki, Finland

^bLappeenranta University of Technology,

Skinnarilankatu 34, FI-53850 Lappeenranta, Finland

^cOkmetic Oy,

Piitie 2, FI-01510 Vantaa, Finland

^dAalto University, Department of Electronics and Nanoengineering,

Tietotie 3, FI-02150 Espoo, Finland

^eLudong University,

186 Hongqi W Rd, Zhifu District, Yantai, Shandong, China

^fRuder Bošković Institute,

Bijenička cesta 54, HR-10000 Zagreb, Croatia

E-mail: maria.golovleva@lut.fi

ABSTRACT: Cadmium telluride is a favorable material for X-ray detection as it has an outstanding characteristic for room temperature operation. It is a high-Z material with excellent photon radiation absorption properties. However, CdTe single crystals may include a large number of extended crystallographic defects, such as grain boundaries, twins, and tellurium (Te) inclusions, which can have an impact on detector performance. A Technology Computer Aided Design (TCAD) local defect model has been developed to investigate the effects of local defects on charge collection efficiency (CCE). We studied a 1 mm thick Schottky-type CdTe radiation detector with transient-current technique by using a red laser at room temperature. By raster scanning the detector surface we were able to study signal shaping within the bulk, and to locate surface defects by observing their impact on the CCE. In this paper we present our TCAD model with localized defect, and compare the simulation results to TCT measurements. In the model an inclusion with a diameter of 10 μm was assumed. The center of the defect was positioned at 6 μm distance from the surface. We show that the defect has a notable effect on current transients, which in turn affect the CCE of the CdTe detector. The simulated charge collection at the position of the defect decreases by 80 % in comparison to the defect-free case. The simulations show that the defects give a characteristic shape to TCT signal. This can further be used to detect defects in CdTe detectors and to estimate the overall defect density in the material.

KEYWORDS: Simulation methods and programs; Detection of defects; X-ray detectors

*Corresponding author.

Contents

1	Introduction	1
2	Materials and methods	2
2.1	TCAD simulations	2
2.2	TCT measurements	2
3	Results and discussion	4
3.1	Simulation results	4
3.2	Experimental results	9
4	Conclusions	11

1 Introduction

Cadmium Telluride (CdTe) is a suitable material for room temperature detection of X-ray and gamma-ray radiation. It has a relatively large band gap, 1.47 eV at 300 K, resulting in a small thermal noise. Another outstanding characteristic of this semiconductor material is its high atomic number that enables strong absorption and good detection efficiency for high-energy photons [1, 2].

At the same time, CdTe detectors suffer from the crystal impurities such as Te-inclusions, dislocation networks, and twin and subgrain boundaries [3], which affect the detector performance [4, 5]. Defects and impurities at the grain boundaries can trap charge carriers and also act as charge drains, which can be seen as fluctuations in the collected signal and charge collection efficiency (CCE) [6].

Laser Transient Current Technique (TCT) is a widely used and adopted method for the characterisation of semiconductor radiation detectors. TCT reveals many material characteristics of a detector, including defects and their influence on electric properties of the device [7, 8].

During a TCT measurement, a laser pulse generates charge carriers which pass through the detector in the applied electric field. With red laser TCT, electron-hole pairs (e - h pairs) are generated close to the surface of the illuminated side of the device. One type of the charge carriers is immediately collected by the nearest electrode. Thus, the induced current is an outcome of a single carrier type drift, depending on the bias voltage. The collected signal is rich on information about the detector: various parameters, such as rise time, charge collection efficiency (CCE), and peaking amplitude can be extracted from the signal. By mounting the setup on a XYZ-stage and by combining the signal output with the position information from the stage, the locations of the defects and other non-uniformities can be mapped, and their effect on the charge collection efficiency (CCE) can be studied [9].

In this paper, we studied the effects of defects in CdTe pad detectors by using red laser TCT. In order to identify the impact of defects on the transient currents, simulations of a CdTe diode structure with the defect inclusion has been performed. By combining measured results and TCAD simulations a detailed study of detector performance was obtained.

2 Materials and methods

2.1 TCAD simulations

To better understand the impact of the defects on the detector performance, simulations were made using a Technology Computer Aided Design (TCAD) package from Synopsys [10]. The TCAD package provides the ability to simulate 2D or 3D CdTe structures with various electrode geometries and uses a drift diffusion model to simulate the detector response. At each point of the model, the Poisson and the charge carrier continuity equations are solved and the electrostatic potential and the carrier concentrations are calculated.

The simulated diode structure had dimensions of $A \times 3000 \times 1000 \mu\text{m}^3$ with a 50 nm thick AlN passivation layer, where A is an area factor to match the dimensions of the real diode. The thicknesses of the gold contacts on the front and backplanes were 500 nm. A work function of 5 eV for Schottky-type contacts was assumed. In the simulation, CdTe bulk with a uniform charge carrier concentration of $1 \times 10^7 \text{ cm}^{-3}$ was used [11]. A bias voltage of -450 V from the backplane was utilised in the simulations and the front plane was set to ground. To consider the high defect concentrations in the CdTe bulk, two mid-gap levels (a deep acceptor and a donor level) were implemented with energies of 0.72 eV and with a concentration of $1 \times 10^{12} \text{ cm}^{-3}$ [12]. The electron and hole capture cross sections were found by fitting simulated transients to the measurement results.

As revealed by IR microscopy mid-sized Te inclusions are in 5–15 μm range [13, 14]. In the simulations, large-scale defects (grain boundaries, Te inclusions) in the detector bulk were reproduced by introducing a CdTe semiconductor material inclusion with high amount of traps into the detector body, as depicted in figure 1(b). This approach was used since the conventional method of introducing energy levels into the CdTe bulk bandgap does not provide any physical localization of the defects. Due to this, a circular shaped inclusion with a diameter of 10 μm was considered as a local defect imitation. For the trap levels in the inclusion material, the same two mid-gap levels (a deep acceptor and a donor level) were implemented with energies of 0.72 eV.

The laser excitation was applied to the front opening. For the generation-recombination mechanism of charge carriers in the CdTe, the doping-dependent Shockley-Read-Hall model (Scharfetter relation [10]) and impact ionization (van Overstraeten model [16]) were used in the simulation. The penetration depth of a red laser is about a few μm , so the red laser TCT signal displays holes drifting through the device, while electrons are immediately collected away by the front contact. The red laser current pulses can be described by the Ramo-Shockley theorem [17]:

$$I_{e,h}(t) = N_{e,h} \exp\left(\frac{-t}{\tau_{e,h}}\right) \vec{E}(\vec{r}) \vec{E}_w(\vec{r}), \quad (2.1)$$

where $N_{e,h}$ is effective doping concentration, \vec{r} the location of the charge, $\tau_{e,h}$ is effective carrier trapping time, $\vec{E}(\vec{r})$, the weighting field given by the electrode configuration in the detector [9]. To consider electric field variation near the surface, the laser beam was pointed at 3 different positions at the surface: the middle of the optical opening (0), the left and right edge of the opening (550 and -550).

2.2 TCT measurements

The CdTe pad detectors discussed in this paper represent a simple structure of a CdTe single crystal with metal electrodes on both sides. Prior to metallization, CdTe was passivated with aluminium

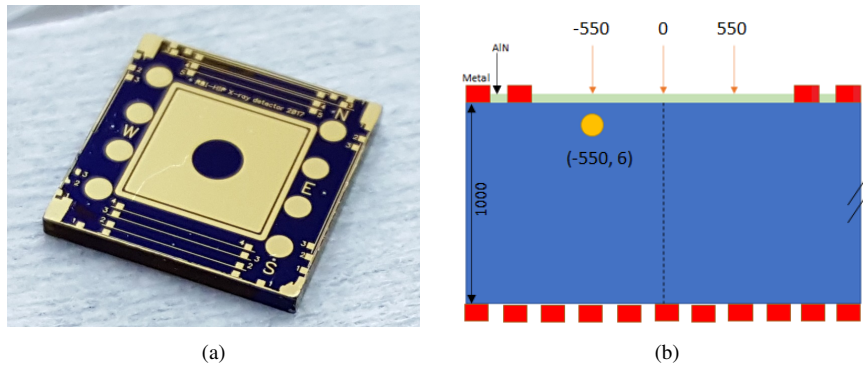


Figure 1. (a)¹ A pad detector with an optical opening in the middle [15] and (b) a schematic of the simulated structure with the optical opening and a defect inclusion. All the dimensions are in μm . Optical opening is from $-1000 \mu\text{m}$ to $1000 \mu\text{m}$ and the defect inclusion center position is $(-550, 6)$. The laser beam was pointed at 3 different positions at the surface: the middle of the opening (0), the left and right edge of the opening (-550 and 550).

nitride (AlN) [15, 18]. The contacts for both sides of CdTe detector were formed by sputtering depositions resulting in Schottky barrier contacts. They consist of a 20 nm thick titanium tungsten (TiW) adhesion layer, and around 200 nm thick layer of gold. For TCT measurements, there is an optical opening on the front side with a diameter of 2 mm without any metallization (figure 1(a)).

The TCT-setup consists of a pulsed laser source, optics with an adjustable diaphragm collimator, and a XYZ-stage. The detectors were mounted to the XY-plane of the system by pressing the front anode with a wire. The wire was also used as a contact for the detector bias. The backside of the detectors was grounded through the metal frame of the sample holder.

The bias voltage of $+450 \text{ V}$ was provided with a Keithley 2410 SourceMeter through a bias-T to the front contact. The voltage supply was also used to monitor, and to limit, the leakage current of the system. The output signal was passed through the bias-T to a Particulars AM-01 A 53 dB RF-amplifier. The resulting signal pulses were read out with a Teledyne Lecroy WaveRunner 840M-MS, 4 GHz, oscilloscope. The oscilloscope was operated in a sampling mode with a sampling frequency of 20 GS/s and a running average of 50 measurements, which was selected experimentally as a balance between noise suppression and response to changes in rise time. All measurements were made at room temperature.

A pulsed red-laser (wave length 660 nm, power 10 mW) with a Gaussian beam profile and pulse duration of 440 ps was used for $e-h$ pair creation. The repetition rate was set to 50 Hz and pulse power was cut to 60% of the maximum power, yielding pulse energy of about 4.4 pJ. The focal distance of the laser was set with a knife-edge technique [19].

In order to locate areas with non-uniformities, the optical opening of the detectors was raster scanned. From the TCT signals, values of amplitude, charge collection efficiency, peaking time, and rise time, were extracted and mapped in 2D maps using the coordinate information from the stages. From the maps, areas with defects were identified [20]. The CCE is defined as an integral over the

¹Reprinted from A. Gädda et al., *Cadmium Telluride X-ray pad detectors with different passivation dielectrics*, *Nucl. Instrum. Meth. A* **924** (2019) 33–37, Copyright (2019), with permission from Elsevier.

transient current signal with a time window of 900 ns. The resulting values are then normalized to the highest value in the measured area.

3 Results and discussion

3.1 Simulation results

In order to investigate the impact of the defect inclusion on the electrical field and the transient currents, a simulation of a reference diode detector with no bulk defects, no surface passivation layer on top of the optical opening and no incorporated defect inclusion was performed. This model is compared to the same structure with one defect inclusion inside.

In figure 2, the transverse distribution of the electrical field at the position of the defect is depicted for the abovementioned structure. The local defect introduction of a circular shape at the position of (-550, 6) gives us a fluctuation of the electric field due to charge accumulation as consequence of carrier trapping by the trap levels in the inclusion. In figure 2(a) one can see that the electric field starts increasing from the value of 1.7 kV/cm near the surface, while for the case without any defect, inclusion the value for the electric field near the surface is 2.1 kV/cm. Figure 2(b) shows that there is a disturbance of the electrical field at the position of the defect inclusion in the lateral distribution as well. This initial simulation indicates that the presence of a localised defect inclusion near the surface can cause fluctuations of the electric field, resulting in a change of the outcome signal.

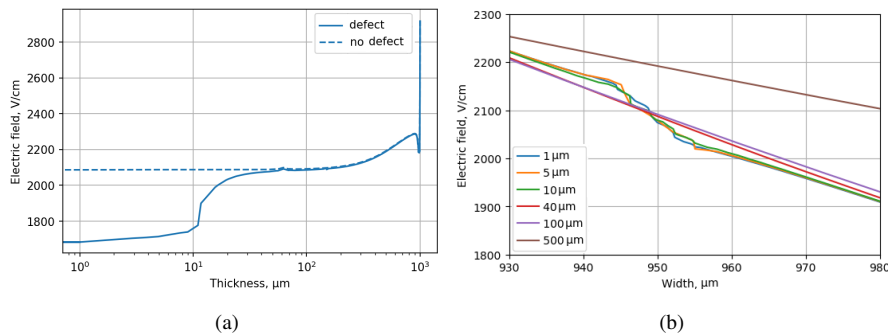


Figure 2. (a) Comparison of the simulated transverse distribution of the electrical field at the position of the defect for the simulated diode with and without defect incorporation. No bulk traps and no surface passivation were considered. (b) Simulated lateral electric field cuts with defect incorporated for different distances from the surface in μm in the proximity of the defect position.

The transient currents of the CdTe diode with and without defect are shown in figure 3. In the case of no inclusion, after generating $e - h$ pairs, fast electrons are collected on the front electrode in a short time that is demonstrated as a narrow peak, whereas slow holes travel long time through the sample to the back. When we are looking at the transient with the local defect, after the narrow peak produced by collected electrons the current rapidly decreases. In figure 3(b) the zoomed plot of the transient current is depicted. As the creation point of $e - h$ pairs is very close to the defect

area with a very high concentration of traps, part of the free carriers were captured by the trap levels in the inclusion. As it is shown in figure 3, the current for the case with the defect is by 2 orders of magnitude less than the signal without any inclusion.

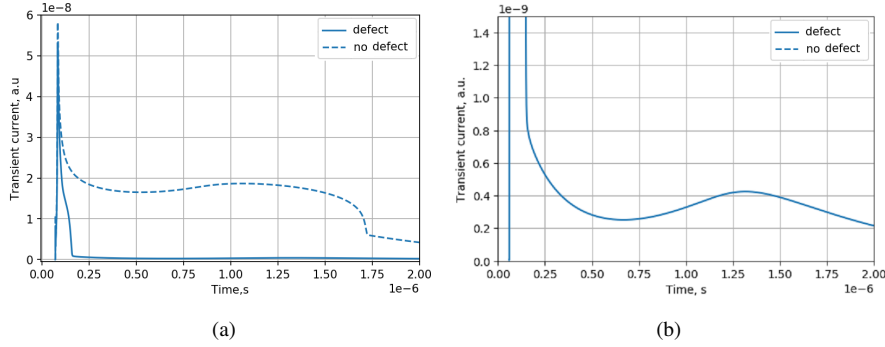


Figure 3. (a) Comparison of the simulated transient current at the position of the defect for simulated diode with and without defect incorporation. No bulk traps and no surface passivation were considered. (b) Zoom-in to the transient with defect inclusion.

In addition to bulk defects, surface recombination has a high impact on the device performance [21]. This can be reduced by passivating the surfaces of the crystal. To see how it affects the field strength, the AlN layer is added on top of the optical opening of the simulated structure. In figure 4(a), the transverse distribution of the electrical field is compared for two cases: passivation on top of the opening and no passivation. Since the bias is applied through the metallization, the strength of the electric field for the structure with no dielectric is the lowest in the middle of the optical opening (figure 4(a) green solid curve represents “no AlN” case). However, one can notice that with AlN deposited on top of the optical opening this effect is negligible (figure 4(a), green dashed curve represents AlN-passivated case). Figure 4(b) shows the lateral electric field profile of the simulated CdTe sensor with the defect inclusion and passivation layer along the optical opening for different distances from the surface. The field is uniform across the sample except for a local fluctuation of the field ascribed to the defect inclusion. For the field 1 μm below the surface the distribution reaches a peak at 4560 V/cm, then for 5 μm the peak height is decreasing, at 10 μm there is still some disturbance of the field and after 40 μm it becomes uniform. Also the electric field strength is almost two times higher for the detector with a dielectric on top of the optical opening. In the simulation, a positive fixed oxide charge was used with the absolute value of Q_f equal to $1 \times 10^{12} \text{ cm}^{-2}$. With the AlN layer on top of the optical opening, the potential difference increases and the strength of the electric field changes to a higher value. In figure 5, a simulated transverse field distribution as well as corresponding transient currents are shown for different oxide charge values. It can be noticed that with the higher value of the interface oxide charge, the electric field strength has a higher value. For the corresponding current signals the higher value of the interface oxide charge gives a lower value of the amplitude of the signal.

The waveforms corresponding to electric fields with and without passivation in figure 4(a) are shown in figure 6. When there is no AlN film on top of the optical opening, the electric field is small enough that the signal duration is much longer than 1 μs . At the center of the opening without AlN

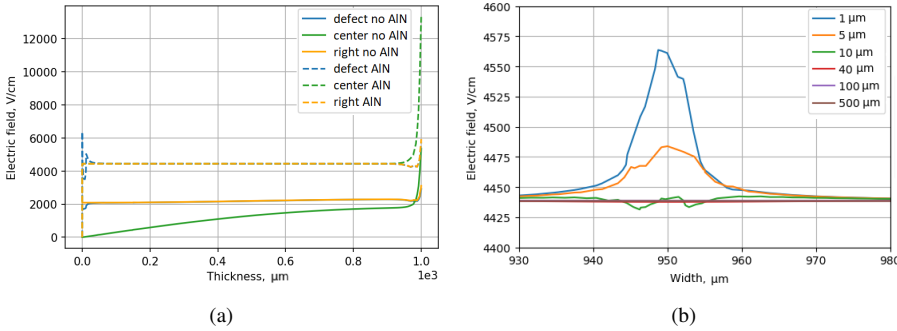


Figure 4. (a) Simulated transverse distribution of electrical field for the diode with the defect inclusion, no bulk traps and with and without passivation on top of the optical opening and (b) lateral electric field cuts with AlN on top of the optical opening for different distances from the surface in μm in the proximity of the defect position.

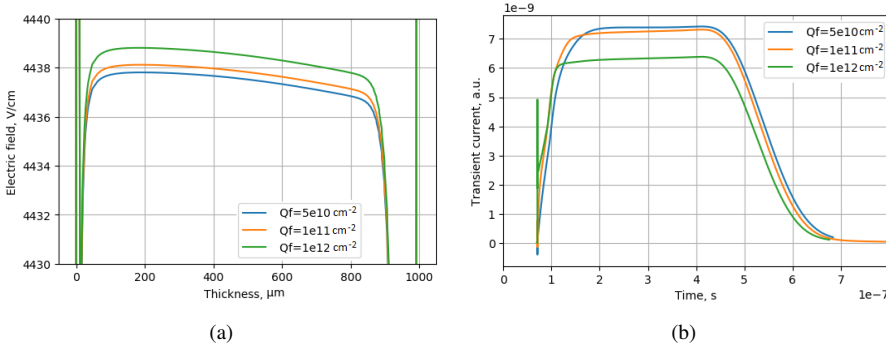


Figure 5. (a) Simulated transverse electric field distribution and (b) corresponding transient current at the position of defect inclusion with AlN on top of the optical opening for different oxide charges Q_f .

film, the electric field near the surface is zero, so the charge carrier drift velocity slows in the low potential region and the signal evolves very slow. We see only the beginning of the signal with very low amplitude. On the right side of the opening, the current reproduces the signal with no defect in the figure 3(a). The electric field strength at the center of the optical opening with the dielectric on top is almost the same as for the right side of the device, therefore the transient currents are identical as well. Comparing two transient signals at the position of the defect inclusion with and without passivation layer in figure 6, one can notice that the resulting current duration is 600 ns with the AlN deposited, while for the case without dielectric on the optical opening, the signal is longer than 1000 ns. The narrow peak in the beginning of the signal disappears with the passivation with the positive fixed charge, as the electric field strength increases, the electron drift velocity increased as well and the electrons are collected by the contact right away. It should be pointed out, that the shape of the signal with the defect inclusion and AlN on top of the opening has a characteristic form at the defect position, which can be easily identified from the surroundings.

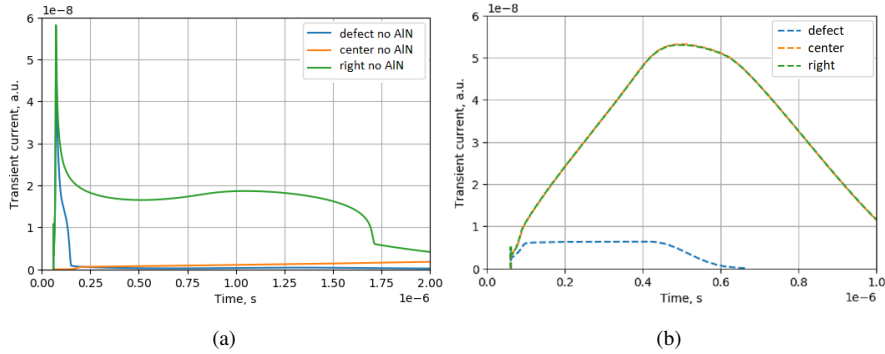


Figure 6. (a) Simulated transient current for simulated diode with the defect inclusion, no surface passivation and no bulk traps. (b) Simulated transient current for simulated diode with the defect inclusion, surface passivation and no bulk traps.

Finally, the bulk trap levels were implemented as to take into account the highly defected CdTe bulk material. In order to reproduce the measured double peak electric field distribution, a new defect model was created. In the upper half of the structure, the acceptor trap level was introduced with the energy 0.72 eV from conduction band and electron and hole capture cross section $\sigma_{e,h} = 2 \times 10^{-13} \text{ cm}^2$. For the bottom half of the created diode, the donor level was implemented with the same energy level and electron and hole capture cross section of $\sigma_{e,h} = 1 \times 10^{-16} \text{ cm}^2$. The acceptor and donor concentration of $1 \times 10^{12} \text{ cm}^{-3}$ was used. The electric field distributions of the abovementioned structure are shown in figure 7(a). In figure 7(b) the simulated transients are plotted. One can notice that the electric field shape reproduced by the waveforms and the transient signal amplitude at the position of the defect inclusion is around 4 times smaller than the signal at other positions of the device.

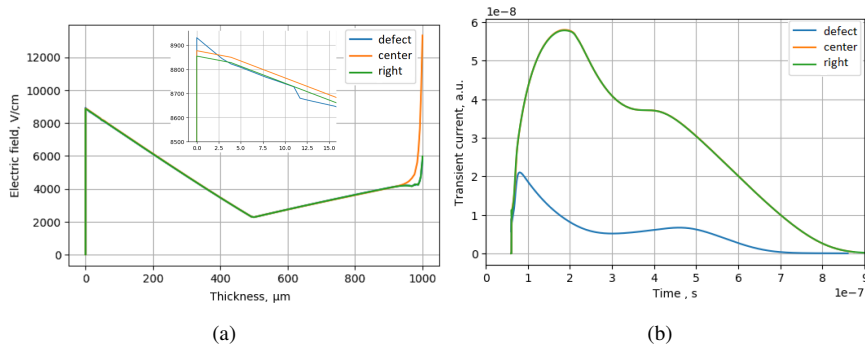


Figure 7. (a) Simulated transverse electric field distribution for the diode with the defect inclusion, bulk traps and passivation layer and (b) corresponding transient currents.

In a real CdTe crystal, there are different types of defect complexes that can be spread all over the bulk of the device [22], but in the simulation we used only one defect inclusion to see its effect

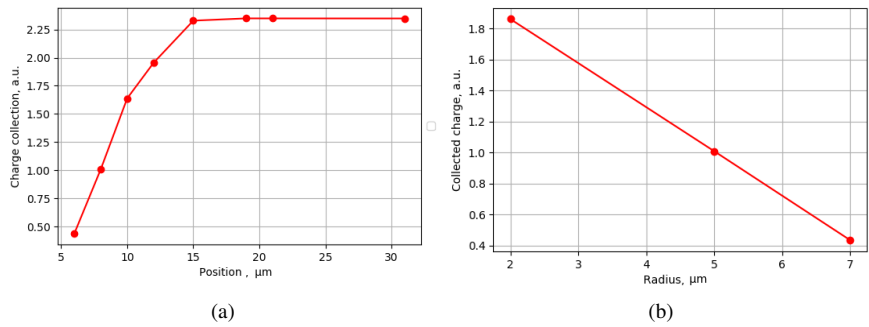


Figure 8. Simulated charge collection for different (a) defect positions with the radius 5 μm and (b) different defect radius of the inclusion with the defect position of 8 μm below the surface. The beam diameter is 10 μm for both cases.

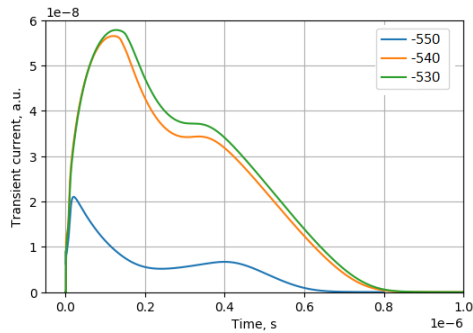


Figure 9. Simulated transient currents for the laser pointed at 3 different points at the optical opening where -550 is at the center of the defect.

on the waveforms. As an illustration of the dependence of the position and radius of the defect, figure 8(a) shows charge collection for different defect positions. The closer the defect inclusion is located to the diode surface, the higher is the impact of it on the red laser induced transient current. After around 19 μm from the surface there is no impact of the defect to the charge collection. In figure 8(b) the effect of the defect diameter is depicted. In this simulation, the defect inclusion is placed at 8 μm below the surface and the defect radius is varied. It is shown that for the smaller sized defect, a larger fraction of charge carriers reaches the diode backplane and thus the influence of the defect on the CCE is less. All the above transient current simulations were performed at the center position of the inclusion. However, if the laser beam was directed on the optical opening a bit shifted related to the defect center, the shape of the signal changes as well, as can be seen in figure 9. The closer the creation point of the charge carries is to the center of the defect, the more impact it has on the waveform.

3.2 Experimental results

By raster scanning the area of the opening in the horizontal direction, the uniformity of the detector is analyzed. The resulting plot of the CCE in the optical opening is presented in figure 10(a). In the plot, the CCE is normalized to the maximum value in the area. The fact that there is a passivation layer deposited in our sample can be an explanation why there is no minimum of charge collection in CCE map. From figure 10(b) we can also see that in the low-CCE region, the drift velocity is also lower than on the upper half of the opening. This could be resulting from trapping and de-trapping of the carriers [23].

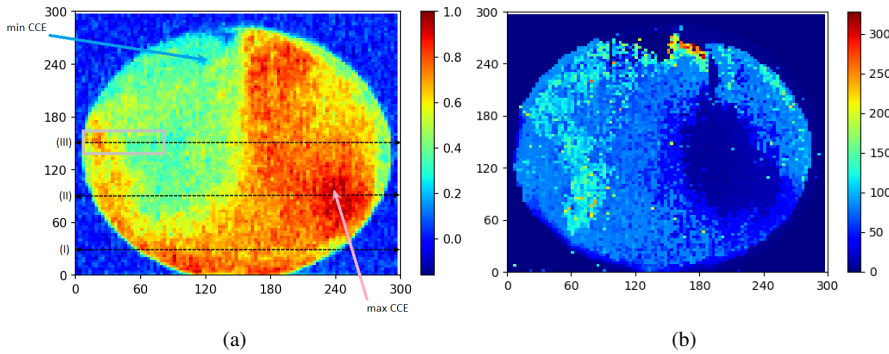


Figure 10. (a) TCT area scan and (b) the corresponding signal rise time at the optical opening of the CdTe detector at 660 nm. The area marked with a rectangle in (a) is discussed later in the paper.

The shape of the signals in the point with maximum and minimum CCE shown with the arrows in figure 10(a) and at the center of the optical opening are depicted in figure 11. The signal has a peak in the beginning and a long tail of the distributions that is produced both by the trapping-detrapping effects, and by the holes drifting to the sensor back-plane. The transient signal ends within 600 ns for the point with the lowest CCE, while the transient duration for the highest CCE is around 900 ns. The transient signal has a double peak shape [24]. Since the current is induced by charge moving in an electrical field, the shape of the signal is directly proportional to the electric field inside the sensor. The double peak signal gives us an evidence of the double peak electric field distribution through the bulk due to space charge build up at the contacts, probably in consequence of strongly trapped carriers in deep levels in the material [25].

In figure 12, the TCT signal cuts obtained from the oscilloscope at three different horizontal positions I, II and III of the TCT area scan map are depicted. These three horizontal cuts are shown in figure 10 with dashed lines and labeled. Each pixel represents a transient current amplitude where the x axis is a vertical position of the optical opening and y axis is a time of the waveforms. One can notice that from around 200 ns to 400 ns, the current signal has its minimum. For the TCT signal cut at a horizontal position I, where we see a uniform distribution of charge collection in the CCE map, the waveform durations are almost equal comparing to the other cuts. Likewise there is a minimum of the signal height almost at the middle of the transient duration. For the cuts at the center of the optical opening line III and at the position II, the signal length is much more scattered and the minimum is more pronounced. The longer signal could be associated with a smaller value

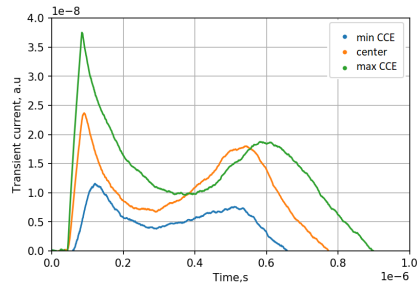


Figure 11. Transient currents for the point with maximum and minimum CEE shown with the arrows in figure 10(a) and at the centre of the optical opening .

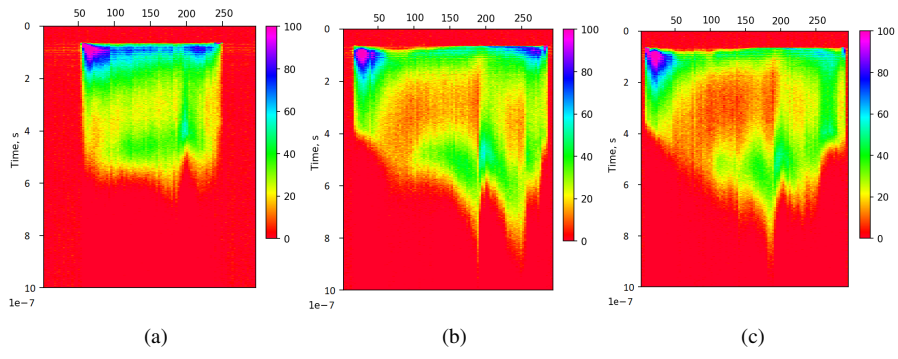


Figure 12. Transient current cuts at the I, II, and III horizontal position of the optical opening shown with dashed line in figure 10(a).

of electric field at this point. In contrary the shorter transient can indicate a higher field, or more likely a presence of some defect that can trap charge carries or act as charge drains, again leading to charge loss.

Figure 13(a) shows a closeup of the rectangular area marked in figure 10(a). In figure 13(b) the measured transient currents at two points, with higher and lower CCE, from this area are depicted. The simulated signals are plotted with dashed lines. One can notice that the transient signal for the point B with the minimum CCE is well reproduced by the simulation with the defect inclusion. However, the simulated currents at the position A where the higher charge collection has occurred, the simulation without any defect does not reproduce the measurement results precisely. This can be explained by the fact that in a real CdTe crystal, there are different types of defect complexes and they can be spread all over the bulk of the device. The simulation model with one defect works well in areas with a high concentration of defects, but may not be fully representative for such areas where defects are more sparse. Nonetheless, simulations demonstrate the ability of the transient current technique to be used in distinguishing between areas with high and low concentration of defects.

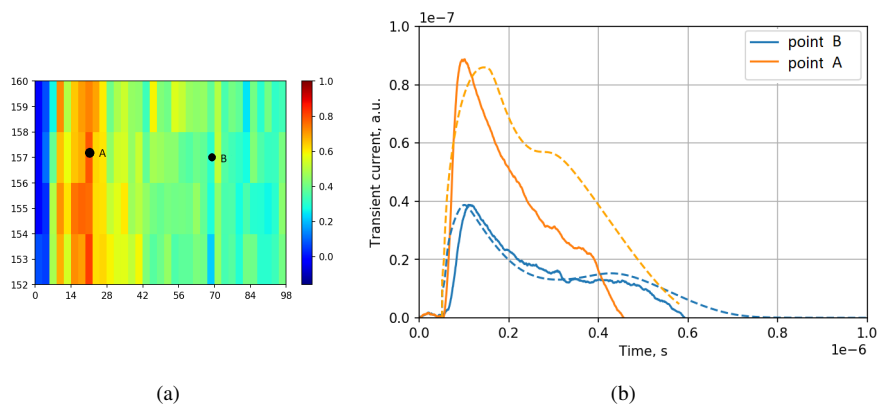


Figure 13. (a) Zoomed part of the CCE map marked with rectangle in figure 10(a). (b) Simulated (dashed) and measured (solid) transient currents at the points A and B of the optical opening of the CdTe detector.

4 Conclusions

TCAD simulations are a powerful tool in aiding semiconductor detector design and understanding complex physical problems. Numerical simulations were used to create a model of a local bulk defect to better understand the effect of it on the transient current. This model shows that the presence of the local defect leads to a reduction in charge collection efficiency. Depending on the defect inclusion size, position and the position of the laser beam pointed on the surface of the optical opening, the transient current have different shapes. Defect inclusions that are closer to the surface and have a bigger diameter, if the trap level energies, trap concentration and electron and hole capture cross sections are unchanged, have a higher impact to the charge collection by red laser TCT. Shifted laser beam position from the center of the defect result in the fluctuations of the signal form as well. The surface passivation, especially the fixed oxide charge value, plays an important role in electric field formation and should be taken into account while designing the detector.

Simulation adds an evidence to the conclusion that the transient current has a characteristic shape at a defect position, which can be clearly distinguished from the surroundings using transient current technique. We were able to reproduce the measurement results adequately with a simple simulation model with one defect inclusion.

CdTe has a large amount of extended crystallographic defects that deteriorate the device performance. It is crucial to evaluate the quality of the material. A combination of the simulations, TCT and three-dimensional (3D) infrared microscopy (IRM) would show the impact of the localised defect of the raw material on the performance of the processed detector.

All measurements that were shown in this paper were made by using only one bias level, and at room temperature. Further studies will involve, among others, analysis of effects of bias level, impact of temperature variation, and changes in laser parameters.

Publication IV

Bharthuar, S., Golovleva, M., Bezak, M., Brücken, E., Gädda, A., Härkönen, J.,
Karadzhinova-Ferrer, A., Kramarenko, N., Kirschenmann, S., Luukka, P., Mizohata, K.,
Ott, J., and Tuominen, E.

**Characterization of Heavily Irradiated Dielectrics for Pixel Sensors Coupling
Insulator Applications**

Reprinted with permission from
Frontiers in Materials
Vol. 8, 769947, 2022.
© 2022, Frontiers



Characterization of Heavily Irradiated Dielectrics for Pixel Sensors Coupling Insulator Applications

S. Bharthuar^{1,2*}, M. Golovleva^{1,3}, M. Bezak^{1,3}, E. Brücken¹, A. Gädda^{1,4}, J. Härkönen^{1,5}, A. Karadzhinova-Ferrer^{1,5}, N. Kramarenko^{1,3}, S. Kirschenmann^{1,2}, P. Koponen¹, P. Luukka^{1,3}, K. Mizohata², J. Ott^{1,6} and E. Tuominen^{1,2}

¹Helsinki Institute of Physics, Helsinki, Finland, ²Department of Physics, University of Helsinki, Helsinki, Finland, ³Lappeenranta-Lahti University of Technology, Lappeenranta, Finland, ⁴Okmetic Oy., Vantaa, Finland, ⁵Ludong University, Yantai, China, ⁶Aalto University, Department of Electronics and Nanoengineering, Espoo, Finland

OPEN ACCESS

Edited by:

Wenzhuo Wu,
Purdue University, United States

Reviewed by:

Dana Weinstein,
Purdue University, United States
Jackson Anderson,
Purdue University, United States, in
collaboration with reviewer DW
Sharaf Sumaiya,
Intel, United States

*Correspondence:

S. Bharthuar
shudhashil.bharthuar@helsinki.fi

Specialty section:

This article was submitted to
Semiconducting Materials and
Devices,
a section of the journal
Frontiers in Materials

Received: 02 September 2021

Accepted: 16 December 2021

Published: 19 January 2022

Citation:

Bharthuar S, Golovleva M, Bezak M, Brücken E, Gädda A, Härkönen J, Karadzhinova-Ferrer A, Kramarenko N, Kirschenmann S, Koponen P, Luukka P, Mizohata K, Ott J and Tuominen E (2022) Characterization of Heavily Irradiated Dielectrics for Pixel Sensors Coupling Insulator Applications. *Front. Mater.* 8:769947. doi: 10.3389/fmats.2021.769947

An increase in the radiation levels during the high-luminosity operation of the Large Hadron Collider calls for the development of silicon-based pixel detectors that are used for particle tracking and vertex reconstruction. Unlike the conventionally used conductively coupled (DC-coupled) detectors that are prone to an increment in leakage currents due to radiation, capacitively coupled (AC-coupled) detectors are anticipated to be in operation in future collider experiments suitable for tracking purposes. The implementation of AC-coupling to micro-scale pixel sensor areas enables one to provide an enhanced isolation of radiation-induced leakage currents. The motivation of this study is the development of new generation capacitively coupled (AC-coupled) pixel sensors with coupling insulators having good dielectric strength and radiation hardness simultaneously. The AC-coupling insulator thin films were aluminum oxide (Al₂O₃) and hafnium oxide (HfO₂) grown by the atomic layer deposition (ALD) method. A comparison study was performed based on the dielectric material used in MOS, MOSFET, and AC-coupled pixel prototypes processed on high resistivity p-type Magnetic Czochralski silicon (MCz-Si) substrates. Post-irradiation studies with 10 MeV protons up to a fluence of 10¹⁵ protons/cm² suggest HfO₂ to be a better candidate as it provides higher sensitivity with negative charge accumulation on irradiation. Furthermore, even though the nature of the dielectric does not affect the electric field within the AC-coupled pixel sensor, samples with HfO₂ are comparatively less susceptible to undergo an early breakdown due to irradiation. Edge-transient current technique (e-TCT) measurements show a prominent double-junction effect as expected in heavily irradiated p-type detectors, in accordance with the simulation studies.

Keywords: AC-pixel sensors, MOS capacitor, MOSFET, radiation hardness, alumina, hafnia, ALD (atomic layer deposition), magnetic Czochralski

1 INTRODUCTION

The Phase-2 Upgrade of the LHC to high-luminosity LHC (HL-LHC) in 2027 is expected to increase the instantaneous luminosity by a factor of 5–7, along with a goal of delivering an increase in the integrated luminosity from 400 fb⁻¹ to 3000–4,000 fb⁻¹ (an increase of a factor of ten compared to the expected dataset at that time). During the operation, silicon detector layers within the inner

tracker of the CMS experiment will be exposed to increased radiation doses up to $2.3 \times 10^{16} \text{ n}_{\text{eq}}/\text{cm}^2$ (Orfanelli, 2020).

Radiation induced damage within the silicon bulk of the detector leads to trapping of charge carriers, thereby decreasing the charge collection efficiency (CCE) of the detector. However, the detector efficiency can be improved by optimizing the pixel pitch size proportionate to the charge collection length of the detector. Simultaneously, such finely segmented pixel structures provide better position resolution by increasing the granularity of the detector. The CCE of the detector can be improved by reading the signal out due to electrons collected into the n^+ -implants on p-type silicon as they possess a higher mobility than holes that are collected into the traditional p^+ -implants on n-type silicon. This consequently has led to the use of silicon detectors with p-type bulk with segmented n^+ -implants, unlike the traditionally used n-type bulk with segmented p^+ -implants. However, with the use of silicon dioxide, characteristically a positive oxide charge, the dielectric layer results in surface electron accumulation near the interface of the insulating layer and the p-bulk. This would lead to the formation of a short circuiting channel between the n^+ -segments, thereby degrading the spatial resolution of the detector. Thus, in order to mitigate this issue, a p-stop or p-spray is usually added to electrically isolate the pixelated segments (Pellegriani et al., 2007). However, this requires additional implantation processing steps which subject the silicon wafers to high temperature and increases the mask levels that reduce the cost-effectiveness of the finally processed detectors.

Alternatively, the segmented implants can be electrically discrete from one another by utilizing thin films of a field insulator with negative oxide charge, such as hafnium oxide (HfO_2) and aluminum oxide (Al_2O_3), for an improved surface current termination strategy. Both Al_2O_3 and HfO_2 have a high negative oxide charge of the order of 10^{11} – 10^{13} cm^{-2} and possess very good dielectric constants, thereby yielding a higher oxide capacitance (Härkönen et al., 2016a,b).

Thin films of these insulating layers are grown by the atomic layer deposition (ALD) technique. The ALD technique requires low temperatures within 200–300°C and is beneficial in providing very conformal thin films (of tens of nm) with uniform thickness and good accuracy (Suntola, 1992; Leskelä, 2002). ALD HfO_2 films are widely used in the contemporary semiconductor industry, specifically for non-volatile memory chips like in portable flash memory storage devices and complementary metal-oxide-semiconductor (CMOS) chips in computers (Müller et al., 2014).

The following study focuses on a comparison of ALD-grown Al_2O_3 and Al_2O_3 along with HfO_2 ($\text{Al}_2\text{O}_3 + \text{HfO}_2$) as a field insulator implemented in metal-oxide-semiconductor (MOS) capacitors and field-effect-transistors (MOSFETs) as well as study the robustness in capacitive coupling for $n^+/p^-/p^+$ pixel detectors, on proton irradiation. An additional layer of HfO_2 is incorporated as it possesses a high dielectric constant of a magnitude of 25 (almost 3 times higher than that of Al_2O_3). This in turn provides a higher capacitive coupling along with a

better insulation and improved radiation hardness (Tsui et al., 2013).

2 MEASURED DEVICE SPECIFICATIONS

The detector fabrication was carried out in the facilities of the Micronova Nanofabrication Centre, Finland's national research infrastructure for micro- and nanotechnology. The devices were processed on 6-inch boron-doped magnetic Czochralski (MCz) silicon wafers provided by Okmetic Oyj. The wafers have a thickness of 320 μm and resistivity in the range of 4–8 $\text{k}\Omega\text{-cm}$. The ion implantation was carried out in an Eaton 8RPP ion implanter, implanting the front side with 60 keV phosphorous ions to target total doses of $1 \times 10^{15} \text{ cm}^{-2}$. The Al_2O_3 thin films were patterned for finely segmented structures by traditional wet etching, while HfO_2 was patterned by chemical mechanical polishing (CMP) into deep reactive ion etching (DRIE) defined structures.

The main samples that were characterized for this study, as shown in **Figure 1**, are as follows:

- MOS capacitors where the diameter of the gate is 1.5 mm.
- Circular MOSFETs with a channel width of 250 μm . The source and drains have heavily doped n^+ -implants where the doping concentration is of a maximum value of $1 \times 10^{19} \text{ cm}^{-3}$. The width of the annular source and the diameter of the circular drain is 200 μm and 400 μm , respectively.
- Pad diodes with standard prototype where the active area of the pad is $7.2 \times 7.2 \text{ mm}^2$.
- AC-coupled pixel sensors similar to the PSI46dig design consisting of 52×80 pixel matrix, along with a pitch size of $150 \times 100 \mu\text{m}$ (Gray, 2013).

Detailed information behind the processing of the MOS devices and detectors has been provided in articles—Ott et al. (2020); Gädde et al. (2021); Härkönen et al. (2021); Ott et al. (2021). Each of the abovementioned samples have either Al_2O_3 or $\text{Al}_2\text{O}_3 + \text{HfO}_2$ to permit better capacitive coupling. In addition to an improved capacitive coupling layer of individual pixels, thin films of TiN were used as bias resistors in the AC-pixel sensors, as shown in **Figure 1E**.

The actual thickness of the insulating layer for devices with Al_2O_3 is 84 nm. On the other hand, the samples employed with $\text{Al}_2\text{O}_3 + \text{HfO}_2$ as a dielectric layer were of a thickness of 84 and 63 nm, respectively. Since the dielectric constant of HfO_2 is almost three times higher than that of Al_2O_3 , the equivalent oxide thickness (defined as the thickness of silicon oxide film that provides the same electrical performance as that of a high dielectric constant material being used) of a composite dielectric system consisting of Al_2O_3 and HfO_2 with thicknesses of 84 and 62 nm, respectively, is reduced by $\sim 33 \text{ nm}$ as compared to 146 nm thick Al_2O_3 . This enables one to achieve similar oxide capacitance values (as can be observed in Section 4.1.1) and simultaneously increase the insulation resistance.

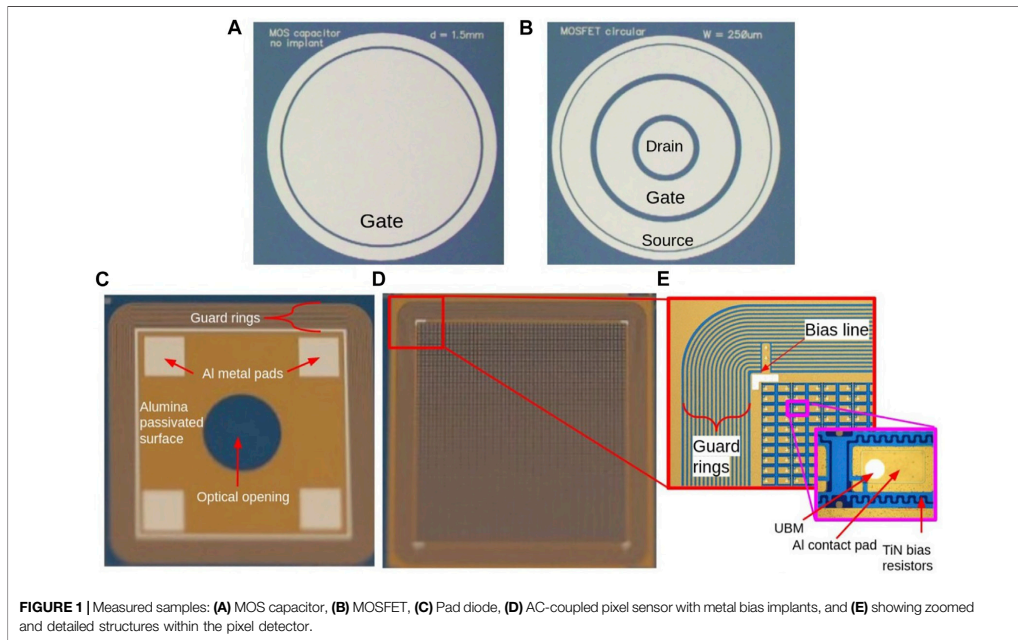


FIGURE 1 | Measured samples: **(A)** MOS capacitor, **(B)** MOSFET, **(C)** Pad diode, **(D)** AC-coupled pixel sensor with metal bias implants, and **(E)** showing zoomed and detailed structures within the pixel detector.

The main aspects of the study associated to the measured samples are as follows:

- First, a comparison study based on the characterization of the devices with either Al_2O_3 or $\text{Al}_2\text{O}_3 + \text{HfO}_2$ as a dielectric insulating layer. This is performed by measuring the oxide and oxide-silicon interface charges of pre- and post-irradiated MOS capacitors and MOSFET devices.
- Second, electrical characterization based on current-voltage (I-V), capacitance-voltage (C-V), and e-TCT measurements on AC-coupled pixel sensors with the different dielectrics. Simultaneously, TCAD simulation studies were performed to study the coherence.

The samples were irradiated with 10 MeV protons up to a fluence of 5×10^{15} protons/cm². A theoretical value of a magnitude of 3.87 was considered as the NIEL scale factor for silicon.

3 CHARACTERIZATION OF DEVICES

3.1 MOS Capacitors

C-V measurements of a MOS capacitor are performed by measuring the capacitance values with voltage sweep applied across the metal contact, called the gate, as shown in **Figure 1A**. C-V measurements in MOS capacitors are used to determine the effective oxide and mobile charges of the insulating layer by

studying their flat-band voltage. The flat-band voltage is defined as the gate voltage value at which the energy band of the substrate is flat at the silicon and oxide layer interface. In ideal conditions, without any oxide and interface-trapped charges, this value is -0.54 V for MOS devices with aluminum as the metal gate and a silicon substrate with a doping concentration of 8×10^{11} cm⁻³. The shift in the flat-band voltage (ΔV_{fb}) from its ideal condition gives an estimation of the effective fixed oxide charges (N_f). A fixed oxide charge is a non-ideal condition in MOS capacitors caused by ions which are incorporated in the oxide during growth or deposition (Hu, 2010).

As the MOS capacitors possess a p-type substrate, an accumulation layer is formed when applying a negative bias to the gate due to holes at or near the surface. This surface accumulation condition provides information about the effective fixed oxide charges as the shift in the flat-band voltage from ideal condition (where $V_{fb} \neq V_{gate}$) corresponds to the maximum capacitance value solely determined by the oxide layer. With positive sweep in the applied gate voltage, the device reaches its flat-band condition and is eventually driven to inversion. Generation of minority charge carriers (electrons in case of p-type substrate) in the inversion region is dependent on the frequency of the measurement. This is due to the difference in the response times of the majority and minority carriers corresponding to the applied voltage. At lower frequencies, the capacitance reaches back to its maximum value for positive gate voltage values due to the formation of the inversion layer by the

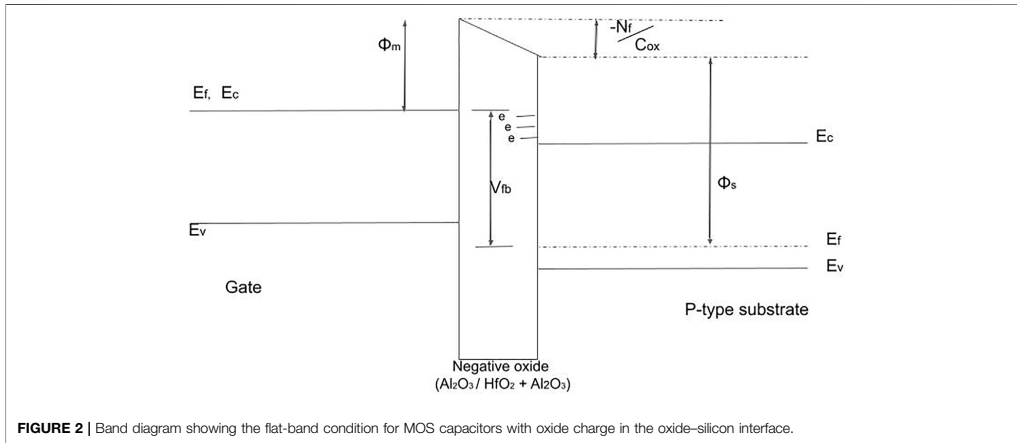


FIGURE 2 | Band diagram showing the flat-band condition for MOS capacitors with oxide charge in the oxide-silicon interface.

minority carriers in the oxide–substrate interface. However, at high frequencies, the system is not in thermal equilibrium state where the minority carriers find the sweep rate of the DC gate bias too rapid to follow. Consequently, no inversion layer is formed where a non-equilibrium condition is reached. At this point the neutrality is satisfied when the depletion width gets wider than its value during thermal equilibrium. This results in the lowering of the capacitance value below the saturated thermal equilibrium value, and the device is driven toward deep-depletion condition. Due to this phenomenon, the C-V measurements at a high frequency give rise to an S-shaped curve. All of the MOS capacitors in this study were performed at a high frequency of 1 kHz and an AC signal amplitude of 998.5 mV. The flat-band voltage is experimentally derived by differentiating the $(C_{measured}/C_{oxide})^{-2}$ versus bias voltage curve twice. The bias voltage value corresponding to the peak in the double differentiated curve is equal to the flat-band voltage value. Second differentiation usually introduces a great deal of noise as the bias voltage sweeps toward the deep-depletion region but that can be avoided by smoothing the data (Schroder, 2005). The oxide charge density can be determined from the flat-band voltage shift in the C-V curves. A positive value of the effective fixed oxide charge shifts the C-V curve to negative values of applied gate voltages in comparison to ideal C-V curve and vice versa.

In ideal conditions, the flat-band voltage is calculated as the difference in the work function of the metal and substrate. However, on considering the presence of oxide charges in the dielectric layer, the band diagram is modified, as shown in **Figure 2**. The oxide charge for simplicity is taken to be at the interface of oxide and substrate and induces an electric field with oxide voltage of $-N_f/C_{ox}$. Consequently, negative oxide in the dielectric changes the flat-band voltage as follows:

$$V_{fb} = \Phi_m - \Phi_s + \frac{N_f}{C_{ox}} \tag{1}$$

As Al_2O_3 and HfO_2 are negative oxides, oxide charge N_f shifts the flat-band voltage and consequently the threshold voltage to higher positive values.

The effective fixed oxide charges can be determined using the following relationship:

$$N_f = \Delta V_{fb} \times C_{ox} \tag{2}$$

where C_{ox} is the oxide capacitance corresponding to the accumulation region of the C-V curve. The fixed oxide charge density is further calculated by dividing N_f by the active area of the MOS capacitors.

Another non-ideal condition in MOS capacitors can be noticed due to the mobile charges (N_m) by the hysteresis in the high-frequency capacitance curve when sweeping the gate voltage back and forth from accumulation to inversion region and vice versa (Fowkes and Burgess, 1969). The mobile charges are due to the positive trapped charges induced into the oxide. It has been studied that the origin of mobile ions charges is due to heavy alkaline metallic contamination, like Na^+ and K^+ ions in case of SiO_2 introduced in the oxide layer during the fabrication steps (Repace, 1977; Schroder, 2005; Achuthan, 2007). However, the origin of mobile charges due positive trapped charges in the oxide layer in case of Al_2O_3 and HfO_2 needs further investigation. The shift toward applied voltage in the measured curves differ since a positive gate voltage causes mobile charge to move away from the gate electrode, while a negative voltage attracts the charge toward the gate (Hu, 2010). Therefore, the incorporation of the mobile charges can be used as a factor to determine the sensitivity of the oxide layer in MOS capacitors.

3.2 MOSFET

An increase in the gate voltage (V_g) with positive polarity repels the holes from the surface of the substrate. As a consequence the surface is depleted of mobile charge carriers, and the charge density in the depletion region is dependent on the doping

concentration of the substrate. With an increase in V_g , beyond the threshold voltage (V_{th}), the concentration of conduction electrons increases at the substrate–oxide interface, thereby generating an n-type “inversion” layer at the surface of the substrate. The inversion layer electrons serve as a resistive channel for the current to flow between the highly conductive source to drain regions (Hu, 2010).

Charge built up in the oxides and the silicon–oxide interface of MOS transistors (MOSFETs) due to high-energy ionizing radiation aids in determining the sensitivity of the insulating layer. When exposed to high-energy ionizing radiation, the oxide in MOSFETs generates electron-hole pairs. In our case of p-type substrate MOSFETs, with a positive applied gate bias, most of the electrons and hole pairs that escape recombination advance through the localized states in the oxide and rapidly drift toward the gate and the silicon–oxide interface, respectively. These holes are trapped in the silicon–oxide interface as they “jump” across the localized states within the oxide where they react and form interface traps. It has been studied that due to ionizing irradiation, hydrogen ions are released as holes. The oxide-trapped and interface-trapped charges are studied by determining the threshold voltage (V_{th}) in drain-to-source current (I_{ds}) versus gate voltage (V_g) characterization at a constant drain-to-source voltage (V_{ds})—also known as transfer characteristics. The threshold voltage is the point of inflection beyond which I_{ds} increases exponential with gradual increase in V_g . At V_{th} , interface traps are predominantly positively charged for p-channel transistors and negatively charged for n-channel transistors (Schwank et al., 2008).

The native negative oxide charges and the radiation-induced electron traps in the oxide layer as well as at the interface leads to significant changes in the MOSFET's channel currents. The channel current is very sensitive to the trapped charges at the interface as they are localized close to the channel. Therefore, the shift in the threshold voltage is a direct measure of the concentration of the charges trapped in the oxide and the interface of the silicon and insulating layer, as mathematically derived in Freeman and Holmes-Siedle (1978).

For measuring the transfer characteristics of the MOSFETs, the samples are placed on a chuck which is in contact to its backplane. The chuck is grounded virtually with a 0 Ω resistor. There are three needles, each connected to the gate, source, and drain, respectively. The needles are held by the micro-manipulator which helps in making the metallic contacts and guard rings by moving them in three dimensions (– x, – y and – z directions) by the help of fine adjustment screws. The needle in contact with the gate is used to apply bias voltage with the help of a DC power supply (with a voltage range of ± 200 V). The other two needles connected to the source and drain are grounded with 0 Ω resistor and Keithley 6487 picoampere meter, respectively. Keithley 6487 is used to measure the drain-to-source current (I_{ds}). It consists of a voltage source which is completely isolated from the electrometer. This enables us to measure the I_{ds} (with sweeping V_g) by simultaneously setting the drain-to-source voltage (V_{ds}) fixed at a constant value. Output characteristics of the MOSFETs were recorded by measuring the variation in I_{ds} with sweeping V_{ds} for specific V_g values. This in turn will enable

us in determining the threshold voltage, identified as the gate voltage value beyond which the device is no longer operating in the cut-off region.

3.3 Diodes and Pixel Detectors

The radiation hardness studies of AC-coupled pixel sensors without any implanted bias lines were performed using C-V and TCT methods. The full depletion voltage and the silicon bulk capacitance after full depletion were determined using C-V measurements on pre- and post-irradiated AC-coupled pixel sensors containing Al_2O_3 or $Al_2O_3 + HfO_2$ as the dielectric insulating material. Based on C-V measurements, the full depletion voltage of the detector is identified as the bias voltage beyond which the capacitance is constant. The value is extracted by determining the inflection point in inverse-square capacitance versus bias voltage ($1/C^2$ -V) plot. The effective doping concentration (N_{eff}) value of the detector substrate is determined from the full depletion voltage (V_{fd}) by using the following relation:

$$N_{eff} = \frac{2\epsilon_0\epsilon_{Si}V_{fd}}{eW^2}, \quad (3)$$

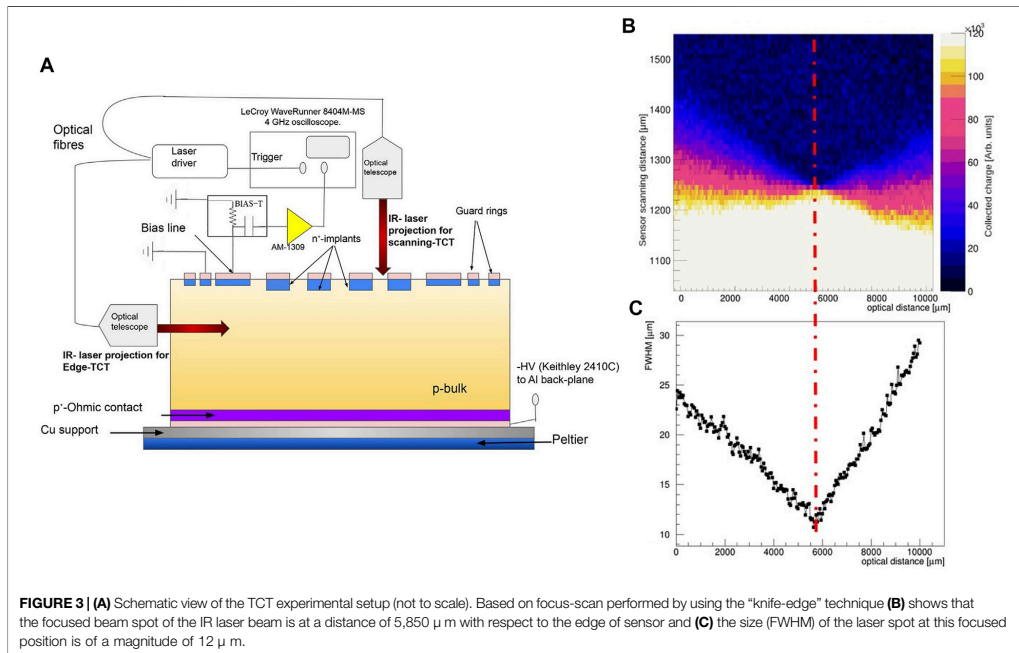
where ϵ_0 and ϵ_{Si} are the permittivities of the vacuum and silicon, respectively, and W is the substrate thickness. Furthermore, the resistivity (ρ) of silicon substrate can be calculated from the effective doping concentration and charge carrier mobility, using the following relation:

$$\rho = \frac{1}{e\mu_h N_{eff}}, \quad (4)$$

where μ_h is the hole mobility as the detectors possess a p-type substrate.

For C-V characterization of the sensors and MOS capacitors, we used the LCR meter E4980A with a test frequency range from 20 Hz to 1 MHz to measure capacitance with an accuracy of 1 ff. Due to the technical limitations of this setup, only high-frequency C-V curves at 1 kHz were taken into consideration during the measurements. The device has a maximum signal voltage level of 1 V. The bias voltage is provided to backplane with help of a Keithley 2410C sourcemeter that can provide voltage within the range of ± 1000 V. The voltage source has a maximum current of 1 mA and can also measure higher currents which is useful in case of irradiated samples. There are two needles, one connected to the bias line in case of pixel detectors or the metal contact pad in diodes from where the capacitance is measured, while the other is connected to the innermost guard ring of the sensor which is grounded. A detailed schematic and explanation of the setup has been described in Arsenovich (2020).

The variation in total dark leakage current densities, leakage current damage factor (α), electric field, and charge collection efficiency (CCE), due to irradiation, were measured using the TCT characterization method. TCT is a method commonly used for electrical characterization of semiconductor detectors. In TCT, a fast pulsed infrared (IR) laser is used to imitate the crossing of minimum ionizing particles (MIPs) through the detector. The photons of IR laser traversing through the depleted region within the bulk generate charge carriers and



provide a better approximation of high-energy particles interacting with the detector. These carriers (electrons and holes) traverse from the generation point within the bulk toward their respective electrodes. The resulting transient signal induced by the movement of the charge carriers in an electric field, according to the Shockley–Ramo theorem, is detected by the oscilloscope. The shape of the signal is studied to analyze the electric field, doping concentration, and the charge collection efficiency of the detector. The collected charge at a given bias voltage is calculated by integrating the current signal over time. On performing a voltage sweep at a given position on the sensor optically exposed to the laser beam, the saturation of the collected charge beyond a certain bias can be interpreted as the onset of full depletion of the sensor (Eremin et al., 1996; Fretwurst et al., 1997; Mandić et al., 2015, 2013, 2014).

The measurements in this study were performed with a Particulars d.o.o. (Ljubljana, Slovenia) based scanning-TCT setup. An IR laser (1,064 nm) directed either toward the front side plane or the edge of the sensor was used. The laser pulse was transmitted to the detector by an optical fiber. The signal was identified in areas without any metal as the photons could pass through the active depleted region and generate the charge carriers. The measurements were performed at a low IR laser intensity of 60%, equivalent to the charge deposition of 5–10 MIPs and repetition rate of 1 kHz. The reverse bias voltage is applied to the backplane of the sensor, while the transient signal is read from the front bias line of the pixel sensor with the n^+ -implant. The first guard ring surrounding the bias line is grounded with a 50 Ω terminator. In addition to the IR laser, the

other components in the measurement setup were focusing optics, a sample holder mounted on a XYZ stage for scanning the entire surface of the detector, a Keithley 2410C 1100 V Sourcemeter unit, bias tee, a wide band current amplifier with a Tenma power supply, and a LeCroy WaveRunner 8404M-MS 4 GHz oscilloscope. During the measurement campaign, an average of more than 100 waveforms was recorded at each scanning point by the oscilloscope. An offset correction for the onset time and baseline was applied to all measurements. **Figure 3A** shows a schematic view of the electronic connections during the measurement.

The collected charge and the depletion width of the detector can be studied by projecting the IR laser beam across the edge of the detector, also known as the edge-TCT (e-TCT) characterization method. **Figure 3A** portrays a layout for the characterization of the sensor using e-TCT as well. The focus spot of the Gaussian laser beam is determined by using the “knife-edge” technique (Khosrofiyan and Garetz, 1983; de Aratijo et al., 2009). As shown in **Figure 3C**, the beam size is $\sim 12 \mu\text{m}$. The corresponding position of the focused beam spot was calculated to be at a distance of 5,680 μm with respect to the edge of the active region of the sensor, as shown in **Figure 3B**. The depth profile is calculated by recording the current signals as the laser scans across the depth of the sensor.

Furthermore, the electric field within the active region of the depleted bulk of the detector can be determined by producing the drift velocity profiles while scanning the IR laser beam across the depth of the detector. The induced current signal generated initially due to the charge carriers is given by the following expression:

$$I(y, t \sim 0) \approx \epsilon AN_{e,h} \frac{v_e(y) | v_h(y)}{W} \quad (5)$$

Furthermore, on expressing the drift velocity to mobility, we get the following relationship:

$$I(y, t \sim 0) \approx \frac{\epsilon AN_{e,h}}{W} [\mu_e(E) | \mu_h(E)] E(y). \quad (6)$$

Therefore, the drift velocity can be predicted by integrating over the initial rise time of the current signal. The signal rise time is ~ 300 ps, which is of the same order of magnitude as the trapping time for detectors irradiated at a fluence of 10^{15} protons/cm². Therefore, as the maximum drift distance of the charge carriers at 300 ps is ≈ 30 μ m, which is comparable to size of the beam, the drift velocity profiles were calculated by integrating over 300 ps of the signal rise time. This is also known as the prompt current method (Canali et al., 1971).

As shown in Eq. 6, the drift velocity can be expressed in terms of an electric field and mobility, where according to our approximation the mobility of the charge carriers is constant across their drift length. In cases where the drift velocity has not saturated as function of electric field strength, the sum of the drift velocities (of both electrons and holes) gives an image of the electric field strength within the sensor. Studies have been performed under the RD50 collaboration at CERN to investigate the carrier mobility dependence on fluence by magnetoresistance means. Results show an inverse-square root dependence of mobility on fluence values beyond a magnitude of 1×10^{14} neq/cm², for low electric fields. However, for high electric fields, the variation of carrier mobility does not change that significantly with fluence, except for heavily irradiated sensors beyond 1×10^{15} neq/cm². The total mobility of the charge carriers decreases by $\sim 20\%$ on irradiating silicon detectors from 1×10^{14} to 1×10^{15} neq/cm², depending on the concentration of cluster defects in the bulk (Vaitkus et al., 2021). However, the variation in the mobility of the charge carriers with an electric field has not been taken into consideration to simplify the model for our measurements.

Furthermore, in order to cross-check the investigations of the electric field distribution with simulation, a larger 2-D structure was created. The simulated sensor configurations were designed with parameters as close to the real sensors as possible. The sensor had a physical thickness of 320 μ m, a pitch of 150 μ m, and a pixel implant width of 100 μ m. The doping concentration of the p-type bulk was set to 8×10^{11} cm⁻³. In addition to that the heavily phosphorus-doped silicon implants in the front and boron implantation on the backplane had peak concentrations of a magnitude of 1×10^{15} cm⁻³ and 5×10^{15} cm⁻³, respectively. Each pixel had a biasing electrode as well as AC-coupled charge collecting contacts. The reverse bias voltage was provided to the backplane Ohmic contact at room temperature.

4 RESULTS

4.1 Proton-Irradiated MOS Capacitors and MOSFETs

4.1.1 C-V Measurements of MOS Capacitors

C-V curves for MOS capacitors with different oxides are shown in Figures 4A,B. The curves were recorded by

sweeping the gate voltage from accumulation to inversion, that is, starting from negative to positive values as the devices possess a p-type substrate and vice versa. As explained earlier, the hysteresis in the C-V curve for each sample helps in analyzing the concentration of mobile charges in the insulating layer. The results show no significant hysteresis in voltage sweep for non-irradiated sample. However, a shift in the flat-band condition voltage (V_{fb}) from ideal conditions (where $V_{fb} = -0.54$ V for MOS devices with aluminum as the metal gate and a silicon substrate with a doping concentration of 8×10^{11} cm⁻³) is observed in the non-irradiated MOS capacitors, irrespective of the nature of the oxide layer. Nevertheless, MOS capacitors with a combination of Al₂O₃ + HfO₂ as the oxide layer possess a V_{fb} shift of (2.18 ± 0.35) V lower than those with Al₂O₃ as the dielectric layer. This corresponds to a decrease in the fixed oxide charges by a factor of ~ 1.5 for samples with HfO₂, as shown in Figure 5A. The fixed oxide charge increases by a factor of ~ 3 with irradiation and this is observed as a positive shift in the flat-band voltage. The physics behind this can be explained as a consequence of increasing negative charge accumulation at the oxide-silicon interface that causes the bands to be pulled down farther in equilibrium. In order to achieve the flat-band condition, one must apply a positive voltage to overcome the inherent bending of the bands. A negative charge in the oxide near the p-type silicon substrate aids in increasing the holes on the surface, so the gate voltage required to invert the surface to become n-type is increased, as a consequence of which, this behavior will lead to shifts in the threshold voltage as well to higher positive values.

No hysteresis for non-irradiated MOS capacitors was observed, thereby inferring that there are no positive heavy alkaline ions induced in the oxide layer due to contamination during the fabrication steps. However, the hysteresis observed for irradiated samples is possibly due to the mobile charges originating from radiation-induced traps. Furthermore, the effective mobile charge increases on irradiation of the MOS capacitors to a fluence of 5×10^{14} protons/cm². The value is by a factor of ~ 1.6 higher in case of samples possessing Al₂O₃ + HfO₂ in comparison to those consisting of Al₂O₃ alone, as shown in Figure 5B. This shows that MOS capacitors with HfO₂ show higher sensitivity to irradiation.

The simulated MOS capacitor structure had dimensions of $1 \times A \times 320$ μ m³, where A is the area factor to match the dimensions with the real device. The thicknesses of the Al₂O₃ and HfO₂ as the insulating layer for the devices were identical to the fabricated samples. The bulk doping concentration was set to 6×10^{11} cm⁻³. The V_{fb} shift due to irradiation can be assessed from measurements, as shown in Figure 4C, and it is directly assigned to an amount of oxide charge density (Q_{ox}) increase at the oxide-silicon interface. These variables are then used as input parameters for the TCAD surface damage model. The oxide-silicon interface is also characterized by interface traps distributed throughout the silicon energy gap. From a macroscopic point of view, it is represented as a stretch out in the high-frequency capacitance-voltage curve. The interface trap states density D_{it} can be estimated by means of the

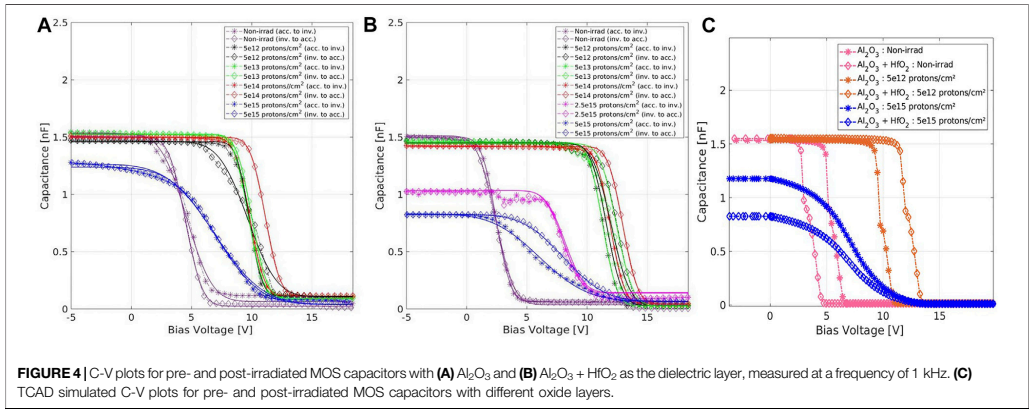


FIGURE 4 | C-V plots for pre- and post-irradiated MOS capacitors with (A) Al_2O_3 and (B) $\text{Al}_2\text{O}_3 + \text{HfO}_2$ as the dielectric layer, measured at a frequency of 1 kHz. (C) TCAD simulated C-V plots for pre- and post-irradiated MOS capacitors with different oxide layers.

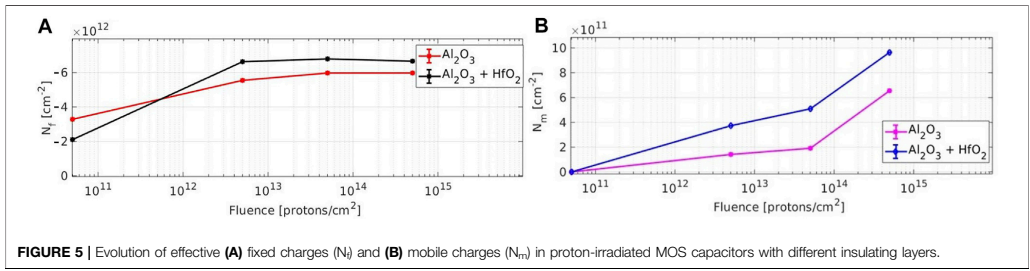


FIGURE 5 | Evolution of effective (A) fixed charges (N_f) and (B) mobile charges (N_m) in proton-irradiated MOS capacitors with different insulating layers.

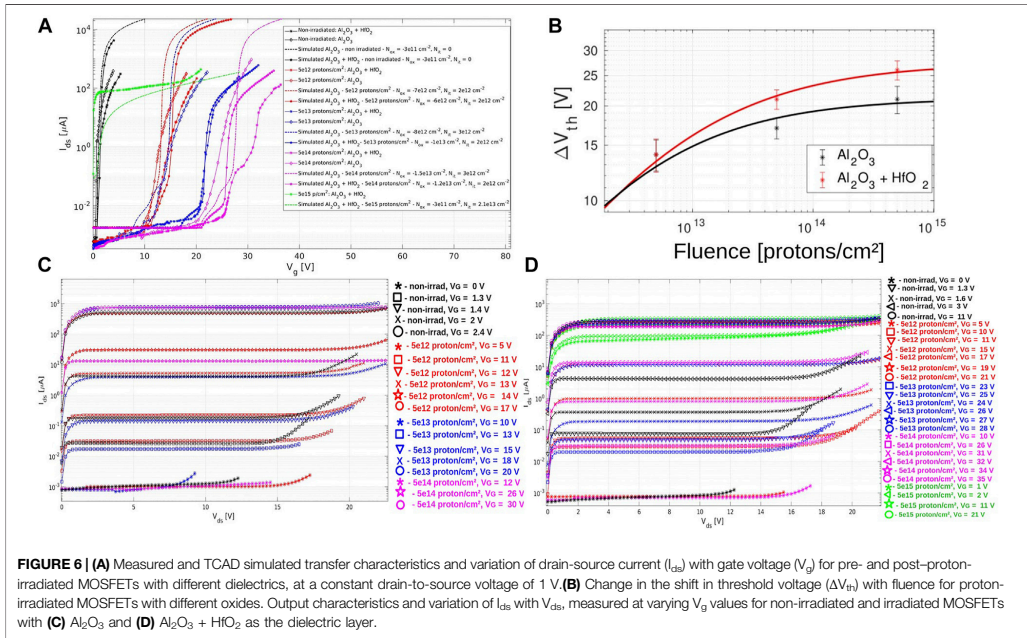
TABLE 1 | Details of the surface damage model.

Type of trap	Level (eV)	σ_e (cm^2)	σ_h (cm^2)	Fluence (protons/ cm^2)	Concentration (cm^{-2})
Donor	Ev+0.5	$1 \cdot 10^{-16}$	$1 \cdot 10^{-15}$	0	$5 \cdot 10^{11}$
Acceptor	Ec-0.5	$1 \cdot 10^{-15}$	$1 \cdot 10^{-16}$	0	$5 \cdot 10^{11}$
Donor	Ev+0.5	$1 \cdot 10^{-16}$	$1 \cdot 10^{-15}$	$5 \cdot 10^{12}$	$5 \cdot 10^{11}$
Acceptor	Ec-0.5	$1 \cdot 10^{-15}$	$1 \cdot 10^{-16}$	$5 \cdot 10^{12}$	$5 \cdot 10^{11}$
Donor	Ev+0.5	$1 \cdot 10^{-16}$	$1 \cdot 10^{-15}$	$5 \cdot 10^{15}$	$7 \cdot 10^{12}$
Acceptor	Ec-0.5	$1 \cdot 10^{-15}$	$1 \cdot 10^{-16}$	$5 \cdot 10^{15}$	$3 \cdot 10^{12}$
—	—	—	—	Fluence (protons/ cm^2)	Oxide charge (cm^{-2})
—	—	—	—	0	$2 \cdot 10^{12}$
—	—	—	—	$5 \cdot 10^{12}$	$4.8 \cdot 10^{12}$
—	—	—	—	$5 \cdot 10^{15}$	$3 \cdot 10^{12}$

capacitance high-low method (Nicollian and Brews, 1982). Due to the technical limitations in low-frequency measurements and inaccuracies at extremely high-frequency, C-V curves for MOS capacitors were obtained at only 1 kHz. Therefore, the D_{it} was found by fitting simulated C-V curves to the measurement results. The interface states were modeled with two single trap levels, one donor at 0.50 eV from the valence band edge (E_V) and one acceptor at 0.50 eV

from the conduction band edge (E_C). All the parameters that were used for the surface damage model are listed in the **Table 1**.

It is evident from **Figure 4C** that for the first radiation fluence step there is only an increase in the effective oxide charge with no change in the interface trap concentration. However, for the highest fluence dose, an increase in the interface trap concentration occurs. The simulation adds



evidence to the fact that the interface traps play an important role for higher fluences.

4.1.2 Output and Transfer Characteristics of MOSFETs

Radiation-induced threshold voltage shift due to charges trapped in the gate oxide as well as the oxide-silicon interface is dependent on the irradiation dose that the MOSFET device is exposed to. The total shift in the threshold voltage (ΔV_{th}) is the sum of the threshold voltage shifts due to oxide trap (ΔV_{ot}) and interface trap charge (ΔV_{it}) as shown below:

$$\Delta V_{th} = \Delta V_{ot} + \Delta V_{it} \tag{7}$$

The cumulative shift in the threshold voltage depends on the increase in oxide-trapped charges (N_{ot}) and interface-trapped charges (N_{it}), given by the following equation:

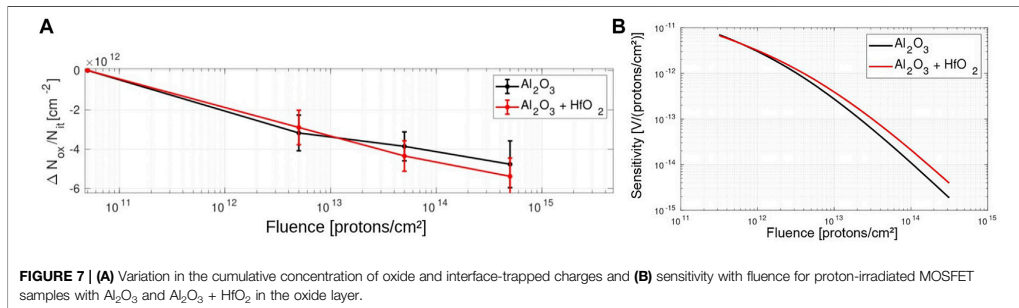
$$\Delta(N_{ot}/N_{it}) = \Delta V_{th} \times C_{ox} \tag{8}$$

where C_{ox} is the oxide capacitance in the accumulation region retrieved from C-V measurement.

The generation of dangling bonds in the oxide-silicon interface due to irradiation is responsible for predominantly trapping holes as they hop across the localized states in the oxide where they react and form the interface traps. An increase in the interface-trapped charges decreases the channel mobility. As a consequence of the deep hole trapping, a high amount of negative charge gets accumulated in the interface forming the interface traps in

the n-channel MOS. On the other hand, defects in the oxide generated by radiation lead to trapping of negative charge, thereby causing an increase in applied gate voltage value to reach threshold condition. At high radiation doses to 5×10^{14} protons/cm², the concentration of oxide traps supersedes the interface charges causing a positive shift in threshold voltage, as shown in **Figure 6A**.

TCAD simulation was performed on pre- and post-irradiated MOSFETs with alumina and hafnia as the dielectric layer to cross-check the transfer characteristics. The simulated MOSFET structure had dimensions similar to the specifications provided in **Section 2**. The doping concentration and the energy level parameters were similar to that of the MOS capacitors, as listed in **Table 1**. The results are congruous to the measurements where the shift in the threshold voltage to higher bias values is due to the cumulative contribution of negative oxide and interface-trapped charges. Up to a fluence of 5×10^{14} protons/cm², the oxide-trapped charges supersede the interface traps, giving rise to a positive shift in the threshold voltage. However, at fluences above 5×10^{14} protons/cm², the concentration of the interface-trapped charges exceeds that of the oxide traps causing a huge increase in the leakage current (by ~ 4 orders of magnitude) as well as a slightly negative shift in the threshold voltage that can potentially cause a breakdown of the chip (Lho and Kim, 2005). Therefore, as shown in **Figure 6B**, the variation in the effective threshold voltage with fluence was taken into account for samples with different dielectric layers irradiated



to a fluence of 5×10^{14} protons/cm². The threshold voltage value can be extracted by determining the *x*-axis coordinate of the intersection point for the two linear fits which correspond to the inflection point in each of the *I*_{ds} versus *V*_g curves, shown in **Figure 6A**, for pre- and post-proton-irradiated MOSFETs with different dielectrics.

The cumulative shift in the oxide and interface-trapped charges, Δ(*N*_{ox}/*N*_{it}) as in **Figure 7A**, increases by a factor of ~5 when irradiated to a fluence of 5×10^{14} protons/cm². As the devices operate in low-field regimes, the following curve was utilized to fit in the Δ*V*_{th} versus fluence plot:

$$\Delta V_{th} = a + \frac{a}{1 + bD^c} \tag{9}$$

where *D* is the proton fluence and (*a*, *b*, *c*) are three curve-fit parameters. The boundary conditions are defined such that for non-irradiated samples when *D* is zero Δ*V*_{th} is also zero. Furthermore, when fluence goes to infinity, *a* saturates to its maximum value corresponding to no further change in threshold voltage at the maximum fluence of proton irradiation. The value of parameter *a* extracted from the fit was five times higher for samples with Al₂O₃ + HfO₂ as the dielectric layer.

The sensitivity (ratio of the change in threshold voltage to fluence) was calculated by using the parameters extracted from the fits for the different samples based on the nature of the dielectrics employed in MOSFETs. As shown in **Figure 7B**, MOSFETs with additional layer of HfO₂ show higher sensitivity to proton irradiation at high fluences. This is expected for MOSFETs with high-*k* dielectric materials (Yilmaz et al., 2008; Kaya et al., 2015; Kaya et al., 2018).

Furthermore, the output characteristics, as shown in **Figures 6C,D**, for MOSFETs with Al₂O₃ and Al₂O₃ + HfO₂ as dielectric layers, respectively, validate the reproducibility of the results in extraction of threshold voltage from transfer characteristics. The MOSFET is in the cut-off region for gate voltage values below the threshold voltage where the current is way too low (in nA scale) and the device is in off-state. At gate voltage values above the threshold value, *I*_{ds} values beyond the linear/ohmic region remain constant before undergoing breakdown. This operation region where *I*_{ds} remains constant with increasing *V*_{ds} is called the saturation region. It is important to note that for *V*_g > *V*_{th}, the *I*_{ds} values in the saturation region from output characteristics of non-irradiated

and irradiated MOSFETs are consistent with the *I*_{ds} values beyond *V*_{th} in the transfer characteristics.

4.2 Proton-Irradiated AC-Coupled Pixel Sensors

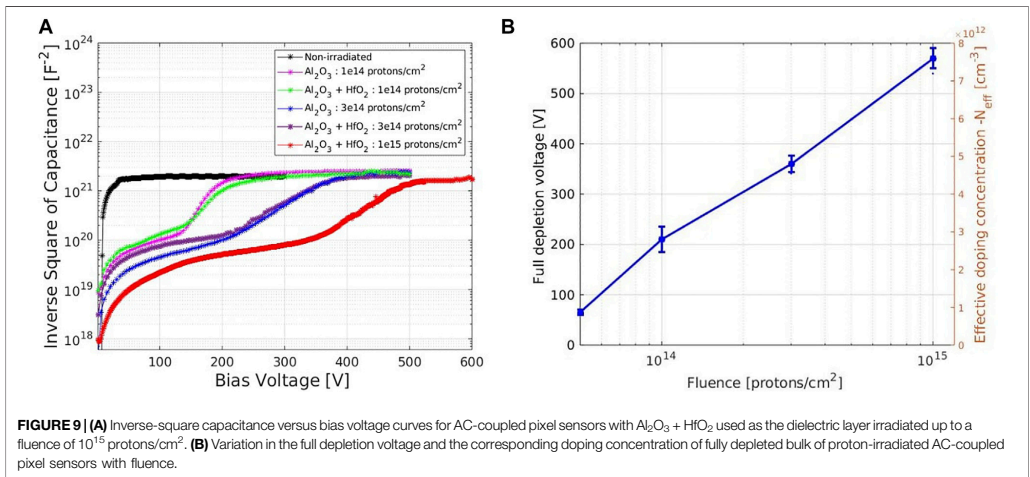
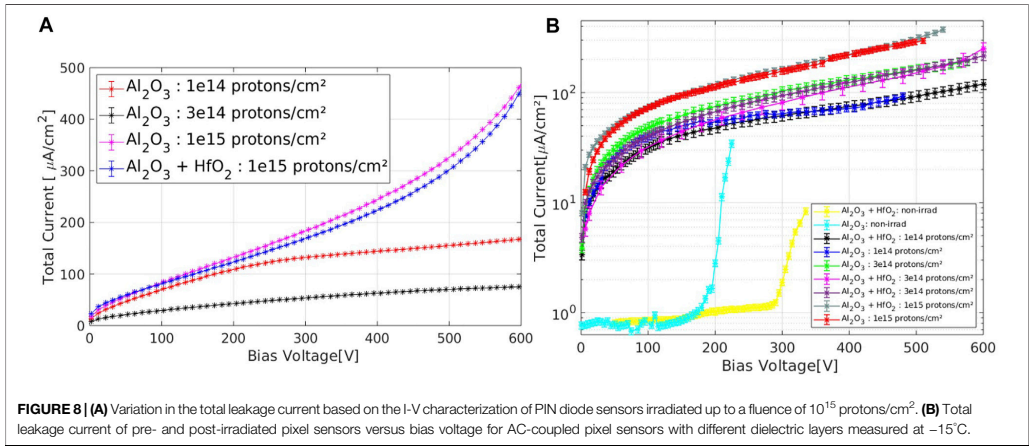
4.2.1 I-V/C-V Measurements

Figure 8A shows the variation in the total leakage current for PIN-diode-like structures irradiated up to a fluence of 10^{15} protons/cm², measured at a temperature of -15°C after annealing at room temperature for a day. Furthermore, the parameter damage factor (*α*) can be calculated with respect to the total leakage current of non-irradiated samples by using the formula from Moll (1999)

$$\alpha = \frac{I_{\text{irradiated sensor}} - I_{\text{non-irradiated sensor}}}{\Phi_{eq} V} \tag{10}$$

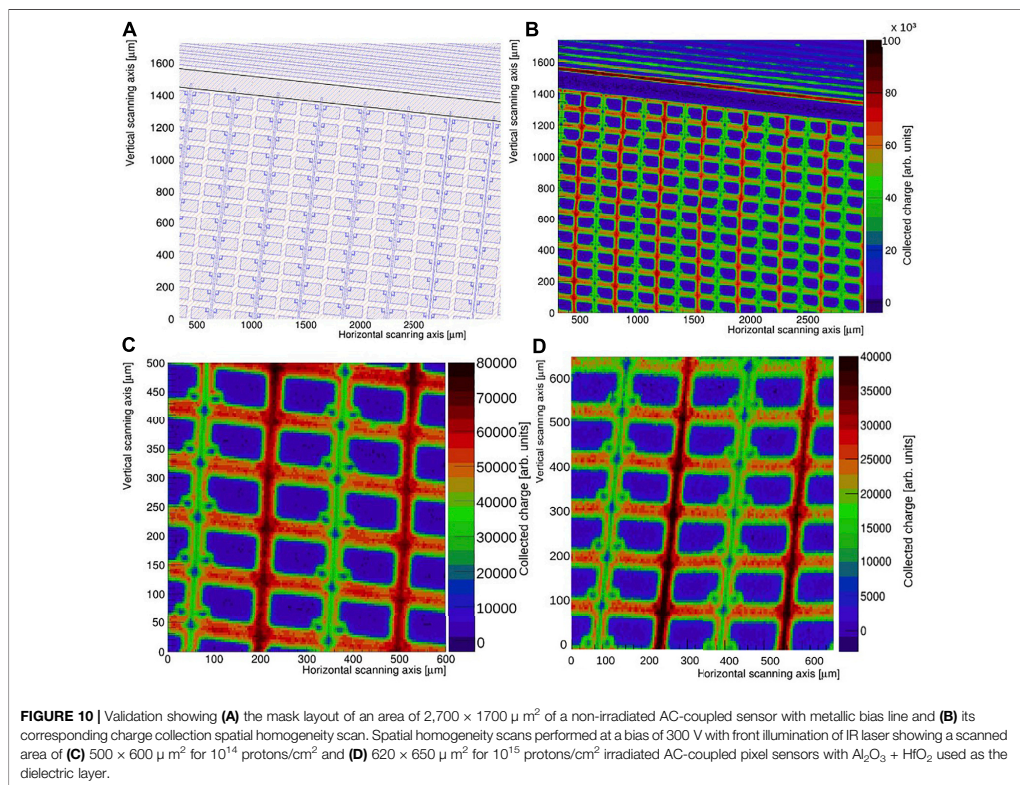
where the terms Φ_{eq} and *V* represent the fluence for proton irradiation and volume of the diode, respectively. The average value of *α* for fully depleted diodes irradiated up to a fluence of 10^{15} is $(4.55 \pm 0.65) \times 10^{-17}$ A/cm (Wiehe et al., 2018).

The total leakage current of the non-irradiated and irradiated AC-coupled pixel sensors with different dielectric layers, measured at a temperature of -15°C, is shown in **Figure 8B**. For non-irradiated sensors, the reverse bias total leakage current increases proportionally to the square root of the bias voltage until the detector breaks down beyond which the dark current rises more sharply. It is a characteristic feature of the non-irradiated pixel sensors to possess an early breakdown (Dieter et al., 2021). The possible reason for an early breakdown is due to the formation of an Ohmic current path along the detector surface resulting in the loss of electrical isolation between the pixels. The major difference is that samples with HfO₂ can sustain high bias voltages as it provides better insulation than sensors with Al₂O₃ alone as a dielectric layer. Non-irradiated pixel sensors with HfO₂ as an insulating layer have a maximum operational voltage, approximately 100 V higher. With irradiation up to a fluence of 10^{15} protons/cm², results show that the sensors with Al₂O₃ + HfO₂ as an insulating layer are able to sustain a higher electric field, and there is no breakdown visible up to the maximum test operational voltage of approximately 550 V.



The inflection point in the inverse-square capacitance versus bias voltage curves from the C-V measurements at room temperature, as shown in **Figure 9A**, provides the full depletion voltage of the detector. The increasing shift in the full depletion voltage with an increasing fluence of proton irradiation is irrespective of the nature of the insulating layer. It is important to note that full depletion voltage of the active bulk is attainable in case of pixel sensors with $\text{Al}_2\text{O}_3 + \text{HfO}_2$ as the oxide layer since they were able to sustain a high bias voltage without undergoing an early breakdown. The full depletion voltage of the active bulk of the detector, using **Eq. 4**, for non-irradiated sensors is approximately 76 V which corresponds to a doping concentration value of $1.08 \times 10^{12} \text{ cm}^{-3}$ and a resistivity of

12 kΩ cm. The resistivity of the fully depleted bulk based on the C-V measurements is increased by a factor of ~ 1.5 in comparison to the specifications of the wafers provided by Okmetic. The reason behind this observation is related to the thermal donors induced due to the oxygen diffusion in the magnetic Czochralski-grown silicon ingots along with additional heating that the wafer is subjected to during the detector processing steps (Tuovinen et al., 2007). Furthermore, with irradiation, as shown in **Figure 9B**, the full depletion voltage of the sensors irradiated up to a fluence of 10^{15} protons/cm² increases up to (570 ± 15) V. This corresponds to an increase in the doping concentration by factor of ~ 7 and decrease in the resistivity of the fully depleted bulk to approximately 2 kΩ-cm.



Also, unlike for the non-irradiated sensors, the inverse-square capacitance versus voltage curves for irradiated AC-coupled pixel sensors, as shown in **Figure 9A**, are non-linearly increasing before the full depletion of their bulk (Sato et al., 2020). This implies that the effective bulk resistivity after irradiation is not uniform along the depth of the detector due to trapping of charge carriers released by the generation current in the radiation-induced defects. Consequently, it results in space charge sign inversion of the detector close to the backplane of the sensor, thereby leading to a “double-junction” effect (Hara et al., 2016), explained in Section 4.2.2.

4.2.2 TCT Measurements

Front illumination of IR laser in TCT characterization of AC-coupled pixel sensors aids in studying the homogeneity in the collected charge spatially across the active region of the detectors. **Figure 10A** shows the mask layout of the scanned area for a non-irradiated pixel sensor with metallic bias line consisting of $\text{Al}_2\text{O}_3 + \text{HfO}_2$ as the dielectric layer in the detector. An area of $2.7 \times 1.7 \text{mm}^2$ was scanned with IR laser at a laser intensity corresponding to charge deposited

by approximately ~ 10 MIPs at a bias voltage of 280 V and a constant temperature of -15°C . The total dark current during the measurement at the corresponding bias was $12.15 \mu\text{A}$. **Figure 10B** shows the spatial homogeneity in the charge collected across the scanned area within the active region of the sensor. The region of minimum collected charge, according to the color scale, corresponds to the metallized region of the detectors, that is, the pixels, the bias lines, and the guard rings. The region of maximum collected charge corresponds to the spaces in the sensor without any metallization as the IR laser photons can pass through the bulk of the detector to generate the signal due to charge carriers collected by the electrodes. Since only the first guard ring is terminated with a 50Ω resistor and the subsequent guard rings are left floating, a gradient in the collected charge can be observed in the scans from the innermost to the outer guard rings. This ensures a gradual gradient in the potential as the voltage drops from outside in Evensen et al. (1993).

Figures 10C,D show a spatial scan of two pixel sensors, with $\text{Al}_2\text{O}_3 + \text{HfO}_2$ as the insulating layer, irradiated at 10^{14} protons/cm² and 10^{15} protons/cm². They were measured at a constant bias

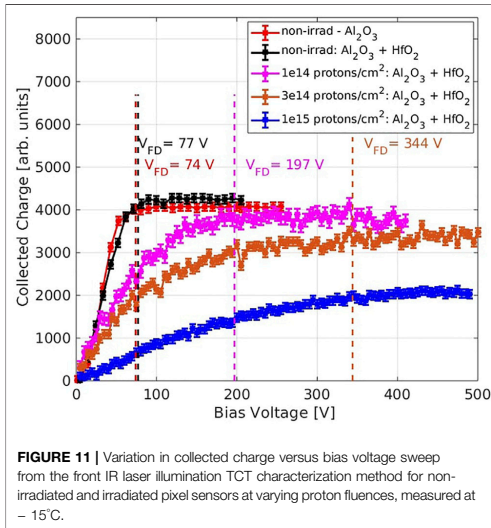


FIGURE 11 | Variation in collected charge versus bias voltage sweep from the front IR laser illumination TCT characterization method for non-irradiated and irradiated pixel sensors at varying proton fluences, measured at -15°C .

of 300 V and subjected with IR laser of the same intensity as for the non-irradiated sample. Results show that on proton irradiation, the resolution of the pixels based on the collected charge homogeneity scans does not change significantly. However, the maximum collected charge within the active region of the sensor is reduced by a factor of 2.25 (approximately 55%) and 1.13 (approximately 11%) for samples irradiated at fluences of 10^{15} protons/cm² and 10^{14} protons/cm², respectively. The reduction in the value of the collected charge is due to trapping of charge carriers in defect states within the bandgap of silicon (Oblakowska-Mucha, 2017). The reason for the traps is associated to the dislocation of the silicon atoms from its lattice site to an interstitial site leading to a displacement damage in the cascade of multiple interactions, thereby causing cluster defects (Lindström, 2003).

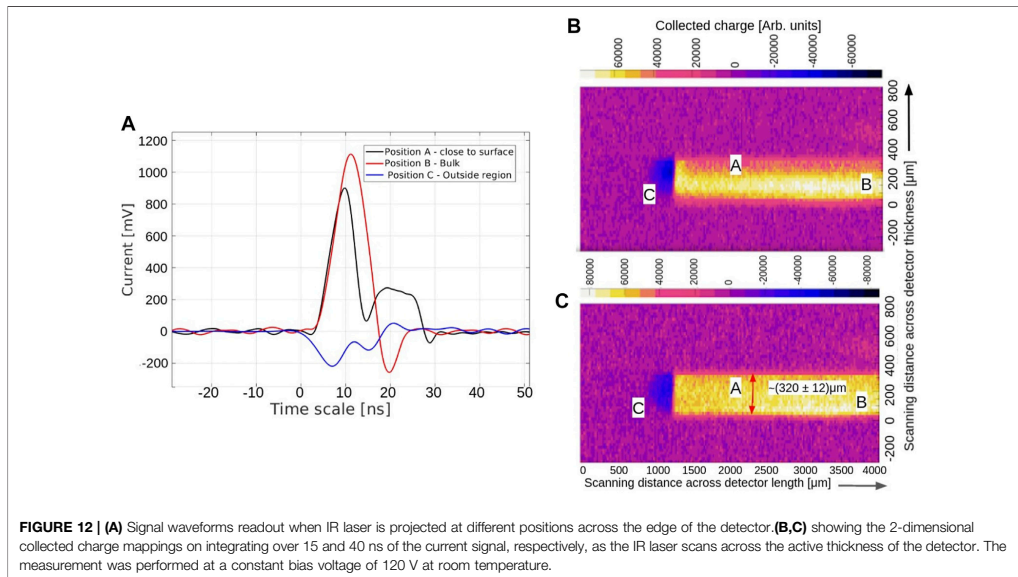
The full depletion voltage can be determined from the inflection point in the variation in a collected charge versus bias voltage plots for non-irradiated and irradiated sensors, as shown in Figure 11. The CCE for non-irradiated sensors does not depend on the nature of the employed insulating layer. The full depletion voltage of the non-irradiated pixel sensor extracted from the front illumination of IR laser in TCT measurement is of a magnitude of ~ 75 V, similar to the value extracted from the C-V measurements in Figure 9. As observed earlier in the spatial homogeneity scans for irradiated samples, the collected charge is reduced approximately by factor of 1.11, 1.27, and 2.1 for pixel sensors irradiated at fluences of 10^{14} , 3×10^{14} , and 10^{15} protons/cm², respectively. The corresponding full depletion voltages extracted from the “knee” point was identified to be of a magnitude of 197 and 344 V for sensors irradiated at fluences of 10^{14} and 3×10^{14} protons/cm², respectively. However, the

inflection point in the curve could not be identified for 10^{15} protons/cm² irradiated sample as the source measure unit (SMU) reached compliance at a bias of 492 V due to high reverse leakage current values.

Based on illumination of IR laser across the edge of the detector, e-TCT aids in evaluating the charge collection and electric field profiles by analyzing the drift velocity of the generated charge carriers across the active bulk of the sensor, as shown in the relation in Eq. 5. The amplitude and shape of the waveforms recorded by the oscilloscope vary depending on the position at which the IR laser is projected across the edge of the sensor, as shown in Figure 12A. In reverse bias conditions, when the laser beam is pointed at a distance of 30 μm from the surface of the sensor, the electrons drift quickly toward the electrodes close to the segmented n⁺ implants as in case of silicon the electron mobility is ~ 3 times higher than hole mobility. The generated electrons are collected rapidly close to the front surface electrodes and contribute toward the rise time of the signal peak. Meanwhile, the holes traverse through the entire bulk and are collected toward the electrode on the backplane of the sensor and give rise to the transient current signal, detected by the oscilloscope, as the movement of charge induced in an electric field is in accordance with the Shockley-Ramo theorem (Shockley, 1938; Ramo, 1939). Furthermore, charge carriers generated due to the projection of the IR laser beam within the bulk, ~ 190 μm from the surface of the sensor, drift toward their respective electrodes giving rise to a Gaussian signal. The negative polarity is a consequence of reflections due to impedance mismatching between the bias tee and the detector (Kramberger et al., 2010).

Figures 12B,C show the homogeneity in the collected charge mapping for a non-irradiated pixel sensor at a constant bias voltage of 120 V at room temperature by integrating the current signal over 15 and 40 ns, respectively. Integrating the signal over a timescale of 40 ns gives an estimation of the bulk thickness with a magnitude of (320 ± 12) μm . The uncertainty of 12 μm is arising from the size of the Gaussian laser beam. The e-TCT collected charge scans were performed over a length of 2.7 mm within the active region of the sensor along with one of its ends consisting of the guard rings. A gradient in the negative collected charge corresponding to the negative signal can be observed within the region under the guard rings in the spatially scanned maps. The first guard ring that is grounded contributes to the negative signal with a low amplitude due to the generated holes which charge and discharge the active region (similar to that of a capacitor) as they share the common ohmic backplane from where the sensor is biased (Bharthuar et al., 2020). However, no signal was detected beyond 2.7 mm (toward the right side of the plot) of the scanning length of the sensor as the HV bias line attached to the spring connector of the readout board blocked the laser beam from reaching the sensor.

Charge collection profiles at different bias voltages for non-irradiated pixel sensors with different dielectrics, as can be seen in Figures 13A,B, show no difference depending on the nature of the dielectric material implemented in the detector. The magnitude of the normalized charge collection value saturates to a maximum amplitude of ~ 1 throughout the active bulk of the



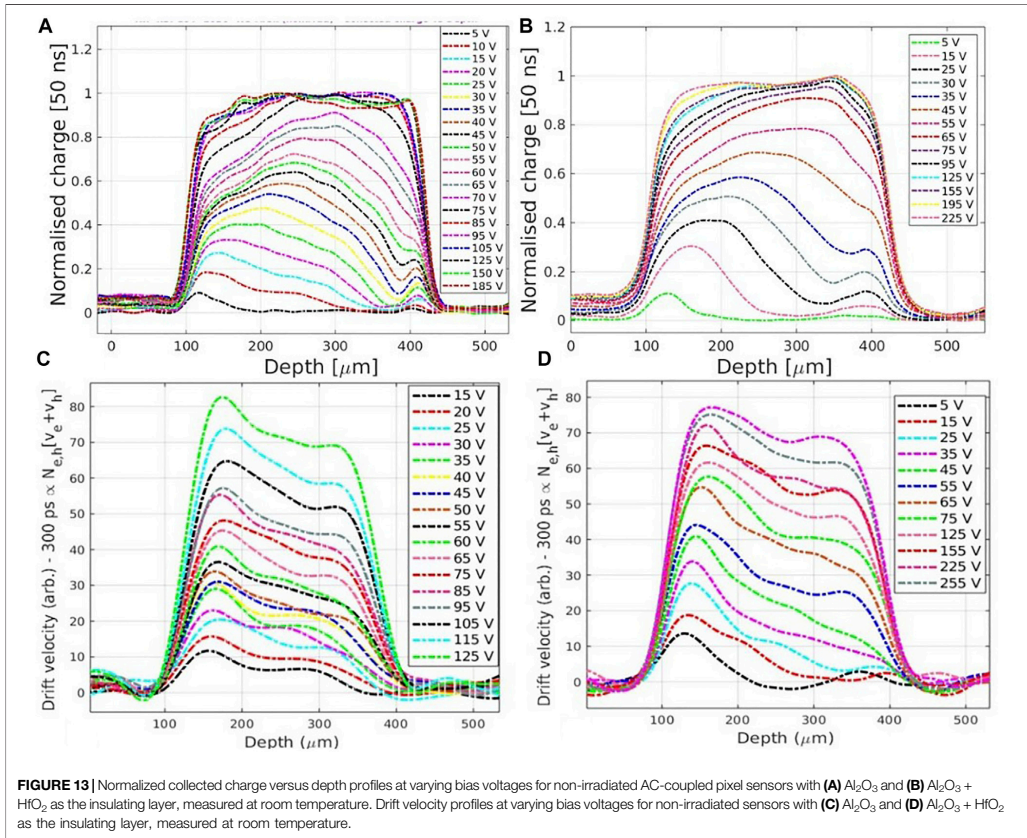
sensor at bias voltage values beyond 75 V. Therefore, the active bulk of the pixel sensors with a thickness of $\sim 320 \mu\text{m}$ is fully depleted at a bias voltage of 75 V.

For voltage values above the full depletion voltage, the total charge collected at any point across the thickness of the sensor does not depend on the position of the electron-hole pair generation. At voltage values below the full depletion voltage, the regions around the pixels are more efficient owing to the depletion growth from the segmented n^+ -implants side. Meanwhile, at bias greater than full depletion voltage, the pixelated side of the sensor is less efficient than the backplane due to the long drift of the holes and is consequently ballistic deficit. As the detector begins to deplete, a thin depleted region is formed due to the difference in the doping concentration between the p-bulk and p^{++} -Ohmic contact. As a result of this, a double-junction is observed in the charge collection profiles for low bias voltages. The non-vanishing normalized charge value is observed beyond the active thickness of the detector as a consequence of light reflection from the support plate (Kramberger et al., 2010; Kramberger et al., 2014).

The electric field can be numerically determined from Eq. 5 by extracting the drift velocity profiles using the prompt method, as shown in Figures 13C,D, for non-irradiated sensors with different dielectrics. An almost uniform gradient in the electric field profiles is observed with a maximum at a depth beyond $30 \mu\text{m}$ from the segmented side and a gradual minimum toward the backplane of the sensor. A low electric field is initially measured close to the segmented implants/pixels. This is due to the small velocity dependence on the electric field at a field strength of approximately $1 \text{ V}/\mu\text{m}$ and also the fact that the electric field

calculated at a specific position across the depth of the sensor is an average over the pixel width and the laser beam diameter. The profile reaches its peak at a depth beyond $\sim 30 \mu\text{m}$ as the current signal due to the electrons and holes is integrated over a time approximately equivalent to this distance on account of the bandwidth limitations of the amplifier and the oscilloscope. No significant difference in the electric field profiles is observed depending on the nature of the dielectric material employed in the pixel sensors.

The pixel sensor irradiated to a fluence of 10^{14} protons/cm² was fully depleted at a bias of 175 V. The full depletion voltage extracted in the charge collection profiles in Figure 14A is slightly lower (by approximately 20 V) than the value calculated from C-V measurements. At bias values above the full depletion voltage, the charge collection profiles remain almost constant with no further increase in the maximum collected charge value at any point across the active thickness of the sensor. A uniform charge collection profile is unattainable for a sensor irradiated to a fluence of 3×10^{14} protons/cm², although it is depleted at a bias of 350 V. This corresponds to the reason that the field strength is not strong enough for the release of the charge carriers from the traps. However, a sharp gradient in the charge collection profiles is observed in sensors irradiated at 10^{15} protons/cm² due to the increase in the trapping effects. The transition between active and non-active region can be seen in Figures 14B,C as a steep fall of the collected charge along the depth of the sensor. The active region grows with an increase in the bias voltage and is caused by an increase in the amount of weighting potential crossed by the charge



carriers. The weighting potential spreads across the entire thickness of the high resistivity bulk even though the sensor is not fully depleted. Some charge increases slightly at depths above ~240 μm due to the “double-peak effect” (Menichelli et al., 1999).

Furthermore, with irradiation, the electric field near the backplane of the sensor gets much weaker than the junction close to the pixels, as shown in **Figures 14D–F**, which indicates that the contribution of induced charge carriers drifting toward the backplane is less significant. This gives rise to the characteristic double-peak distortion in the electric field that gets more prominent for sensors irradiated to fluences above 10¹⁴ protons/cm². The reason behind this effect is due to deep-level traps of non-uniform concentration of charge carriers originating from radiation-induced defects (Eremin et al., 2004; Castaldini et al., 2002). As can be noticed in **Figure 14D**, for a pixel sensor irradiated at 10¹⁴ protons/cm², the double-junction effect gets less pronounced for higher bias voltages as the MCz-silicon

wafers possess a high concentration of oxygen of a magnitude of ~10¹⁷ cm⁻³ responsible for the suppression of deep-level traps formations by decreasing the mid-gap defect concentrations (Verbitskaya et al., 2007).

In the simulation, the bulk damage is approximated by an effective two-defect model with the parameters listed in **Table 2**. Surface damage is modeled in the simulation by placing a fixed charge at the oxide–Si interface and the interface traps that were assessed from the MOS capacitor simulation. The simulated electric field profiles for sensors irradiated at 2, 4, 10, and 20 × 10¹⁴ protons/cm², as shown in **Figure 15**, exhibit a similar double-peak effect that gets more pronounced for heavily irradiated samples above 2 × 10¹⁴ protons/cm². This concurs with results from the two-defect model as shown in Eremin et al. (2002).

The pulse amplitude and width is affected with irradiation. In case the electron-hole pairs are generated close to the pixels, majority of the induced charge is a consequence of holes drifting toward the backplane of the sensor. With irradiation,

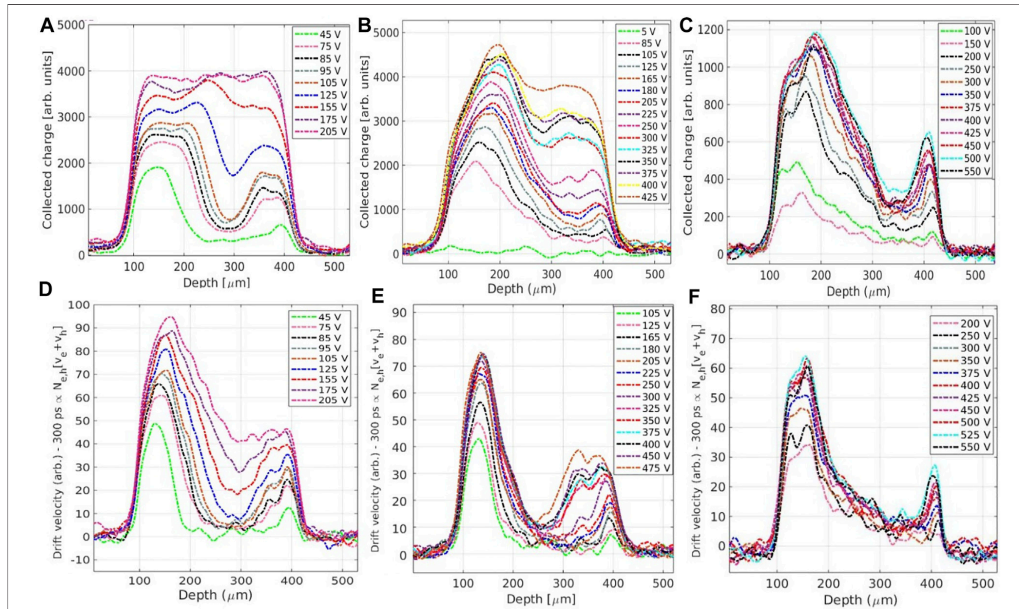


FIGURE 14 | Measured charge collection profiles at varying bias voltages for AC-coupled pixel sensor irradiated to a fluence of: **(A)** 10^{14} protons/cm², **(B)** 3×10^{14} protons/cm², and **(C)** 10^{15} protons/cm², at a temperature of -15°C . **(D-F)** Electric field profiles for the AC-coupled pixel sensors irradiated with the same fluences, respectively.

TABLE 2 | Details of the two-level bulk damage model F is the fluence in $n_{\text{acc}}/\text{cm}^2$.

Type of trap	Level (eV)	σ_e (cm ²)	σ_h (cm ²)	Concentration (cm ⁻³)
Donor	$E_v + 0.48$	$4 \cdot 10^{-14}$	$4 \cdot 10^{-14}$	0.8F
Acceptor	$E_c - 0.525$	$4 \cdot 10^{-14}$	$4 \cdot 10^{-14}$	0.8F

the signal amplitude and width get much shorter, clearly evident in the comparison between sensors irradiated to fluences of 3×10^{14} and 10^{15} protons/cm², as shown in **Figures 16B,C**, respectively. This is a consequence of high drift velocities and increases trapping effects. However, with an increase in the bias voltage, the width and the amplitude of the pulse increased due to the increase in the depletion width of the detector.

The pixel sensor irradiated to 10^{14} protons/cm² possesses shorter induced current signals due to charge carriers generated close to the pixels. However, with an increase in the depth, the peak of the signal is shifted (delayed) by a few hundreds of picoseconds corresponding to the time needed for the electrons to drift to the segmented electrodes. For heavily irradiated sensors, irradiated above 10^{14} protons/cm², the second peak in the signal gets more prominent at high bias voltages of 250 V, especially when the position of the laser beam moves away from the pixels. The reason for the second peak in the induced current pulses is mainly due to the drift of the holes generated as a

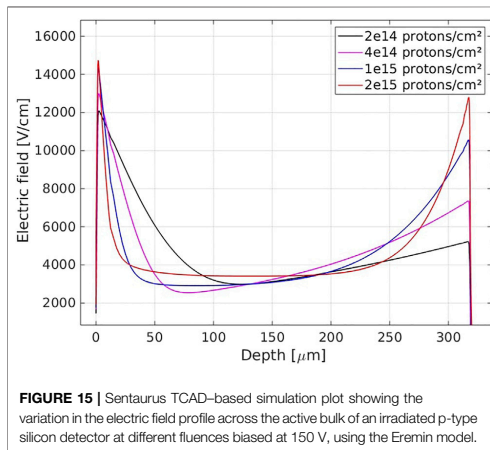
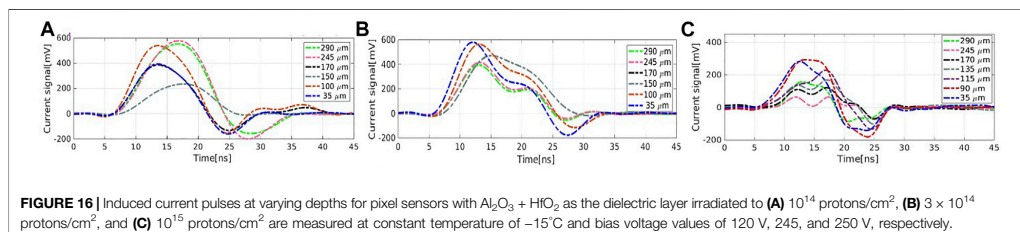


FIGURE 15 | Sentaurus TCAD-based simulation plot showing the variation in the electric field profile across the active bulk of an irradiated p-type silicon detector at different fluences biased at 150 V, using the Eremim model.

consequence of the avalanche multiplication of the electrons in the region of the high electric field near the segmented implants/pixels (Kramberger et al., 2014).



5 CONCLUSION

Characterization of MOS and MOSFET devices indicates a negative charge accumulation is induced by proton irradiation based on the study of the flat-band voltage and shift in the threshold voltage, respectively. The negative oxide charge during the irradiation is an essential prerequisite of radiation hardness resiliency of $n^+/p^-/p^+$ (n on p) particle detectors widely intended to be used in future high-luminosity experiments. MOS devices with $\text{Al}_2\text{O}_3 + \text{HfO}_2$ possess higher sensitivity to irradiation, especially when irradiated to high fluences, in comparison to samples with Al_2O_3 alone as the oxide layer. Furthermore, at fluences above 5×10^{14} protons/cm², an increase in the concentration of the interface-trapped charges leads to negative shift in threshold and a subsequent increase in the leakage current.

Studies based on e-TCT measurements suggest that the impact of different dielectric-silicon interfaces show hardly any differences on the functionality of the AC-pixel sensors. However, the double-junction effect as a consequence of deep-level traps in the bandgap of silicon was identified in proton-irradiated samples. The double-junction effect gets more prominent for sensors irradiated to higher fluences. This is congruous to the simulation studies using the two-defect model for proton-irradiated sensors.

DATA AVAILABILITY STATEMENT

The raw data supporting the conclusion of this article will be made available by the authors, without undue reservation.

REFERENCES

- Achuthan, M. K. (2007). *Fundamentals of Semiconductor Devices*. Noida, India: NPTEL.
- Arsenovich, T. (2020). *Reliability and Quality Assurance Methods for Silicon Detectors and Their Application to the Development of Detectors with Alumina Thin Films*. Helsinki, Finland: Helsinki Univ. Ph.D. thesis.
- Bharthuar, S., Ott, J., Helariutta, K., Litichevsky, V., Brücken, E., Gädda, A., et al. (2020). Study of Interpad-gap of HPK 3.1 Production LGADs with Transient Current Technique. *Nucl. Instr. Methods Phys. Res. Section A: Acc. Spectrometers, Detectors Associated Equipment* 979, 164494. doi:10.1016/j.nima.2020.164494
- Canali, C., Ottaviani, G., and Alberigi Quaranta, A. (1971). Drift Velocity of Electrons and Holes and Associated Anisotropic Effects in Silicon. *J. Phys. Chem. Sol.* 32, 1707–1720. doi:10.1016/S0022-3697(71)80137-3
- Castaldini, A., Cavallini, A., Polenta, L., Nava, F., and Canali, C. (2002). Electric Field Distribution in Irradiated Silicon Detectors. *Nucl. Instr. Methods Phys.*

AUTHOR CONTRIBUTIONS

All authors listed have made a substantial, direct, and intellectual contribution to the work and approved it for publication.

FUNDING

The research is supported by the Magnus Ehrnrooth Foundation (research grant number 200 011). This study was partially funded by the Academy of Finland (project number 314 473), “Multi-spectral photon-counting for medical imaging and beam characterization.”

ACKNOWLEDGMENTS

SB would like to acknowledge the Magnus Ehrnrooth Foundation for financial support. Facilities for detector fabrication were provided by Micronova Nanofabrication Centre in Espoo, Finland within the OtaNano research infrastructure. The proton irradiation of the samples was performed at the Accelerator Laboratory in University of Helsinki. The C-V, I-V, and TCT measurements were performed at the Detector Laboratory in Helsinki Institute of Physics. The authors are grateful for Mr. Jaakko Salonen's assistance in CMP processing.

- Res. Section A: Acc. Spectrometers, Detectors Associated Equipment* 476, 550–555. doi:10.1016/S0168-9002(01)01655-2
- de Araújo, M. A., Silva, R., de Lima, E., Pereira, D. P., and de Oliveira, P. C. (2009). Measurement of Gaussian Laser Beam Radius Using the Knife-Edge Technique: Improvement on Data Analysis. *Appl. Opt.* 48, 393. doi:10.1364/AO.48.000393
- Dieter, Y., Daas, M., Dingfelder, J., Hempterek, T., Hügging, F., Janssen, J., et al. (2021). Radiation Tolerant, Thin, Passive CMOS Sensors Read Out with the RD53A Chip. *Nucl. Instr. Methods Phys. Res. A* 1015, 165771. doi:10.1016/j.nima.2021.165771
- Eremin, V., Li, Z., Roe, S., Ruggiero, G., and Verbitskaya, E. (2004). Double Peak Electric Field Distortion in Heavily Irradiated Silicon Strip Detectors. *Nucl. Instr. Methods Phys. Res. Section A: Acc. Spectrometers, Detectors Associated Equipment* 535, 622–631. doi:10.1016/j.nima.2004.06.14310.1016/s0168-9002(04)01462-7
- Eremin, V., Strokan, N., Verbitskaya, E., and Li, Z. (1996). Development of Transient Current and Charge Techniques for the Measurement of Effective Net Concentration of Ionized Charges (Neff) in the Space Charge Region of P-N junction Detectors. *Nucl. Instr. Methods Phys. Res. Section A: Acc.*

- Spectrometers, Detectors Associated Equipment* 372, 388–398. doi:10.1016/0168-9002(95)01295-8
- Eremin, V., Verbitskaya, E., and Li, Z. (2002). The Origin of Double Peak Electric Field Distribution in Heavily Irradiated Silicon Detectors. *Nucl. Instr. Methods Phys. Res. Section A: Acc. Spectrometers, Detectors Associated Equipment* 476, 556–564. doi:10.1016/S0168-9002(01)01642-4
- Evensen, L., Hanneborg, A., Avset, B. S., and Nese, M. (1993). Guard Ring Design for High Voltage Operation of Silicon Detectors. *Nucl. Instr. Methods Phys. Res. Section A: Acc. Spectrometers, Detectors Associated Equipment* 337, 44–52. doi:10.1016/0168-9002(93)91136-B
- Fowkes, F. M., and Burgess, T. E. (1969). Electric fields at the Surface and Interface of SiO₂ Films on Silicon. *Surf. Sci.* 13, 184–195. doi:10.1016/0039-6028(69)90247-7
- Freeman, R., and Holmes-Siedle, A. (1978). A Simple Model for Predicting Radiation Effects in MOS Devices. *IEEE Trans. Nucl. Sci.* 25, 1216–1225. doi:10.1109/TNS.1978.4329516
- Fretwurst, E., Eremin, V., Feick, H., Gerhardt, J., Li, Z., and Lindström, G. (1997). Investigation of Damage-Induced Defects in Silicon by TCT. *Nucl. Instr. Methods Phys. Res. Section A: Acc. Spectrometers, Detectors Associated Equipment* 388, 356–360. doi:10.1016/S0168-9002(97)00002-8
- Gädä, A., Ott, J., Bharthuar, S., Brücken, E., Kalliokoski, M., Karadzhinova-Ferrer, A., et al. (2021). AC-coupled N-In-P Pixel Detectors on MCz Silicon with Atomic Layer Deposition (ALD) Grown Thin Film. *Nucl. Instr. Methods Phys. Res. Section A: Acc. Spectrometers, Detectors Associated Equipment* 986, 164714. doi:10.1016/j.nima.2020.164714
- Gray, J. A. (2013). The CMS Phase-1 Pixel Detector. *J. Inst.* 8, C12047. doi:10.1088/1748-0221/8/12/C12047
- Hara, K., Allport, P. P., Baca, M., Broughton, J., Chisholm, A., Nikolopoulos, K., et al. (2016). Charge Collection and Field Profile Studies of Heavily Irradiated Strip Sensors for the ATLAS Inner Tracker Upgrade. *Nucl. Instr. Methods Phys. Res. A* 331, 181–188. doi:10.1016/j.nima.2016.04.035
- Härkönen, J., Ott, J., Gädä, A., Bezak, M., Brücken, E., Tuovinen, E., et al. (2021). Processing and Interconnections of Finely Segmented Semiconductor Pixel Detectors for Applications in Particle Physics and Photon Detection. *Front. Phys.* 9, 32. doi:10.3389/fphy.2021.601730
- Härkönen, J., Ott, J., Mäkelä, M., Arsenovich, T., Gädä, A., Peltola, T., et al. (2016b). Atomic Layer Deposition (ALD) Grown Thin Films for Ultra-fine Pitch Pixel Detectors. *Nucl. Instr. Methods Phys. Res. Section A: Acc. Spectrometers, Detectors Associated Equipment* 831, 2–6. doi:10.1016/j.nima.2016.03.037
- Härkönen, J., Tuovinen, E., Luukka, P., Gädä, A., Mäenpää, T., Tuovinen, E., et al. (2016a). Processing of N⁺/p⁻/p⁺ Strip Detectors with Atomic Layer Deposition (ALD) Grown Al₂O₃ Field Insulator on Magnetic Czochralski Silicon (MCz-Si) Substrates. *Nucl. Instr. Methods Phys. Res. Section A: Acc. Spectrometers, Detectors Associated Equipment* 828, 46–51. doi:10.1016/j.nima.2016.04.069
- Hu, C. (2010). *Modern Semiconductor Devices for Integrated Circuits*. New Jersey: Pearson/Prentice Hall.
- Kaya, S., Jaksic, A., Duane, R., Vasovic, N., and Yilmaz, E. (2018). FET-based Radiation Sensors with Er 2 O 3 Gate Dielectric. *Nucl. Instr. Methods Phys. Res. Section B: Beam Interactions Mater. Atoms* 430, 36–41. doi:10.1016/j.nimb.2018.06.007
- Kaya, S., Yilmaz, E., Kahraman, A., and Karacali, H. (2015). Frequency Dependent Gamma-ray Irradiation Response of Sm₂O₃ MOS Capacitors. *Nucl. Instr. Methods Phys. Res. Section B: Beam Interactions Mater. Atoms* 358, 188–193. doi:10.1016/j.nimb.2015.06.037
- Khosrofiyan, J. M., and Garetz, B. A. (1983). Measurement of a Gaussian Laser Beam Diameter through the Direct Inversion of Knife-Edge Data. *Appl. Opt.* 22, 3406–3410. doi:10.1364/AO.22.003406
- Kramberger, G., Cindro, V., Mandić, I., Mikuž, M., Milovanović, M., and Zavrtanik, M. (2014). Modeling of Electric Field in Silicon Micro-strip Detectors Irradiated with Neutrons and Pions. *J. Inst.* 9, P10016. doi:10.1088/1748-0221/9/10/p10016
- Kramberger, G., Cindro, V., Mandić, I., Mikuž, M., Milovanović, M., Zavrtanik, M., et al. (2010). Investigation of Irradiated Silicon Detectors by Edge-TCT. *IEEE Trans. Nucl. Sci.* 57, 2294–2302. doi:10.1109/TNS.2010.2051957
- Leskelä, M. (2002). Atomic Layer Deposition (ALD): from Precursors to Thin Film Structures. *Thin Solid Films* 409, 138–146. doi:10.1016/S0040-6090(02)00117-7
- Lho, Y. H., and Kim, K. Y. (2005). Radiation Effects on the Power Mosfet for Space Applications. *Etri J.* 27, 449–452. doi:10.4218/etrij.05.0205.0031
- Lindström, G. (2003). Radiation Damage in Silicon Detectors. *Nucl. Instr. Methods Phys. Res. A* 512, 30–43. doi:10.1016/S0168-9002(03)01874-6
- Mandić, I., Cindro, V., Gorišek, A., Kramberger, G., Mikuž, M., Milovanović, M., et al. (2013). TCT Measurements of Irradiated Strip Detectors with a Focused Laser Beam. *J. Inst.* 8, P04016. doi:10.1088/1748-0221/8/04/P04016
- Mandić, I., Cindro, V., Gorišek, A., Kramberger, G., Mikuž, M., and Zavrtanik, M. (2015). Edge-TCT Measurements with the Laser Beam Directed Parallel to the Strips. *J. Inst.* 10, P08004. doi:10.1088/1748-0221/10/08/P08004
- Mandić, I., Cindro, V., Gorišek, A., Kramberger, G., Mikuž, M., Zavrtanik, M., et al. (2014). TCT Measurements with Slim Edge Strip Detectors. *Nucl. Instr. Methods Phys. Res. Section A: Acc. Spectrometers, Detectors Associated Equipment* 751, 41–47. doi:10.1016/j.nima.2014.03.026
- Menichelli, D., Bruzzi, M., Li, Z., and Eremin, V. (1999). Modelling of Observed Double-junction Effect. *Nucl. Instr. Methods Phys. Res. Section A: Acc. Spectrometers, Detectors Associated Equipment* 426, 135–139. doi:10.1016/S0168-9002(98)01482-X
- Moll, M. (1999). *Radiation Damage in Silicon Particle Detectors: Microscopic Defects and Macroscopic Properties*. Hamburg, Germany: Hamburg Univ. Ph.D. thesis.
- Müller, J., Polakowski, P., Müller, S., and Mikolajick, T. (2014). (Invited) Ferroelectric Hafnium Oxide Based Materials and Devices: Assessment of Current Status and Future Prospects. *ECS Trans.* 64, 159. doi:10.1149/06408.0159ecst
- Nicollian, E. H., and Brews, J. R. (1982). *MOS/metal Oxide Semiconductor/Physics and Technology*. John Wiley & Sons, Inc.
- Oblakowska-Mucha, A. (2017). Radiation Damage in Silicon Particle Detectors in High Luminosity Experiments. *Acta Phys. Pol. B* 48, 1707. doi:10.5506/APhysPolB.48.1707
- Orfanelli, S. (2020). The Phase 2 Upgrade of the CMS Inner Tracker. *Nucl. Instr. Methods Phys. Res. Section A: Acc. Spectrometers, Detectors Associated Equipment* 980, 164396. doi:10.1016/j.nima.2020.164396
- Ott, J., Bharthuar, S., Gädä, A., Arsenovich, T., Bezak, M., Brücken, E., et al. (2021). Characterization of Magnetic Czochralski Silicon Devices with Aluminium Oxide Field Insulator: Effect of Oxygen Precursor on Electrical Properties and Radiation Hardness. *J. Inst.* 16, P05011. doi:10.1088/1748-0221/16/05/P05011
- Ott, J., Gädä, A., Bharthuar, S., Brücken, E., Golovleva, M., Härkönen, J., et al. (2020). Processing of AC-Coupled N-In-P Pixel Detectors on MCz Silicon Using Atomic Layer Deposited Aluminium Oxide. *Nucl. Instr. Methods Phys. Res. Section A: Acc. Spectrometers, Detectors Associated Equipment* 958, 162547. doi:10.1016/j.nima.2019.162547
- Pellegrini, G., Fleta, C., Campabadal, F., Miñano, M., Lozano, M., Rafi, J. M., et al. (2007). Technology of P-type Microstrip Detectors with Radiation Hard p-spray, P-Stop and Moderated P-spray Insulations. *Nucl. Instr. Methods Phys. Res. Section A: Acc. Spectrometers, Detectors Associated Equipment* 579, 599–603. doi:10.1016/j.nima.2007.05.253
- Ramo, S. (1939). Currents Induced by Electron Motion. *Proc. IRE* 27, 584–585. doi:10.1109/jrproc.1939.228757
- Repac, J. L. (1977). Radiation-Induced Increase of Mobile Sodium in MOS Capacitors. *IEEE Trans. Nucl. Sci.* 24, 2088–2092. doi:10.1109/TNS.1977.4329170
- Sato, K., Hara, K., Onaru, K., Harada, D., Wada, S., Ikegami, Y., et al. (2020). Characteristics of Silicon Strip Sensor Irradiated up to a Proton Fluence of 10¹⁷ neq/cm². *Nucl. Instr. Methods Phys. Res. Section A: Acc. Spectrometers, Detectors Associated Equipment* 982, 164507. doi:10.1016/j.nima.2020.164507
- Schroder, D. K. (2005). *Semiconductor Material and Device Characterization*. 3rd Edition. John Wiley & Sons, Inc.
- Schwank, J. R., Shaneyfelt, M. R., Fleetwood, D. M., Felix, J. A., Dodd, P. E., Paillet, P., et al. (2008). Radiation Effects in Mos Oxides. *IEEE Trans. Nucl. Sci.* 55, 1833–1853. doi:10.1109/TNS.2008.2001040
- Shockley, W. (1938). Currents to Conductors Induced by a Moving Point Charge. *J. Appl. Phys.* 9, 635–636. doi:10.1063/1.1710367
- Suntola, T. (1992). Atomic Layer Epitaxy. *Thin Solid Films* 216, 84–89. doi:10.1016/0040-6090(92)90874-B
- Tsui, B.-Y., Su, T.-T., Shew, B.-Y., and Huang, Y.-T. (2013). Effect of Surface Preparation on the Radiation Hardness of High-Dielectric Constant Gate Dielectric. *Solid-State Elect.* 81, 119–123. doi:10.1016/j.sse.2012.11.010
- Tuovinen, E., Härkönen, J., Luukka, P., and Tuovinen, E. (2007). Intentional thermal Donor Activation in Magnetic Czochralski Silicon. *Mater. Sci. Semiconductor Process.* 10, 179–184. doi:10.1016/j.mssp.2007.11.006

- Vaitkus, J. V., Mekys, A., and Vaitekoniš, Š. (2021). Electron Mobility Dependence on Neutron Irradiation Fluence in Heavily Irradiated Silicon. *physics* 61, 1216–1225. doi:10.3952/physics.v61i2.4438
- Verbitskaya, E., Eremin, V., Li, Z., Härkönen, J., and Bruzzi, M. (2007). Concept of Double Peak Electric Field Distribution in the Development of Radiation Hard Silicon Detectors. *Nucl. Instr. Methods Phys. Res. Section A: Acc. Spectrometers, Detectors Associated Equipment* 583, 77–86. doi:10.1016/j.nima.2007.08.228
- Wiehe, M., Wonsak, S., Kuehn, S., Parzefall, U., and Casse, G. (2018). Measurements of the Reverse Current of Highly Irradiated Silicon Sensors to Determine the Effective Energy and Current Related Damage Rate. *Nucl. Instr. Methods Phys. Res. Section A: Acc. Spectrometers, Detectors Associated Equipment* 877, 51–55. doi:10.1016/j.nima.2017.09.021
- Yilmaz, E., Doğan, İ., and Turan, R. (2008). Use of Al₂O₃ Layer as a Dielectric in MOS Based Radiation Sensors Fabricated on a Si Substrate. *Nucl. Instr. Methods Phys. Res. Section B: Beam Interactions Mater. Atoms* 266, 4896–4898. doi:10.1016/j.nimb.2008.07.028

Conflict of Interest: Author AG was employed by the company Okmetic Oy.

The remaining authors declare that the research was conducted in the absence of any commercial or financial relationships that could be construed as a potential conflict of interest.

Publisher's Note: All claims expressed in this article are solely those of the authors and do not necessarily represent those of their affiliated organizations, or those of the publisher, the editors, and the reviewers. Any product that may be evaluated in this article, or claim that may be made by its manufacturer, is not guaranteed or endorsed by the publisher.

Copyright © 2022 Bharthuar, Golovleva, Bezak, Brücken, Gädda, Härkönen, Karadžhinova-Ferrer, Kramarenko, Kirschenmann, Koponen, Luukka, Mizohata, Ott and Tuominen. This is an open-access article distributed under the terms of the Creative Commons Attribution License (CC BY). The use, distribution or reproduction in other forums is permitted, provided the original author(s) and the copyright owner(s) are credited and that the original publication in this journal is cited, in accordance with accepted academic practice. No use, distribution or reproduction is permitted which does not comply with these terms.

ACTA UNIVERSITATIS LAPPEENRANTAENSIS

1012. ZAHEER, MINHAJ. Evaluation of open-source FEM software performance in analysing converter-fed induction machine losses. 2022. Diss.
1013. HAAPANIEMI, JOUNI. Power-based electricity distribution tariffs providing an incentive to enhance the capacity effectiveness of electricity distribution grids. 2022. Diss.
1014. BUAH, ERIC. Artificial intelligence technology acceptance framework for energy systems analysis. 2022. Diss.
1015. GIVIROVSKIY, GEORGY. In situ hydrogen production in power-to-food applications. 2022. Diss.
1016. SOMMARSTRÖM, KAARINA. Teachers' practices of entrepreneurship education in cooperation with companies. 2022. Diss.
1017. KAN, YELENA. Coherent anti-stokes raman scattering spectromicroscopy in biomedical and climate research. 2022. Diss.
1018. MÄNDMAA, SIRLI. Financial literacy in perspective – evidence from Estonian and Finnish students. 2022. Diss.
1019. QORRI, ARDIAN. Measuring and managing sustainable development in supply chains. 2022. Diss.
1020. MARTIKAINEN, SUVI-JONNA. Meaningful work and eudaimonia: contributing to social sustainability in the workplace. 2022. Diss.
1021. MANNINEN, KAISA. Conducting sustainability target-driven business. 2022. Diss.
1022. LI, CHANGYAN. Design, development, and multi-objective optimization of robotic systems in a fusion reactor. 2022. Diss.
1023. CHOUDHURY, TUHIN. Simulation-based methods for fault estimation and parameter identification of rotating machines. 2022. Diss.
1024. DUKEOV, IGOR. On antecedents of organizational innovation: How the organizational learning, age and size of a firm impact its organizational innovation. 2022. Diss.
1025. BREIER, MATTHIAS. Business model innovation as crisis response strategy. 2022. Diss.
1026. FADEEV, EGOR. Magnetotransport properties of nanocomposites close to the percolation threshold. 2022. Diss.
1027. KEPSU, DARIA. Technology analysis of magnetically supported rotors applied to a centrifugal compressor of a high-temperature heat pump. 2022. Diss.
1028. CHAUHAN, VARDAN. Optimizing design and process parameters for recycled thermoplastic natural fiber composites in automotive applications. 2022. Diss.
1029. RAM, MANISH. Socioeconomic impacts of cost optimised and climate compliant energy transitions across the world. 2022. Diss.
1030. AMADI, MIRACLE. Hybrid modelling methods for epidemiological studies. 2022. Diss.
1031. RAMÍREZ ANGEL, YENDERY. Water-energy nexus for waste minimisation in the mining industry. 2022. Diss.

- 1032.** ZOLOTAREV, FEDOR. Computer vision for virtual sawing and timber tracing. 2022. Diss.
- 1033.** NEPOVINNYKH, EKATERINA. Automatic image-based re-identification of ringed seals. 2022. Diss.
- 1034.** ARAYA GÓMEZ, Natalia Andrea. Sustainable management of water and tailings in the mining industry. 2022. Diss.
- 1035.** YAHYA, MANAL. Augmented reality based on human needs. 2022. Diss.
- 1036.** KARUPPANNAN GOPALRAJ, SANKAR. Impacts of recycling carbon fibre and glass fibre as sustainable raw materials for thermosetting composites. 2022. Diss.
- 1037.** UDOKWU, CHIBUZOR JOSEPH. A modelling approach for building blockchain applications that enables trustable inter-organizational collaborations. 2022. Diss.
- 1038.** INGMAN, JONNY. Evaluation of failure mechanisms in electronics using X-ray imaging. 2022. Diss.
- 1039.** LIPIÄINEN, SATU. The role of the forest industry in mitigating global change: towards energy efficient and low-carbon operation. 2022. Diss.
- 1040.** AFKHAMI, SHAHRIAR. Laser powder-bed fusion of steels: case studies on microstructures, mechanical properties, and notch-load interactions. 2022. Diss.
- 1041.** SHEVELEVA, NADEZHDA. NMR studies of functionalized peptide dendrimers. 2022. Diss.
- 1042.** SOUSA DE SENA, ARTHUR. Intelligent reflecting surfaces and advanced multiple access techniques for multi-antenna wireless communication systems. 2022. Diss.
- 1043.** MOLINARI, ANDREA. Integration between eLearning platforms and information systems : a new generation of tools for virtual communities. 2022. Diss.
- 1044.** AGHAJANIAN MIANKOUH, SOHEIL. Reactive crystallisation studies of CaCO₃ processing via a CO₂ capture process : real-time crystallisation monitoring, fault detection, and hydrodynamic modelling. 2022. Diss.
- 1045.** RYYNÄNEN, MARKO. A forecasting model of packaging costs : case plain packaging. 2022. Diss.
- 1046.** MAILAGAHA KUMBURE, MAHINDA. Novel fuzzy k-nearest neighbor methods for effective classification and regression. 2022. Diss.
- 1047.** RUMKY, JANNATUL. Valorization of sludge materials after chemical and electrochemical treatment. 2022. Diss.
- 1048.** KARJUNEN, HANNU. Analysis and design of carbon dioxide utilization systems and infrastructures. 2022. Diss.
- 1049.** VEHEMAANPERÄ, PAULA. Dissolution of magnetite and hematite in acid mixtures. 2022. Diss.



ISBN 978-952-335-876-8
ISBN 978-952-335-877-5 (PDF)
ISSN 1456-4491 (Print)
ISSN 2814-5518 (Online)
Lappeenranta 2022